

NON VOLCANIC TREMORS AND SEISMIC NOISE TOMOGRAPHY AT THE CHILE  
TRIPLE JUNCTION

By

ALEJANDRO GALLEGO

A DISSERTATION PRESENTED TO THE GRADUATE SCHOOL  
OF THE UNIVERSITY OF FLORIDA IN PARTIAL FULFILLMENT  
OF THE REQUIREMENTS FOR THE DEGREE OF  
DOCTOR OF PHILOSOPHY

UNIVERSITY OF FLORIDA

2010

© 2010 Alejandro Gallego

## ACKNOWLEDGMENTS

I would like to say thanks to my advisor Raymond Russo for the opportunity to participate in this project and for his help during my Phd program. To him, along with Diana Comte, Eduardo Moscoso, Victor Mocanu, Ruth Murdie and John VanDecar, thank you for the great team work and adventures in Patagonia. To my committee members: Liz Screaton, Michael Perfit, Mark Panning, David Foster, and Jacob Jones, for comments and suggestions. Two anonymous reviewers and Mark Panning for important improvements and suggestions in seismic inversion techniques. To the office staff of the geology department: Pam, Nita, Crystal and Susan for reminding me of my administrative duties. Thanks to my parents, who helped me during my college career and for their constant support, and thanks to my wife April for her love and patience.

And finally, to all people from Chile that made the Chile Triple Junction Project possible: Umberto Fuenzalida, Hernan Marilao, Carmen Gloria of the Universidad de Chile; Corporacion Nacional Forestal de Chile (CONAF)—Juan Fica, Claudio Manzur, Carlos Llatureo; Sra. Monica Retamal Maturana, Banco Estado; Carabineros de Chile del Region de Aysen; Armada de Chile; Cuerpo Militar de Trabajo del Ejercito de Chile (Cmdte. Roldan, Maj. Wellkner); Alcaldes de Aysen, Melinka (Luis Miranda Chiguay), Rio Ibanez, Lago Verde; Ejercito de Chile; Aeronautica de Chile (Sr. Carlos Feliu Ruiz); Automotriz Varona (Don Luis Hidalgo); Don Gustavo Lopez y Hostal Bon; Mike Fort, Noel Barstow, Bruce Beaudoin, Jim Fowler of IRIS PASSCAL; Tripulacion de LM Petrel IV (CONAF)—Juan Gallardo, Axel Hernandez, Hernan Aguilar, Jose Geicha Nauto; Gilles Rigaud, Aurelia Rigaud, Valerie Clouard, Lorena Palacio et Morgane; Eduardo Moscoso, Javier; Don Raul Hernandez, Fundo Los Nirres; Ing. Sergio Mirando Contreras (Melinka); Escuela Carlos Condell, Calete Andrade,

Pto. Aguirre (Sr. Victor Figueroa); Enrique Alcalde (Cochrane); Luis Levin (Bahia Murta);  
Baterias GAMI (Puerto Montt); Mauricio Zambrano L. (Coyhaique Centro de Llamadas);  
Rolando Burgos and Roselia Delgado, Fachinal; Aladin Jara, Gob. De Chile Chico; Rolando  
Toloza, Min. Obras Publicas; Mark and Sra. Knipreth, Heart of the Andes Lodge; Tripulacion de  
El Aleph—Heraldo Zapata Rivera, Ramon Villegas, Omar Tapia Vidal, Jorge Oyarzun  
Inostroza; Sandalio Munoz, Fundo La Pedregosa; Don Cristian Brautigam; and the many, many  
people of Region XI, Aysen.

To my parents

# TABLE OF CONTENTS

|  | <u>page</u> |
|--|-------------|
| ACKNOWLEDGEMENTS.....  | 3           |
| LIST OF TABLES.....  | 8           |
| LIST OF FIGURES .....  | 9           |
| LIST OF ABREVIATOINS.....  | 12          |
| ABSTRACT.....  | 13          |
| CHAPTER  |             |
| 1      TECTONIC SETTING .....  | 15          |
| 1.1 Subduction of the Chile Ridge .....  | 15          |
| 1.2 Geologic Setting.....  | 16          |
| 1.3 Data Acquisition and Instrumentation.....  | 18          |
| 2      NON VOLCANIC TREMORS AT THE CHILE TRIPLE JUNCTION .....                         | 27          |
| 2.1 Introduction.....  | 27          |
| 2.2 Methodology .....  | 30          |
| 2.2.1 Time Distribution of NVT. ....   | 30          |
| 2.2.2 Hypocentral Determination of Non Volcanic Tremor.....                            | 31          |
| 2.2.3 Other Analysis .....   | 32          |
| 2.3 Results.....   | 33          |
| 2.3.1 Characteristics of NVT at the CTJ. ....  | 33          |
| 2.3.2 Time Histograms of Tremor Activity.....  | 33          |
| 2.3.3 Non Volcanic Tremor Location .....   | 34          |
| 2.3.4 NVT Frequency of Occurrence. ....  | 34          |
| 2.3.5 Low Frequency Earthquakes .....  | 36          |
| 2.4 Discussion.....  | 36          |
| 2.5 Conclusion .....   | 41          |
| 3      TIDAL CONSTITUENTS IN NON VOLCANIC TREMORS AT THE CHILE TRIPLE<br>JUNCTION..... | 59          |
| 3.1 Introduction.....  | 59          |
| 3.2 Methodology .....  | 61          |
| 3.3 Results.....   | 62          |
| 3.4 Discussion.....  | 63          |
| 3.5 Conclusions.....   | 65          |

|       |   |     |
|-------|---|-----|
| 4     | SEISMIC NOISE TOMOGRAPHY IN THE CHILE RIDGE SUBDUCTION REGION.  | 75  |
| 4.1   | Introduction.....   | 75  |
| 4.2   | Data.....   | 76  |
| 4.3   | Methodology.....  | 77  |
| 4.3.1 | Cross-Correlation of Noise .....  | 77  |
| 4.3.2 | Signal to Noise Ratio, SNR .....  | 79  |
| 4.3.3 | Dispersion and Rayleigh Wave Group Velocities .....   | 80  |
| 4.3.4 | 2-D Travel Time Inversion.....  | 81  |
| 4.3.5 | 3-D Travel Time Inversion.....  | 82  |
| 4.4   | Results.....  | 83  |
| 4.4.1 | 5-10 Second Period Inversion.....   | 83  |
| 4.4.2 | 10-20 Second Period Inversion .....   | 84  |
| 4.4.3 | 3-D Group Velocity Inversion .....  | 84  |
| 4.5   | Discussion .....  | 84  |
| 4.6   | Conclusions.....  | 86  |
| 5     | AZIMUTHAL ANISOTROPY OF THE UPPER CRUST FROM AMBIENT SEISMIC<br>NOISE AT THE CHILE TRIPLE JUNCTION..... | 105 |
| 5.1   | Introduction.....   | 105 |
| 5.2   | Methodology .....   | 107 |
| 5.2.1 | Radial Anisotropy from Group Velocity of Love and Rayleigh Waves....                                    | 107 |
| 5.2.2 | Azimuthal Anisotropy from Phase Velocity Rayleigh Waves.....  | 108 |
| 5.2.3 | 2-D Travel Time Inversion for Anisotropic Terms.....  | 111 |
| 5.3   | Results.....  | 112 |
| 5.4   | Discussion .....  | 114 |
| 5.5   | Conclusions.....  | 117 |
|       | SUMMARY AND CONCLUSIONS.....  | 132 |
|       | REFERENCE LIST .....  | 134 |
|       | BIOGRAPHICAL SKETCH.....  | 144 |

## LIST OF TABLES

| <u>Table</u>  | <u>page</u> |
|---|-------------|
| 3-1 Tidal constituents of solid earth tide, product of moon and sun gravitational attraction (Wahr 1995)..... | 67          |
| 3-2 Maximum cross-correlation of NVT signal and solid Earth tidal displacement .....                          | 68          |

## LIST OF FIGURES

| <u>Figure</u>   | <u>page</u> |
|---|-------------|
| 1-1 Tectonics and topography of Chile Triple Junction (CTJ) area.....   | 20          |
| 1-2 Shaded-relief bathymetry in the area of the Chile Triple Junction (Ranero, 2006).....   | 21          |
| 1-3 Common Caption: Geologic map of CTJ region, modified from Escobar (1980).....   | 22          |
| 1-4 Continuation Figure 1-3.....  | 23          |
| 1-5 Viscoelastic numerical model from GPS observations.....   | 24          |
| 1-6 Seismic events from 1964 to present (IRIS DMC catalog).....   | 25          |
| 1-7 Details of seismic network..  | 26          |
| 2-1 Non Volcanic Tremor waveform. .   | 43          |
| 2-2 Time series analysis of NVT. ....   | 44          |
| 2-3 Brightness function calculated for a tremor burst .....   | 45          |
| 2-4 One continuous hour of tremor signal (top) and spectrogram (bottom).....  | 46          |
| 2-5 Comparison of a tremor burst and local earthquake near the epicentral area of NVT..   | 47          |
| 2-6 Particle motion diagram of NVT signal. ....   | 48          |
| 2-7 Amplification of a LFE within tremor signals.....   | 49          |
| 2-8 Epicentral location of LFE..  | 50          |
| 2-9 Delay time between P and S waves for a LFE.....   | 51          |
| 2-10 LFE earthquake analysis.....   | 52          |
| 2-11 Frequency comparison between Local Earthquakes (LE), low frequency earthquakes (LFE), non volcanic tremor (NVT), and background noise..... | 53          |
| 2-12 Epicentral location of NVT and LFE. ....   | 54          |
| 2-13 Distance from the active Chile ridge to the center of the northern and southern cluster of NVT.....  | 55          |

|      |   |     |
|------|---|-----|
| 2-14 | Vertical sections of NVT hypocenters. ....  | 56  |
| 2-15 | Number of NVT located with SSA as a function of depth. ....   | 57  |
| 2-16 | Cumulative frequency of NVT at the Chile Triple Junction. ....  | 58  |
| 3-1  | Binarized signal of tremor duration time series per hour .....  | 69  |
| 3-2  | Power spectrum of binarized tremor time series.. ....   | 70  |
| 3-3  | Power spectrum of binarized tremor time series for diurnal periods.. ....                                 | 71  |
| 3-4  | Station ISM spectrogram. ....   | 72  |
| 3-5  | Station PLM spectrogram. ....   | 73  |
| 3-6  | Tidal amplitude (red line) and tremor activity (dark bars) during a period of 700 hours... 74             |     |
| 4-1  | Time series of cross-correlation for station HOP01 .....  | 88  |
| 4-2  | Time series of cross-correlation for station HUD01.....   | 89  |
| 4-3  | Frequency analysis of cross-correlated waveform between station PLM and IBJ.....                          | 90  |
| 4-4  | Azimuthal distribution of stations path.....  | 91  |
| 4-5  | Data analysis for Right and Left side of the cross-correlation for three period bands. ....               | 92  |
| 4-6  | Selected velocities for station pairs with SNR > 6 and distance large than 1.5 .....                      | 93  |
| 4-7  | FTAN analysis for IBJ-PLM station pair .....  | 94  |
| 4-8  | 407 curves dispersion curves (back) and the averaged group velocity at each period.....                   | 95  |
| 4-9  | 1D inversion model (red line) for the averaged dispersion curves.....                                     | 96  |
| 4-10 | Group velocity derivatives of the calculated model .....  | 97  |
| 4-11 | Interstation paths for group velocities derived from Green's functions filtered at 5-10 sec period. ....  | 98  |
| 4-12 | Interstation paths for group velocities derived from Green's functions filtered at 10-20 sec period. .... | 99  |
| 4-13 | Resolution map for 5-10 sec period group velocities. ....   | 100 |

|      |  |     |
|------|--|-----|
| 4-14 | Resolution map for 10-20 sec period group velocities. ....                 | 101 |
| 4-15 | Group velocity model for 5-10 sec periods. ....                            | 102 |
| 4-16 | Group velocity model for 10-20 sec periods. ....                           | 103 |
| 4-17 | 3D inversion calculated using dispersion analysis .....                    | 104 |
| 5-1  | Dispersion curves for Rayleigh (R) and Love (L) wave group velocities..... | 118 |
| 5-2  | Radial anisotropy model in the upper crust at the CTJ.....                 | 119 |
| 5-3  | Checkerboard test of the study area.....                                   | 120 |
| 5-4  | Inversion results for 5 sec period.....                                    | 121 |
| 5-5  | Inversion results for 6 sec period.....                                    | 122 |
| 5-6  | Inversion results for 7 sec period.....                                    | 123 |
| 5-7  | Inversion results for 8 sec period.....                                    | 124 |
| 5-8  | Inversion results for 9 sec period.....                                    | 125 |
| 5-9  | Inversion results for 10 sec period.....                                   | 126 |
| 5-10 | Inversion results for 11 sec period.....                                   | 127 |
| 5-11 | Inversion results for 12 sec period.....                                   | 128 |
| 5-12 | Inversion results for 13 sec period.....                                   | 129 |
| 5-13 | Inversion results for 14 sec period.....                                   | 130 |
| 5-14 | Inversion results for 15 sec period.....                                   | 131 |

## LIST OF ABBREVIATIONS

|      |   |
|------|---|
| CRSP | Chile Ridge Seismic Project                       |
| CTJ  | Chile Triple Junction                             |
| DAS  | Data Acquisition System                           |
| DMC  | Data Management center                            |
| EMC  | Eastern Metamorphic Complex                       |
| ETS  | Episodic Tremor and Slip                          |
| FTAN | Frequency Time Dispersion Analysis                |
| GPS  | Global Positioning System                         |
| IRIS | Incorporated Research Institutions for Seismology |
| LCPB | Lower Cretaceous Patagonian Batholith             |
| LFE  | Low Frequency Earthquakes                         |
| LGC  | Lago General Carrera                              |
| LOFZ | Liquiñe Ofqui Fault Zone                          |
| MPB  | Miocene Patagonian Btholith                       |
| NPB  | North Patagonian Batholith                        |
| NVT  | Non Volcanic Tremors                              |
| SSE  | Slow Slip Events                                  |
| SVZ  | Southern Volcanic Zone                            |
| WMC  | Western Metamorphic Complex                       |

Abstract of Thesis Presented to the Graduate School  
of the University of Florida in Partial Fulfillment of the  
Requirements for the Degree of Doctor of Philosophy

NON VOLCANIC TREMORS AND SEISMIC NOISE TOMOGRAPHY AT THE CHILE  
TRIPLE JUNCTION

By

Alejandro Gallego

December 2010

Chair: R. M. Russo

Major: Geology

The subduction of the Chile Ridge, the active mid-ocean spreading ridge between the Nazca and Antarctic plates, beneath Patagonian South America provides a unique opportunity to study spreading ridge subduction. From Dec 2004 to Feb 2007 the Chile Ridge Subduction Project (CRSP) temporary seismic network, operated jointly by the University of Florida and the Universidad de Chile, recorded seismic data at 59 seismic stations deployed in the Chile Triple Junction (CTJ) region including local, regional, and teleseismic earthquakes data order to study the ridge subduction. This study includes two main sections, one detailing results of the first observations of nonvolcanic seismic tremors (NVT) to be made in South America, and the second presenting the results of the first study of crustal structure and seismic anisotropy in the CTJ region deriving from ambient seismic noise. The tremor signals at the CTJ appear as low frequency (5-10 Hz) ringing seismic signals, rising clearly above noise; they have durations of up to 48 hours per episode. Tremors are located around 100 km east of the trench in a narrow band that follows the strike of the Nazca slab, but with activity concentrated in two clusters in the north and south of the Chonos Archipelago. Clear correlation was observed between the occurrence of NVT and the amplitudes of solid Earth tides. Semi-diurnal, diurnal and long-

period modulations of tremor signals at the principal solid Earth tidal frequencies were clearly observed. Time series of tidal displacement in the CTJ area were calculated and cross-correlated with the NVT signals. The maximum cross-correlations between the two time series are obtained when tidal displacements parallel the orientations of major structures of the subducted Nazca plate and the Nazca-South America plate boundary. In the second part of this study (chapters 4 and 5), cross-correlation of recorded ambient seismic noise was used to estimate inter-station surface wave time-domain Green's functions, and the resulting travel times were inverted to obtain crustal surface wave velocities and anisotropy models. The resulting inversion shows that cell velocities correlate well with known geologic features: crustal velocities are high where the Patagonian Batholith outcrops or is likely present at depth; and low velocities correlate with sedimentary and volcanoclastic basins, and with the active volcanic arc of the Southern Volcanic Zone and the subducted Chile ridge in Taitao peninsula, where recent volcanism and thermal activity of hot springs is present. High velocities in the mountainous portions of the southeastern study area appear to correlate with outcropping older metamorphic units. For the anisotropic model, high radial anisotropy coincides with a highly layered Chonos metamorphic complex and fast raypaths of crustal azimuthal anisotropy trend approximately N-S, parallel to the pervasive metamorphic fabric orientations (e.g. foliation) of the crustal units in the study region and with the strike of the Liquine-Ofqui strike-slip fault.

## CHAPTER 1 TECTONIC SETTING

### 1.1 Subduction of the Chile Ridge

The current tectonics of the study area (Figure 1-1 and Figure 1-2) are controlled by the subduction of the actively spreading Chile Ridge and transform faults (Cande and Leslie 1986, Cande et al. 1987, Eagles 2004, Breitsprecher and Thorkelson 2009), the plate boundary between the Antarctic and Nazca oceanic plates, currently subducting beneath South America at convergence rates of 1.85 and 6.6 cm/yr, respectively (Wang et al., 2008). The three tectonic plates meet at the Chile Triple Junction (CTJ). The CTJ has progressively migrated from south to north, beginning with subduction of the first ridge segment 14 Ma ago at Tierra del Fuego latitudes (55°S), and is now located at 46.5°S (Cande and Leslie 1986). Subduction of active ridge segments leads to formation of a slab window – a gap between the subducted oceanic lithospheres (Russo et al. 2010, Russo et al. 2010b) – due to continued spreading and cessation of new lithosphere production (Cande and Leslie 1986, Ramos and Kay 1992, Murdie et al. 1993, Breitsprecher and Thorkelson 2009). The Incorporated Research Institutions for Seismology (IRIS). Data Management Center (DMC) catalog shows offshore seismicity ( $M > 4$ ) occurring on the active ridge segments and transform faults of the Chile Ridge. Onshore, seismic activity is low and the only previous seismic study realized in this area revealed a sparse alignment of slab earthquakes parallel to the subducted Taitao fracture zone, indicating continued slip on this ridge transform after subduction (Murdie et al. 1993). South of the CTJ, the seismicity is poorly recorded and apparently even less active, perhaps owing to the slow convergence of the Antarctic plate. Between the Chonos Archipelago and the continent, the Liquiñe-Ofqui fault zone (LOFZ) is an active, low-seismicity, dextral strike-slip fault, with a length of ~1000 km extending from 40-47°S, striking parallel to the volcanic arc trend

(Cembrano and Herve 1993, Rosenau et al. 2006). Current surface site velocities of this area revealed by Global Positioning System (GPS) observations include approximately arc-normal motion of the coast and evidence for dextral displacement on the LOFZ, allowing the northward translation of the Chonos forearc sliver (Wang et al. 2008). North of the study region, average rates of motion are estimated to be 3.6 cm/yr since Pliocene times, decreasing northward to 1.3 cm/yr (Rosenau et al. 2006).

## **1.2 Geologic Setting**

The geology of the South American plate in the CTJ area (Figure 1-3) is divisible into four principal geologic units that lie in approximately north-south belts along the subduction zone. The Western Metamorphic Complex (WMC) constitutes the primary basement outcrops in the forearc domain of the Chonos archipelago and Taitao Peninsula. In the Chonos islands, the WMC is constituted by an eastern belt, composed of metaturbidites, and a western belt, mainly formed by strongly foliated mica schists and greenschists (Herve et al. 2008). Rare preserved fossil faunas date this formation to the Late Triassic (Fang et al. 1998). Intercalated mica schists, phyllites, and other metasediments make up the remaining WMC units (Escobar 1980). The Taitao ophiolite complex, outcropping on the westernmost tip of the Taitao Peninsula, is evidence of obduction of young Nazca plate crust, a product of the collision between the Tres Montes segment of the Chile ridge and the overriding continent (Forsythe and Nelson 1985, Forsythe et al. 1986, Nelson et al. 1993, Lagabrielle et al. 1994, Shibuya et al. 2007).

The North Patagonian Batholith (NPB) is one of the world's largest intrusive bodies, extending from 41°S to 52°S, with a width of nearly 200 km. The granodiorites, granites, and tonalites of the NPB are divisible into two north-south trending bands that differ mainly in age (Pankhurst et al. 1999): the Miocene central band (MPB) outcrops continuously along the

active volcanic arc north of the CTJ (i.e.,  $\sim 46^\circ$  S), but does not extend south of the bifurcation of the Liquiñe-Ofqui fault. In contrast, the Lower Cretaceous North Patagonian Batholith (LCPB) outcrops throughout the study region, primarily to the east of the Liquiñe-Ofqui fault zone, but some satellite bodies outcrop in a N-S trending belt along the easternmost Chonos islands and the Taitao Peninsula. The LCPB extends continuously across the pronounced gap in modern arc volcanic activity (Ramos and Kay 1992) but trends NNE, and thus occupies a forearc position south of the Golfo de Penas (Figure 1-3).

The Paleozoic Eastern Metamorphic Complex (EMC) outcrops in the SE of the study region, includes the oldest rocks in the area, and is formed by two distinct successions: The Rio Lacteo Formation in the north comprises medium-grade metasediments, and the Bahia de la Lancha Formation in the south comprises tightly folded turbidites metamorphosed at low grade (Bell and Suarez 2000, Herve et al. 2008).

North of the EMC outcrops ( $\sim 47^\circ$  S), between the LCPB and the Chile-Argentina border, faulted and folded Jurassic and Tertiary felsic and intermediate volcanics and sedimentary rocks of the Patagonian Ranges outcrop both north and south of the current CTJ (Escobar 1980, Lagabrielle et al. 2004, Lagabrielle et al. 2007). A suite of Tertiary basalts erupted above the Patagonian Range units in Chile, but much more extensively in Argentina, are thought to represent a shift of magmatic activity - normally expressed at the arc - to the back-arc region, where extensive Neogene plateau lavas have erupted synchronously with ridge segment subduction (Ramos and Kay 1992, Gorrington et al. 1997, Espinoza et al. 2005, Guivel et al. 2006, Espinoza et al. 2008). Interaction of the ridge segment subducted at 6 Ma with the overriding plate is also indicated by a marked change in deformation and uplift north and south of Lago General Carrera (LGC) (Lagabrielle et al. 2004, Ramos 2005, Lagabrielle et al. 2007). Near

Lago Carrera, a low gravity anomaly is associated with the both ridge subduction and a change in the crustal thickness (Murdie et al. 2000).

Pleistocene-Holocene strato volcanoes built atop the MPB/LCPB, forming the southern part of the Southern Volcanic Zone (SVZ), are closely aligned with the trend of the LOFZ (Cembrano et al. 1996). Within the study region, five major strato volcanic centers (Figure 1-1) have been active during Holocene-Recent: Melimoyu ( $200 \pm 75$  AD), Mentolat ( $1710 \pm 5$  AD), Maca ( $410 \pm 10$  AD), Cay (Holocene), and Hudson (1991). Hudson is the southernmost volcano of the SVZ, lying essentially due east of the CTJ. Between the SVZ and the Austral Volcanic zone (AVZ) south of the study area, a gap in volcanism of about 500 km is thought to be a result of perturbations in to the upper mantle wedge beneath South America caused by subduction of the Chile Ridge and slab window formation (Cande and Leslie 1986, Ramos and Kay 1992). The presence of recent volcanism and hot springs in the Taitao Peninsula at more than 100 km west of the volcanic arc, is evidence of the interaction between the subducted active and hot Chile Ridge and the overriding plate (Lagrabielle et al. 2000).

### **1.3 Data Acquisition and Instrumentation**

The Chile Ridge Subduction Project seismic network (Figure 1-7) consisted of 59 seismic stations, including 32 STS-2 broadband sensors, 4 L22 short period and 4 fat stations composed of 1 Guralp broadband sensor and 3 or 4 L22 short period sensors in a T- or an L-shaped geometric arrangement. Data were recorded continuously at a sample rate of 50 Hz. Most of the sites lacked alternating current electrical power and batteries charged by solar panels were necessary.

The installation of the equipment required the installation of interconnected subsystems:

- Sensor
- Power sub-system (batteries, solar power, battery charger, utility company, etc)
- GPS timing system

- Data acquisition system (DAS)
- Intra-system cables

To protect the sensor against animals and seasonal and diurnal thermal variations, the sensors were placed in a specially-constructed vault below ground and, if necessary, a fence was constructed around the station. The sensors were placed in a hole about 1.5 m deep and 0.5 m diameter floored by a flat poured-concrete slab. At the bottom of the barrels used for vaults, a drainage tube was installed to evacuate excess rain water and ground water percolation. The sensors were leveled and oriented properly to provide ground motion in the vertical, north-south, and east-west directions. The power subsystems included two 100 Amp-hour deep-cycle marine batteries, two 65 Watt photovoltaic solar panels and a power box that provided a trickle-charge (i.e., one way from panels to batteries) of the batteries and which distributed the energy to the sensor and DAS. The solar panels were attached to a wooden frame facing to the north and inclined at 60° from vertical to capture the maximum solar power at the study region latitude. Batteries at stations powered by wall current were connected to a battery charger. The DAS and batteries were placed together in a plastic container protected from weather conditions at all outdoor sites. The GPS antennas were located at the top of the solar panel frames or on appropriate building architecture. The network was visited approximately every 6 months to collect the data and to provide routine maintenance. Because of the challenging geographic and climatic conditions the use of ships and, in one instance, a hydroplane, was necessary to reach stations located in the Chonos Archipelago and on the Taitao Peninsula, and 4x4 pickups and horses were used to reach the remaining sites. In populated areas, stations were often sited on private property, and the help provided by the local landowners was a very important factor in the success of the project.

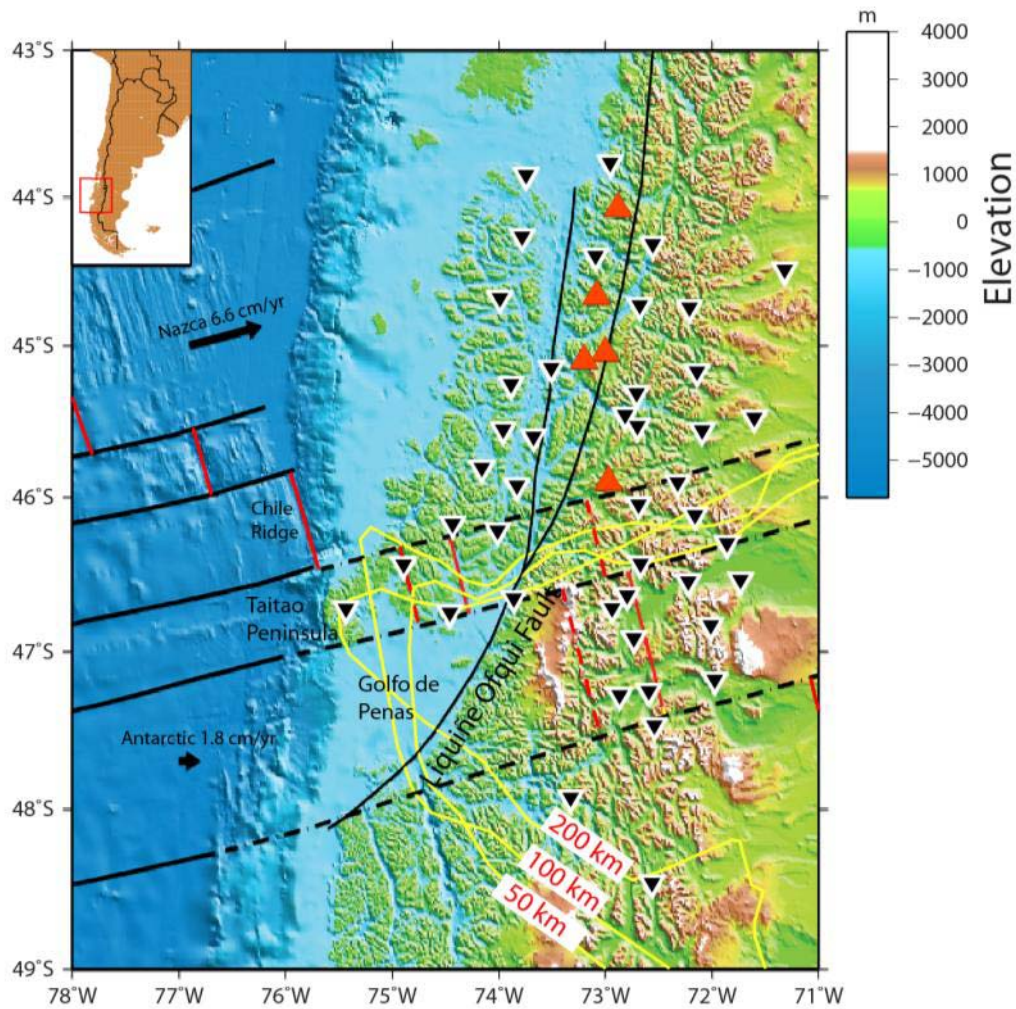


Figure 1-1. Tectonics and topography of Chile Triple Junction (CTJ) area. Black inverted triangles, seismic stations; red triangles, volcanoes. Black and red lines: transform faults, fracture zones, and active ridge segments, dashed where subducted (surface projections by (Murdie and Russo 1999)). Arrows are relative convergence directions of Nazca (6.6 cm/yr) and Antarctic (1.8 cm/yr) plates (Wang et al., 2007). Double stranded fault cutting the region is the Liquiñe-Ofqui fault zone. Yellow curved lines, Patagonian slab window boundary defined by P wave tomography, shown at three depths: 50, 100 and 200 km (Russo et al. 2010, Russo et al. 2010b).

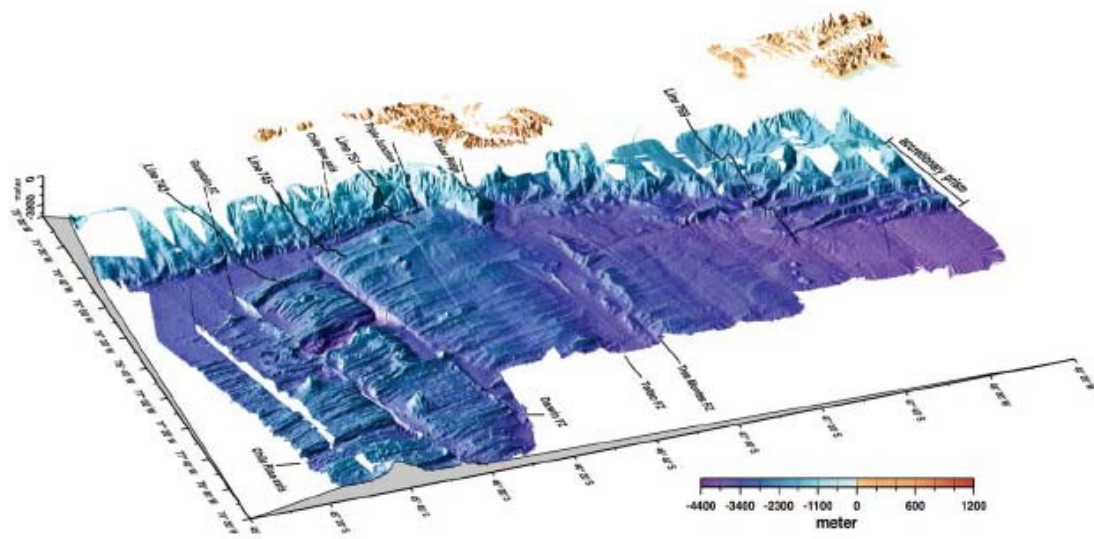


Figure 1-2 Shaded-relief bathymetry in the area of the Chile Triple Junction (Ranero, 2006).

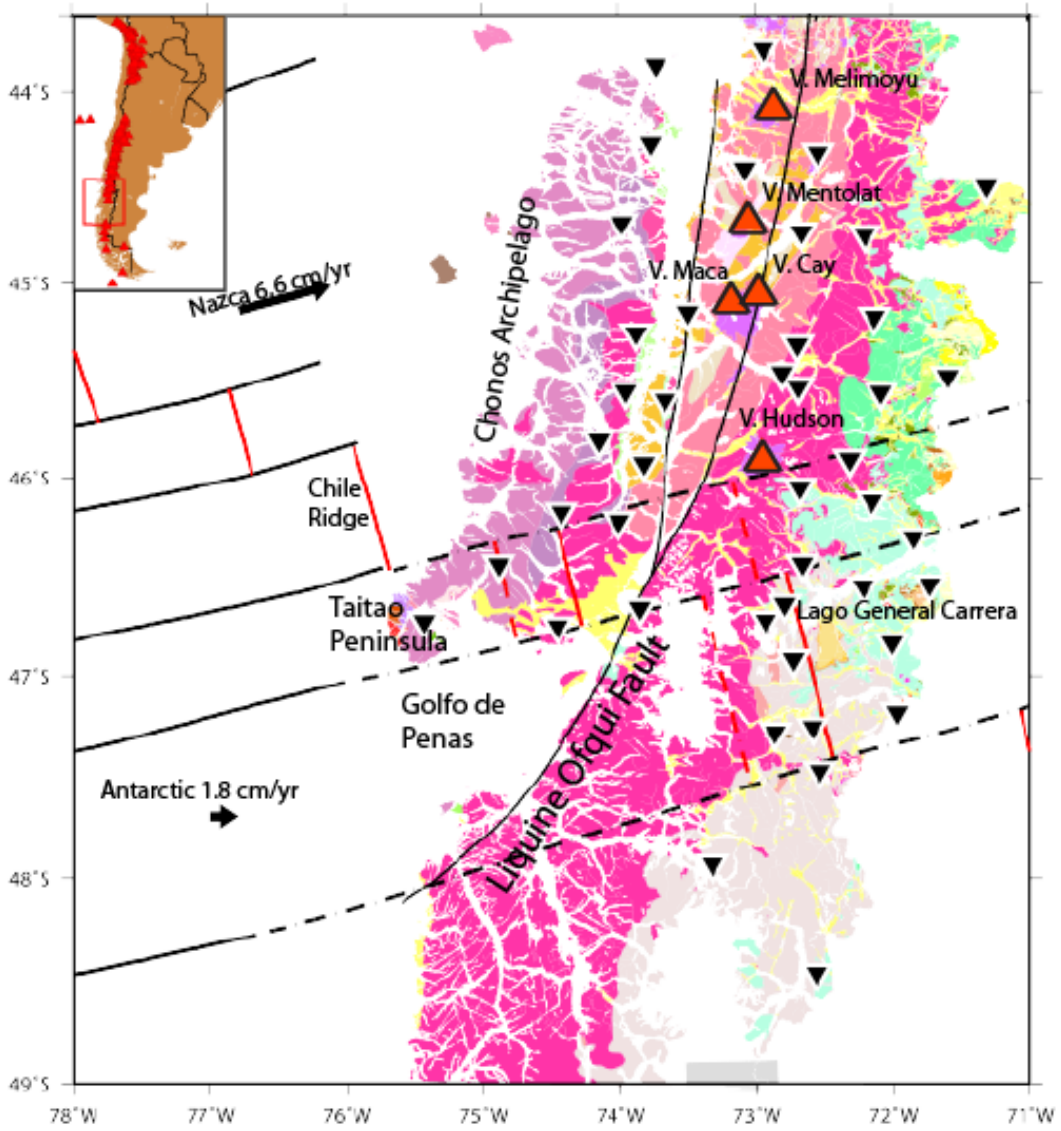


Figure 1-3. Geologic map of CTJ region, modified from Escobar (1980). Black inverted triangles represents seismic stations. Red triangles represent volcanoes. Red line indicates Chile Ridge segments. Black line indicates transform faults and fracture zones. Segmented lines indicate subducted transform faults and fracture zones.

#### Sedimentary Sequences

 Pleistocene-Holocene  
Alluvial, glacial, deltaic, coastal deposits.

#### Volcano-Sedimentary Sequences

 Lower Cretaceous  
Volcanic sequences. Basaltic to andesitic lavas and breccias, andesitic to rhyolitic pyroclastic rocks and sedimentary intercalations. Patagonian Range.

 Jurassic  
Volcanic sequences and centers : dacitic to rhyolitic pyroclastic rocks, andesitic lavas and sedimentary intercalations. Patagonian Range.

#### Volcanic Rocks

 Quaternary  
Stratovolcanoes and volcanic complexes: basaltic to rhyolitic lava, domes and andesitic to basaltic pyroclastic deposits. Patagonian Range.

 Miocene  
Serpentinite, gabbro, dikes and pillow lava with limonite intercalations. Taitao Ophiolite.

#### Intrusive Rocks

 Miocene (MPB)  
Granodiorite, diorite, tonalite. Central part of North Patagonian Batholith.

 Lower Cretaceous (LCPB)  
Granite, granodiorite, tonalite. North Patagonian Batholith.

#### Metamorphic rocks

 Triassic (WMC)  
Mica schist, phyllites, metasedimentaries. Western Metamorphic Complex.

 Triassic (WMC)  
Metaturbiditic sequence. Western Metamorphic Complex.

 Devonian-Carboniferous (EMC)  
Metasandstone, phyllites, marble, chert, metabasalt, metaconglomerate. Eastern Metamorphic Complex.

Figure 1-4. Continuation Figure 1-3

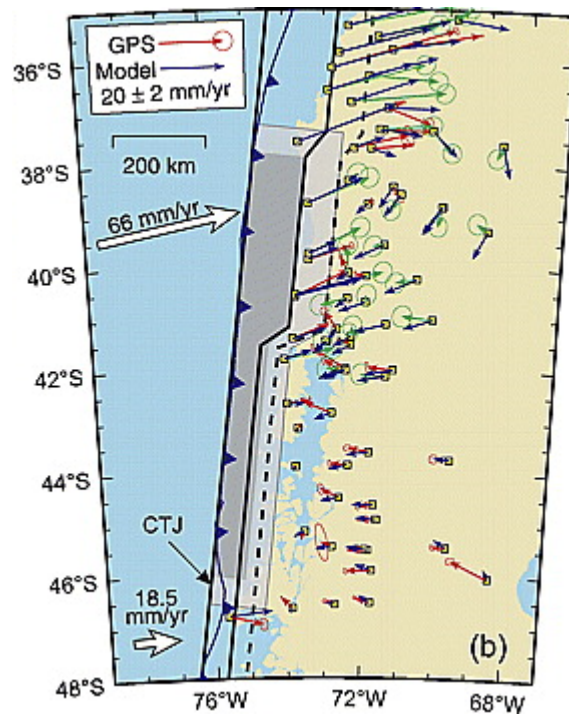


Figure 1-5. Viscoelastic numerical model from GPS observations. Squares indicate locations of GPS sites. Dark shading represents the rupture zone of the 1960 M 9.5 Chile earthquake. Light shading represents the coseismic transition zones. Thick solid and dashed lines outline the locked and interseismic transition zones, respectively (Wang et al. 2008).

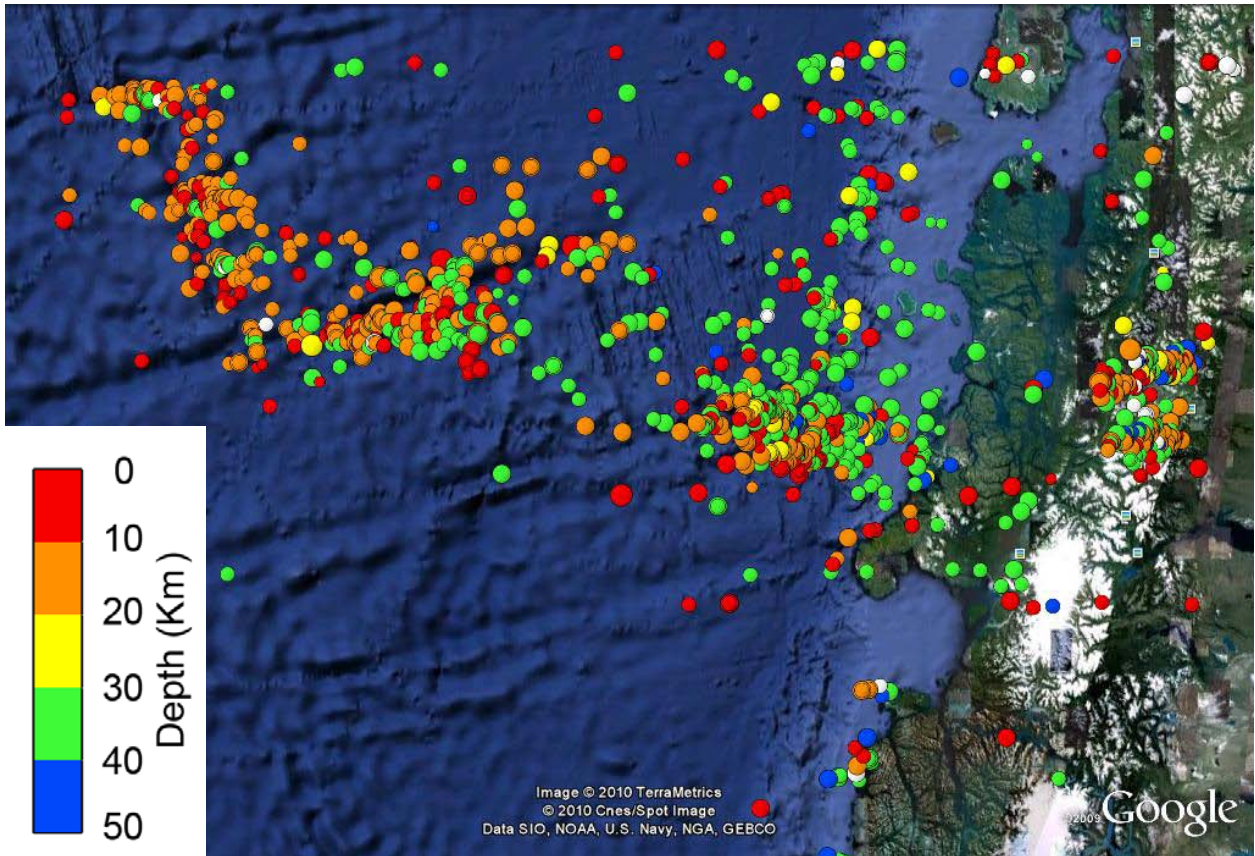


Figure 1-6. Seismic events from 1964 to present (IRIS DMC catalog). Background image: Google Earth.

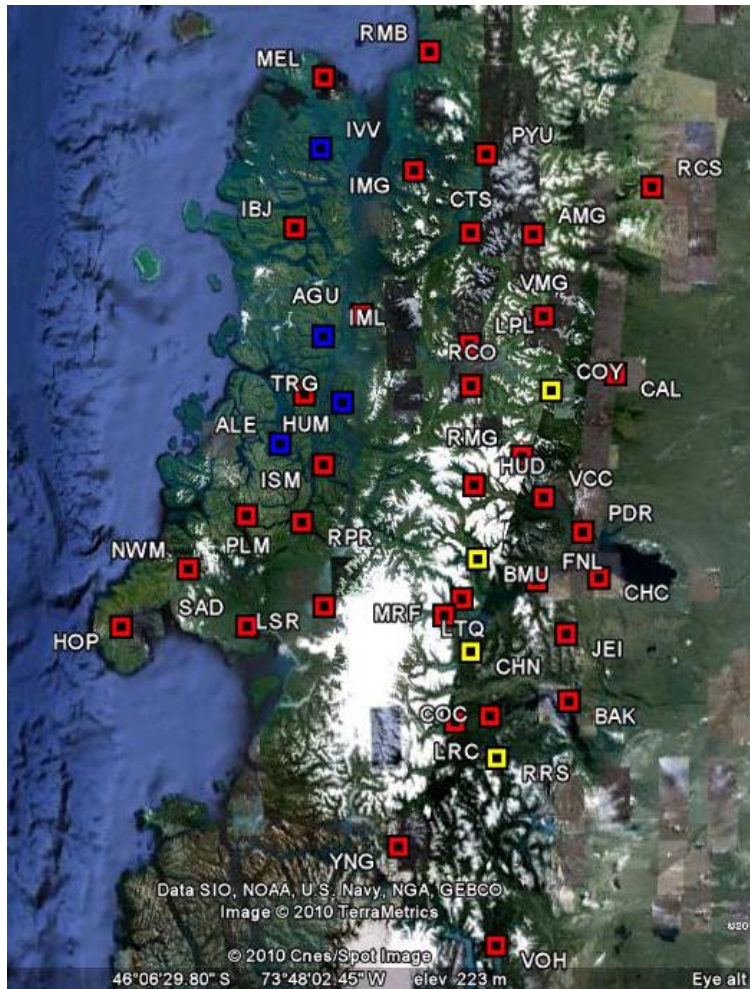


Figure 1-7. Details of seismic network. Red squares, STS-2 broadband sensors, yellow squares, fat stations composed of a Guralp broad sensor and a special arrangement of 3-4 short period L22 sensors. Blue squares, short period sensors. Background image: Google Earth.

## CHAPTER 2 NON VOLCANIC TREMORS AT THE CHILE TRIPLE JUNCTION

### 1.4 Introduction

Non volcanic tremor (NVT) is a weak, 1-10 Hz seismic signal with extended duration of hours to days, with no clear P or S waves. It has been observed episodically at different subduction zones: Nankai in Japan (Obara 2002), Cascadia (Rogers and Dragert 2003), Chile (Gallego et al. 2006), Costa Rica (Brown et al. 2005, Brudzinski and Allen 2007), Oaxaca (Payero et al. 2008), Alaska (Peterson and Christensen 2009), and Taiwan (Peng and Chao 2008), and along the San Andreas Fault (Nadeau and Dolenc 2005). At subduction zones well-located NVT lie in a belt-like zone that follows the 30-40 km iso-depth curves (Shelly et al. 2006). NVT is believed to result from shearing on faults at high pore pressure (Obara 2002, Shelly et al. 2006).

Occasionally, periods of high NVT activity correlate in time and location with the occurrence of Slow Slip Events (SSE). These coupled phenomena are called episodic tremor and slip (ETS) (Rogers and Dragert 2003, Obara et al. 2004). SSE are observed as a sudden motion of the overriding plate in the opposite direction of the subducting plate convergence. The signal is aseismic, but is detected with continuous GPS networks (Dragert et al. 2001, Lowry et al. 2001). There is no clear relation between SSE and major earthquakes, and their duration is variable, generally lasting for weeks or months. In the Cascadia subduction zone, a slip of 2 cm in an area of 200 x 500 km occurred over 15 days, producing energy equivalent to a magnitude 6.7 earthquake. This sudden motion of the surface is interpreted as slip on the interplate interface, down-dip from the locked section of the seismogenic zone (Dragert et al. 2001). One possible interpretation for the mechanism of SSE is the concept of patches analogous to asperities along faults that rupture during earthquakes (Lay and Kanamori 1981),

in which stronger patches with stick-slip behavior are surrounded by larger regions of stable slip (Ito et al. 2007).

Another important characteristic of tremors is their migration. Along Japan's Nankai Trough, NVT locations apparently migrate along the strike of the subduction zone at about 13 km/day (Obara 2002). This migration does not always occur, and sometimes clusters of activity appear randomly in different parts of the slab. Another type of migration appears when successive low frequency earthquakes (LFEs) within the tremor signal migrate in the down-dip direction of the slab at about 45 km/h, much faster than NVT migration along strike (Shelly et al. 2007).

There are two main processes invoked to explain the generation of NVT. The first is the release and rise of fluids from dehydration of the subducting slab; this process is similar to volcanic tremors due to movement of magma or hydrofluids passing through volcanic conduits. Large amounts of water accumulate in the slab due to hydrothermal activity at mid-ocean ridges (Peacock 1990) and to infiltration of water in normal faults formed during the bending of the slab at subduction zones (Ranero and Sallares 2004, Ranero et al. 2006, Faccenda et al. 2009). NVT occur at depths where prograde metamorphism in the slab releases high volumes of fluid (Peacock 1990). These fluids migrate to the slab surface, at high pressure, and result in hydraulic fracturing, and, presumably, the long duration of the tremors occurs due to a chain reaction where the high pressure fluid activates or creates new fractures (Obara 2002). However, a second process is also invoked, one similar to slip during earthquakes, that occurs when a series of near-continuous LFE's are detected as tremors. LFE's were identified for the first time in the Nankai subduction zone (Katsumata and Kamaya 2003) and later within the NVT signal (Obara and Hirose 2006, Shelly et al. 2007). Precise hypocentral locations and focal

mechanisms of earthquakes can be obtained by analyzing the travel times and polarities of P and S waves. For most NVT such analyses are difficult because of the low amplitudes and lack of clear P and S waves in tremors. To overcome this problem, making use of the unmatched spatial density, and low-noise recordings of the Japanese borehole Hi-NET array in Shikoku, Japan, (Shelly et al. 2006) cross-correlated the waveforms of local earthquakes with those of LFE. They thus obtained P and S propagation delay times allowing good hypocentral determinations. The locations showed that tremors lie in a narrow band dipping parallel to the subducting slab, and around 5-8 km shallower than the Wadati–Benioff zone. Ide et al. (2007) correlated the waveforms of stacked LFE with waveforms of local earthquakes with known focal mechanism. Results of P wave first motion focal mechanisms obtained this way showed that the LFE waveforms were consistent with shear slip on definite planes corresponding to thrust fault focal mechanisms.

The relationship between magnitude and frequency of NVT occurrence appears to be unlike that of earthquakes. For earthquakes, there is a power-law relation between earthquake frequency and magnitude, known in seismology as the Gutenberg-Richter law. In contrast, the relationship between nonvolcanic tremor amplitude and duration is exponential (Watanabe et al. 2007). The difference between the two points to a fundamental difference in the processes of earthquakes and NVT, although exactly how they differ has not yet been determined.

Attempts to identify and characterize NVT automatically have burgeoned since the recognition of the phenomenon in 2002, and now include sophisticated computer algorithms (Wech and Creager 2008, Suda et al. 2009, Husker et al. 2010), but the diversity of NVT amplitudes, frequencies, bursts and peaks have largely defied precise and consistent physical characterization. In this study, durations of NVT signals were identified during two continuous

years (2005 and 2006) in the CTJ area with a maximum duration of 48 h, and a maximum time hiatus of 72 hours, thus demonstrating that these are the most continuously active nonvolcanic tremor signals yet observed anywhere in the world. In order to better understand the possible mechanisms producing these tremors and their unique occurrence, data collected at the Chile Triple Junction were used to characterize the NVT signals, yielding their spectral content, wave propagation characteristics, durations, recurrence properties and, in some instances, epicentral locations.

## **1.5 Methodology**

### **1.5.1 Time Distribution of NVT.**

Time series of NVT occurrence were constructed for each seismic station where such signals were detected (Figure 2-2). NVT signals were observed at only 14 stations located in the Chonos Archipelago and Taitao Peninsula, at sites around 100 km east of the Chile trench. Two years of data (2005 and 2006) were examined visually, and the times of the tremor burst first arrival and its end were determined (Figure 2-2). NVT onset was declared when similar-shaped bursts were noted at a minimum of two stations; given a nominal station spacing of 70 km, this assured that the signals indeed corresponded to NVT and not to local noise, which is inherently uncorrelated and thus not recognizable. For earthquakes, the first arrival of P and S waves are typically impulsive and therefore relatively easy to identify. In contrast, NVT signals are emergent, arising very smoothly from background noise without apparent distinctive peaks. To determine the NVT arrival time and duration with accuracy is therefore difficult, but for the purpose of statistical analysis in this study, resulting errors of a few seconds in arrival time or duration are insignificant compared with hours or days of continuous tremor signal.

### 1.5.2 Hypocentral Determination of Non Volcanic Tremor.

Due to the absence of impulsive waves in the tremor signal, traditional earthquake location methods are not applicable. Instead of using impulsive peaks, the Source Scanning Algorithm (SSA) developed by Kao and Shan (2004) utilizes the signal amplitude in a time window of a few seconds to find the travel time of a given tremor burst between source and stations. This forward modeling method depends on accurate knowledge of model shear wave travel times through a three-dimensional volume of the study region. The study area was parametrized as a grid of 10 x 10 km cells, and, for each, the shear wave travel time between the cell and stations using an assumed S-wave velocity model was calculated based on results of Robertson et al. (2003). The SSA then yields a tremor burst hypocentral estimate by sequentially comparing the observed and calculated NVT travel times and burst amplitudes between each potential source cell and each station where the NVT were observed. We then used a two-step procedure to calculate the maximum brightness function:

$$br(\eta, \tau) = \frac{1}{N} \frac{\sum_{n=-M}^M W_m |u_n(\tau + t_{\eta n} + m\delta t)|}{\sum_{m=-M}^M W_m} \quad (2-1)$$

where N is the number of stations,  $t_{\eta n}$  is the predicted travel time from potential source-cell  $\eta$  to station n,  $\tau$  is the origin time,  $u_n$  is the signal amplitude at time  $t_{\eta n}$ , M is the number of samples used to compute the signal amplitude, and  $\delta t$  is the sampling interval.  $W_m$  is a weighting factor that depends on how much the predicted signal travel time differs from the observed arrival time.

In the first step, the signal was visually inspected to find a clear tremor burst. A suitable portion of tremor signal was selected if it contains relatively high SNR, duration longer than 20

sec, and if it was identified on the same seismometer components (e.g., vertical) at a minimum of 4 stations. The amplitude of each selected seismogram was then normalized. In the second step, the time window selected was processed through the SSA.

The brightness function is therefore a measure of how closely the timing and maximum amplitude of a tremor burst observed at a given station correlates with the timing and observed burst amplitudes at other stations, assuming that all the NVT were produced in the same source cell at the same time. The brightness function increases when the arrival times from the source to each station are close to the maximum amplitude of the signal in a particular time window  $m\delta t$ . To accelerate convergence to a single source cell at a given origin time, the algorithm runs in two steps. First, the travel times are calculated using a velocity grid of 10 x 10 km cells that spans the entire study area (400 x 700 km), and then the grid is reduced to cells of 5 x 5 km in the 100 km<sup>2</sup> around the maximum brightness point calculated in the first step. The time window  $m\delta t$  selected was 2.5 sec. By systematically searching through all  $n$  and  $t$  in the grid for the local brightness maxima, the spatial and temporal distribution of the tremor source was found. Due to imperfections in the assumed velocity model (Robertson et al. 2003), the arrival time calculated may differ from the observed time. To calibrate this error, several local earthquakes were located using the SSA and compared with the hypocentral estimates derived from standard location software (HYPO71; Lee and Lahr, 1972), yielding errors of about 10 km horizontally and 30 km vertically. The vertical error is large enough to preclude resolution of the vertical distribution of tremors, which is in discriminate in possible source mechanisms.

### **1.5.3 Other analysis**

Spectrograms (Figure 2-4 and Figure 2-10) of observed NVT signals show variations in the amplitudes of the frequencies that constitute the signal during a given period of observation. These spectrograms are produced by calculating the frequency content in a time window of 2 s

using a slice of 1 s, distributed over the entire signal. This analysis is potentially useful for source discrimination. Particle motion analysis (Figure 2-6 and Figure 2-10), used to compare relative amplitudes on the three components of the seismogram, was constructed by plotting one of the three components of the seismogram (N, E, Z), on the x-axis, against a different component on the y-axis, for each value of the independent variable, time. This analysis is useful to discriminate whether the process releases energy as shear waves or compressional waves.

## **1.6 Results**

### **1.6.1 Characteristics of NVT at the CTJ.**

The NVT signals detected at the CTJ (Figure 2-1) persist for variable durations from minutes to up to two days, have relatively low signal-to-noise ratios, and frequencies between 1 and 10 Hz, i.e., they are depleted in high frequencies compared with local earthquakes in the same epicentral area (Figure 2-5). The signals are composed of several bursts, similar to tremors found in other subduction zones (Obara 2002, Rogers and Dragert 2003).

### **1.6.2 Time Histograms of Tremor Activity.**

Histograms of tremor occurrence (Figure 2-2) for each station, calculated for the two years of data recording (2005 and 2006), show that tremors occur quasi continuously during intervals that vary from a few minutes to two continuous days, with smooth variations preceding and following a high tremor duration peak. Tremor activity was observed exclusively at stations located in the Chonos Archipelago and on the Taitao Peninsula (Figure 1-1). In accordance with the observed intensity of tremor at the observing stations, tremor activity can be separated into three zones: North of the Chonos Archipelago, where the Nazca plate subducts, between the Guamblin and Darwin transform faults, stations IMG, IBJ, and AGU show minor NVT activity

with durations longer than 3.5 h occurring only 5 times. In the central part of the archipelago, between the Darwin and Taitao FZs, stations HUM, ISM, PLM , RPR and NWM recorded the greatest activity, with NVT durations longer than 17 hours occurring 6 times, and the longest observed duration of continuous tremor activity yet seen in South America, which lasted for 48 hours. South of the Taitao FZs, where the Antarctic plate is subducting, tremor activity at stations HOP and SAD is rare.

### **1.6.3 Non Volcanic Tremor Location**

The tremors that we could locate (Figure 2-12) occurred in a band of epicenters about 50 km wide along the Chonos Archipelago and Taitao Peninsula, lying around 60 to-80 km east of the trench. The tremors lie well west of the Liquine-Ofqui fault zone and the recently-active volcanic centers of the Southern Volcanic Zone. They are separated into two clusters about 125 km apart which differ in activity: one very active cluster in the south, mostly centered on the Taitao Peninsula, and a less active cluster in the north centered on the eastern Chonos Archipelago. Analysis of the tremor depth distribution is more difficult due to the small number of stations deployed and the lack of a truly detailed velocity model for this area. As is typical for earthquakes, CTJ tremor hypocenters are more uncertain than their epicenters because the wide station spacing (40 km on average) means the vast majority of tremor do not lie directly beneath a station, and so there is no observed travel time for a strictly vertical path to constrain tremor depth. The tremors we could locate are distributed (Figure 2-14) from the surface to 80 km depth, with a peak of occurrence at  $30 \text{ km} \pm 10 \text{ km}$  (Figure 2-15). Vertically, the two clusters occupy an elongated volume separated horizontally by a gap.

### **1.6.4 NVT Frequency of Occurrence.**

The relationship between earthquake magnitudes and frequency of occurrence is quantified by the Gutenberg-Richter law (Gutenberg and Richter 1945):

$$\log N = a - bM \quad (2-2)$$

where  $N$  is the number of events with a magnitude greater than  $M$ , and  $a$  and  $b$  are constants that depend on the number of earthquakes in a given region. This relation has a fractal behavior because the same relation is found in small and large seismic areas, except for the largest earthquakes.

To explore the relationship between NVT duration and frequency of occurrence, two years (2005 and 2006) of tremor time series were analyzed (Figure 2-2). Tremor duration was plotted against cumulative frequency of occurrence with a 10 min interval. The cumulative frequency expresses the number of tremors with duration greater than or equal to time  $T$  as a function of  $T$ . The resulting curve (Figure 2-16) shows a progressive decrease in the number of tremors with the increase of tremor duration. The curve fits a power-law trend with a correlation coefficient of 0.97 and an exponential trend with a coefficient of 0.76. Therefore, a power law is more appropriate than an exponential law to express the quantitative relationship of the data. The equation obtained that expresses this relation is:

$$\log N = c - d \log T \quad (2-3)$$

where  $N$  is the number of tremors with duration equal to or larger than  $T$ ,  $c = 7$  and  $d=1.95$ . Duration magnitudes for small earthquakes ( $ML < 3$ ) derive from empirical relationships which are highly dependent on local conditions and instrument corrections; however, they all have a logarithmic dependence on event duration (Lee et al. 1972, Castello et al. 2007). Thus,  $\log T$  in tremors is proportional to the tremor magnitude and equation (2-3) is comparable to a Gutenberg-Richter law (2-2).

### **1.6.5 Low Frequency Earthquakes**

Within the tremor signal, on rare occasions, two consecutive impulsive waves appear, the second larger in amplitude than the first (Figure 2-7 and Figure 2-8). The delay time (Figure 2-9) between these two peaks increases with epicentral distance, suggesting that these are seismic signals that propagate at P- and S-wave velocities. The frequency content of these waves (Figure 2-10) is strongly concentrated between 1 and 10 Hz, and particle motions (Figure 2-10) of these peaks are consistent with a primary P-wave oscillating in the vertical plane and a secondary S-wave oscillating in the horizontal plane. Compared to NVT and local earthquakes ( $M_w < 1$ ) from the same epicentral area, their spectral content (Figure 2-11) is similar to that of NVT, but their amplitudes are smaller than those of the local earthquakes. These waves have been recognized in other regions (Katsumata and Kamaya 2003, Shelly et al. 2006) and termed low frequency earthquakes (LFE). The locations of LFE in the CTJ region (Figure 2-12) coincide with the distribution of NVT clusters, but their depths are shallower, distributed between the surface and 40 km deep.

## **1.7 Discussion**

The characteristics of the NVT signal in the CTJ region are similar to those of NVT in other regions (Obara 2002, Rogers and Dragert 2003, Brudzinski and Allen 2007, Payero et al. 2008, Peng and Chao 2008, Peterson and Christensen 2009). We observe tremor durations of hours to days, a frequency range between 1-10 Hz (Figure 2-4), depletion of higher frequencies with respect to spectra of local earthquakes (Figure 2-11), and propagation at shear wave velocities because the signals are large amplitude on horizontal component (Figure 2-6). Histograms of tremor activity during the two years of recording (2005 and 2006) vary smoothly and peaks of long-duration activity seem to be separated by 30 to 40 days. In contrast to other subduction zones where tremors occur episodically in intervals of months (Rogers and Dragert

2003, Obara et al. 2004), NVT at the CTJ are the most active in the world with just 72 hours of NVT hiatus during two years of observation. Stations that recorded major activity (ISM, PLM) show 8 peaks with durations greater than 15 hours. The long signals, composed of several bursts of variable amplitude, shape and duration, indicate that tremors may be produced by a quasi-continuous single-event process, a quasi-continuous process of a chain of events, or a continuous process that is only perceptible when for some reason the amplitude of the signal is greater than the background noise.

The tremor signal also contains sporadic LFE, with distinctive P and S waves, similar to those found in Japan (Katsumata and Kamaya 2003). These LFE are enriched in low frequencies (1-10 Hz) and depleted in high frequencies compared to those of local earthquakes. The variations of the frequency spectra (Figure 2-11) are similar to that of NVT, although their amplitude spectral peaks are greater, supporting the idea of a common source mechanism (Shelly et al. 2007).

Located tremors occur in a distributed zone with a depth range of over 80 km (Figure 2-14) and a peak of occurrence at about 20-30 km depth (Figure 2-15). Accurate tremor locations are critical to understanding the mechanism that produces them. In the Cascadia subduction zone (Kao et al. 2005), located tremors in a distributed zone (depth range of over 40 km), very similar to this study's findings using data from a similarly-spaced seismic network and the SSA technique. However, Shelly et al. (2006) used cross-correlation and double difference to confine LFE observed in Shikoku to a narrow zone dipping parallel to the subducting plate, and a few km above interplate interface. If the Chilean NVT are similar to those in Shikoku, they probably also occur near the Nazca-South America interplate interface.

The geometry of the shallow slab in the CTJ is poorly known, but given the distance of

the tremor cluster from the trench of about 100 km, and a nominal subduction angle of 20 degrees, and assuming tremors occur along or near the interplate interface, the location of the tremors maximum at 20-40 km depths is similar to that observed for Shikoku (Shelly et al. 2006).

The more vigorous NVT activity beneath the south compared with those in the north, is probably related to the differential proximity of the Chile ridge to the trench and the proximity of the southern cluster to the slab window. The central part of the very active southern cluster (46°S) is located 105 km from the Chile Ridge, but the less active northern cluster (45°S) is 343 km from the Chile Ridge (Figure 2-13). In the Cascadia and Shikoku subduction zones, NVT occur where relatively young (< 20 Ma), warmer oceanic plates subduct beneath the overriding plate (Peacock 2009). In southern Chile at 44°S numerical models predict temperatures similar to Cascadia subduction zone (Oleskevich et al. 1999); south of 44°S where tremors were observed to occur, the proximity of the Chile Ridge should increase temperature gradients even more. South of 41°S, GPS data show a decrease of landward motion of coastal sites and an anomalous seaward motion of inland sites (Figure 1-5). This southward decrease in distance between the Chile Ridge and the trench increases the temperature in the slab, narrowing the seismogenic zone toward the south and leading to increased stable slip (Wang et al. 2008). In addition, high amounts of water accumulated prior to subduction due to hydrothermal processes are released in the subducted slab during dehydration processes (Peacock 1990, Peacock and Wang 1999). This dehydration and dewatering almost certainly increases the fluid pressures in the slab interface, reducing the effective normal stress on any fault surface present. Increased pore pressure in a network of intermittently connected fractures should facilitate fault slip, enhancing the occurrence tremors, LFE (Shelly et al. 2006) or the escape of fluids producing

NVT (Obara 2002).

The IRIS CMT earthquake catalog (Figure 1-6) shows that the most active faults offshore are the Guafo, Guamblin, and Darwin transform faults, with some more minor activity near the subducted Taitao and Tres Montes subducted transform faults. Also, lineaments of inland local earthquakes parallel to the subducted Taitao and Darwin transform fault indicate that seismic activity of these transform faults continues after subduction (Murdie et al. 1993). The locations of NVT clusters coincide with the locations of subducted transform faults and fracture zones beneath the Chonos Archipelago (Figure 2-12). The southern, high tremor activity cluster appears immediately north of and above the subducted Taitao transform fault and south of Darwin FZ, and the less active cluster in the north coincides with the subducted Guamblin FZ. The Taitao transform faults generated a slow earthquake (as part of the aftershock sequence of the Great 1960 Chile earthquake) with a rupture process which lasted more than 1 h, indicating that the subducted oceanic transform fault can slip by quasi-seismic creep (Kanamori and Stewart 1979). However, the NVT epicenters are dispersed rather than striking parallel to the fracture zones. Additionally, the subducted Taitao transform fault now forms the southern boundary of the subducting Nazca plate, and, in consequence, is the edge of the slab window exposed to the asthenospheric mantle (Russo et al., 2010a,b), although seismic activity on this principal plate boundary fault plane is frequent enough to be distinguished from background (Murdie et al. 1993). Slip on the shear zone of the plate edge could occur by dragging of the mantle. The minor tremor activity in the northern cluster may be related to reactivation of the Guamblin and Darwin fracture zones during subduction. This reactivation results from changes in vertical and horizontal stresses during subduction (Nakajima and Hasegawa 2006). Note that NVT generation in transform faults is also observed, for example

along the San Andreas transform boundary (Nadeau and Dolenc 2005, Shelly et al. 2009), where they form a recurrently active lineament striking parallel to the fault at depth of 26 km well below the seismogenic zone (Shelly et al. 2009). Since oceanic transform faults accommodate most relative plate motion aseismically (Ihmle et al. 1993, McGuire et al. 1996), a slip mechanism that produces NVT may be a good candidate to compensate the observed slip deficit. Moreover, the seismogenic zone in transform faults is strongly controlled by temperature (Behn et al. 2007). In the southern cluster, the proximity of the Taitao and Darwin transform faults and fracture zones to the Chile Ridge increases the temperature gradient, elevating the isotherms so faults can slip aseismically, thus facilitating the occurrence of NVT. Accurate locations and focal mechanisms of both tremors and low frequency earthquakes are necessary to truly understand the origin of NVT at the CTJ, and to determine the tectonic regime in which they occur: on or near the inter-plate interface, on subducted transform faults, or both. At the CTJ, two factors probably control the distribution and activity of tremors: temperature, as indicated by the tremor cluster locations with respect to the active, unsubducted portion of the Chile Ridge, and high pore pressures in or near interplate interface and within the overriding plate. High pore fluid are likely present due to the dehydration of minerals that were altered by hydrothermal processes during lithosphere formation at the Chile spreading ridge, and also potentially due to infiltration of water in reactivated crustal normal faults during slab bending (Ranero and Sallares 2004, Ranero et al. 2006, Faccenda et al. 2009).

The cumulative frequency of tremor duration (Figure 2-16) shows a power law trend similar to the Gutenberg-Richter law for moment magnitude. A model based on scale invariance assumes that the frequency of a given size earthquake is inversely proportional to the area of the fault involved (Aki 1989):

$$\log N = c - \log S \quad (2-4)$$

where  $S$  is the fault area and  $c$  is a factor depending on the fault shape. The time of rupture propagation,  $T_R$ , during an earthquake is proportional to the area of the fault,  $L$ , and inversely proportional to the velocity of rupture,  $v_R$ , i.e.,  $L = v_R T_R$ . If tremors are a product of fault slip, and  $T_r$  is the tremor duration, the logarithmic relation between tremor duration and tremor frequency of occurrence found in this study (2-3) can potentially be explained by two mechanisms: tremors occur on a single fault, and tremor duration increases logarithmically with the area of the fault; or, tremor duration increases logarithmically with the number of faults that slip in a chain reaction, with tremor duration proportional to the number and size of these faults.

## 1.8 Conclusion

Nonvolcanic seismic tremors in the CTJ subduction zone region are similar to those observed in the Japan and Cascadia subduction zones: long duration signals lasting from hours to days, depleted in high frequencies relative to earthquakes, and occurring in conjunction with LFEs within the tremor signal.

Chilean NVT and LFE lie in a band parallel to the strike of the Nazca slab, dispersed within a narrow elongated area of 100 km width lying 100 km east of the trench. The NVT do not coincide with either recently active volcanic centers or the Liquine-Ofqui fault zone. The wide depth distribution of NVT (0-80 km), with peak occurrence at 30 km, and the depths of LFE within 40 km of the surface, indicate that both phenomena occur mostly near the plate interface and within the overriding South American plate. Two clusters of NVT activity, one very active in the south and another less active in the north, can be explained by different thermal and pore pressure conditions. The proximity of the active Chile Ridge and slab window

to the southern cluster increases the temperature gradient, thereby narrowing the area of the seismogenic zone, thus allowing aseismic fault creeping. Additionally, the oceanic Nazca plate, fractured by normal and strike-slip faults formed prior to subduction, accumulated ocean water within minerals of its altered crust and then released this water later during dehydration of the subducted slab. This process increases the pore pressure and decreases the effective normal stress necessary for faulting. The frequency of occurrence of Chilean NVT is well represented by a power law, revealing a direct relationship between tremor duration and the number and size of faults involved in their production.

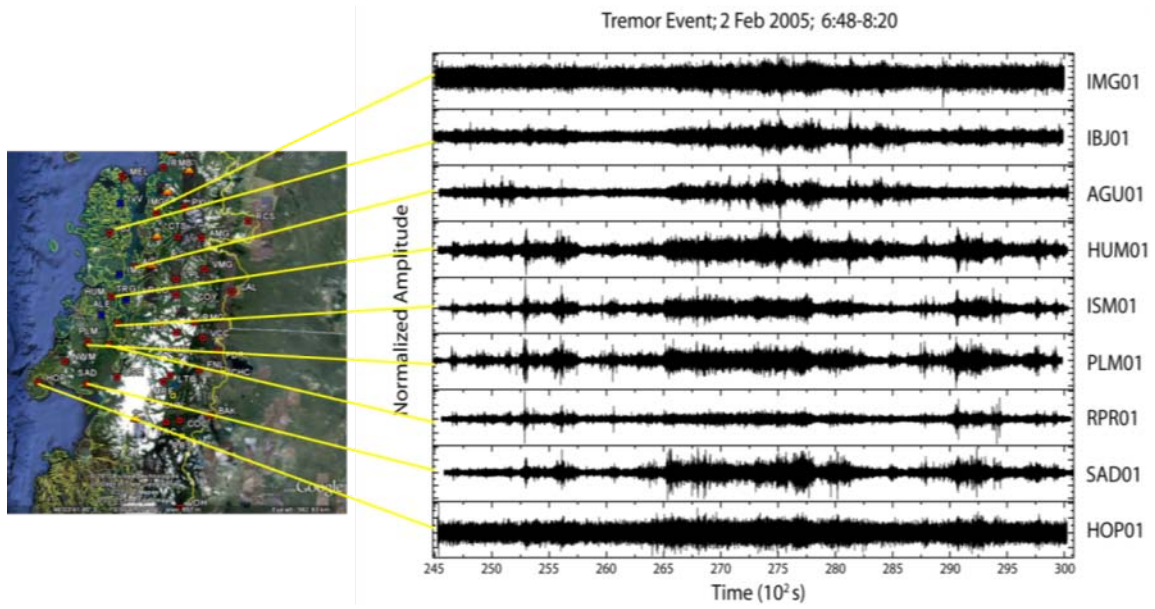


Figure 2-1. Non volcanic tremor waveform. More than one hour of signal detected at 9 stations located along the Chonos Archipelago. Stations at the top (north) and bottom (south) are separated by more than 350 km.

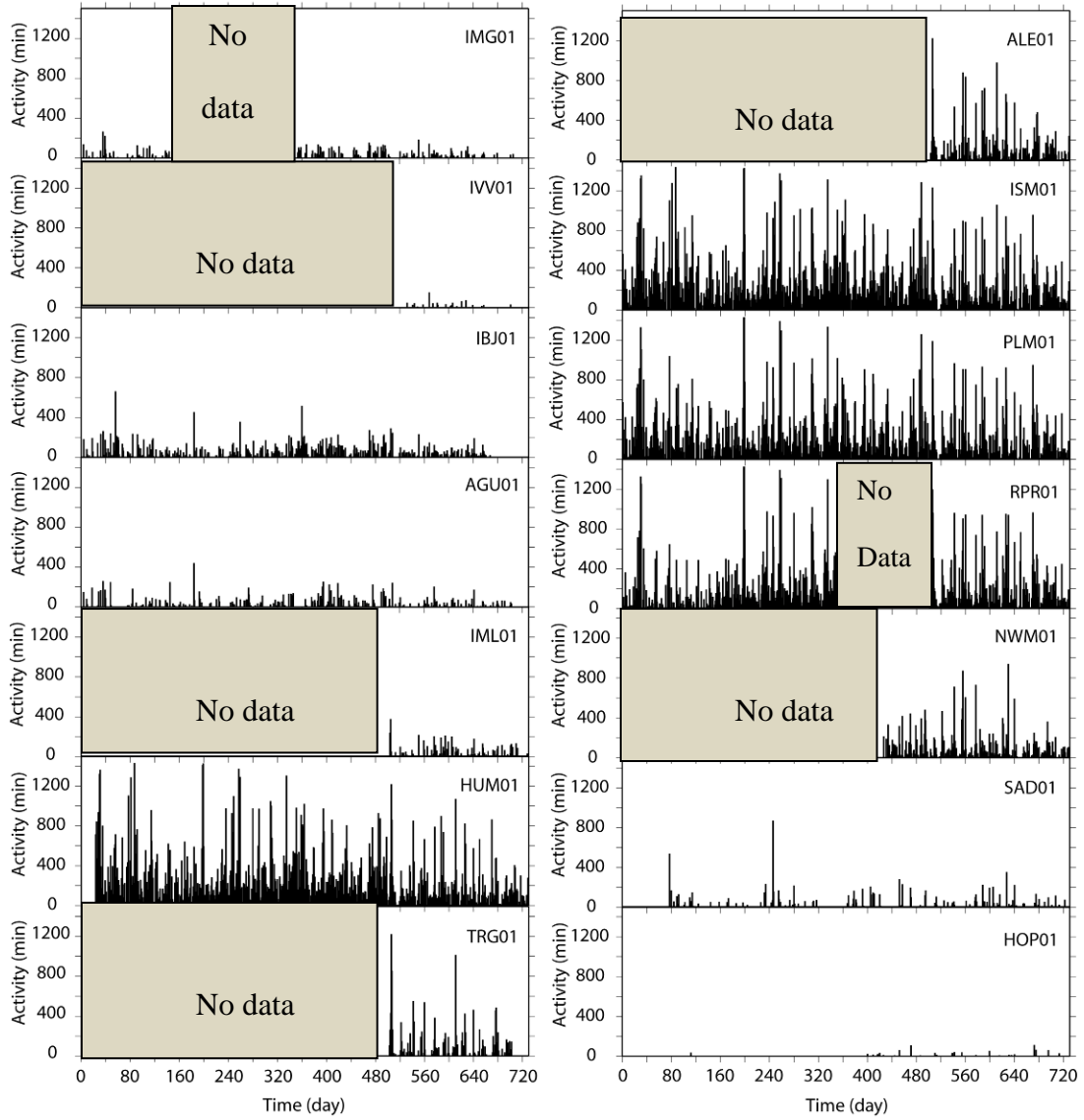


Figure 2-2. Time series analysis of NVT. Dark bars represent tremor duration in minutes per day during two years of data recording (2005 and 2006).

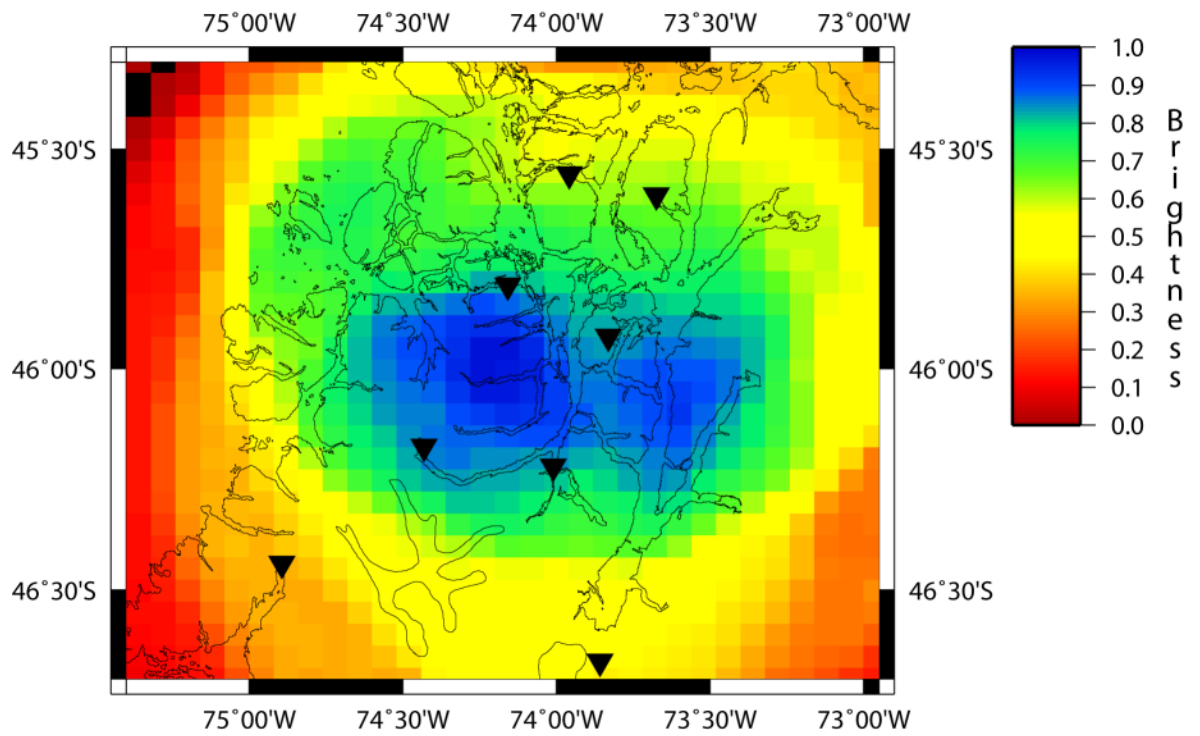


Figure 2-3. Brightness function calculated for a tremor burst: blue colors represent an increase in the average amplitude for travel time calculated from a cell grid to all stations shown (inverted black triangles).

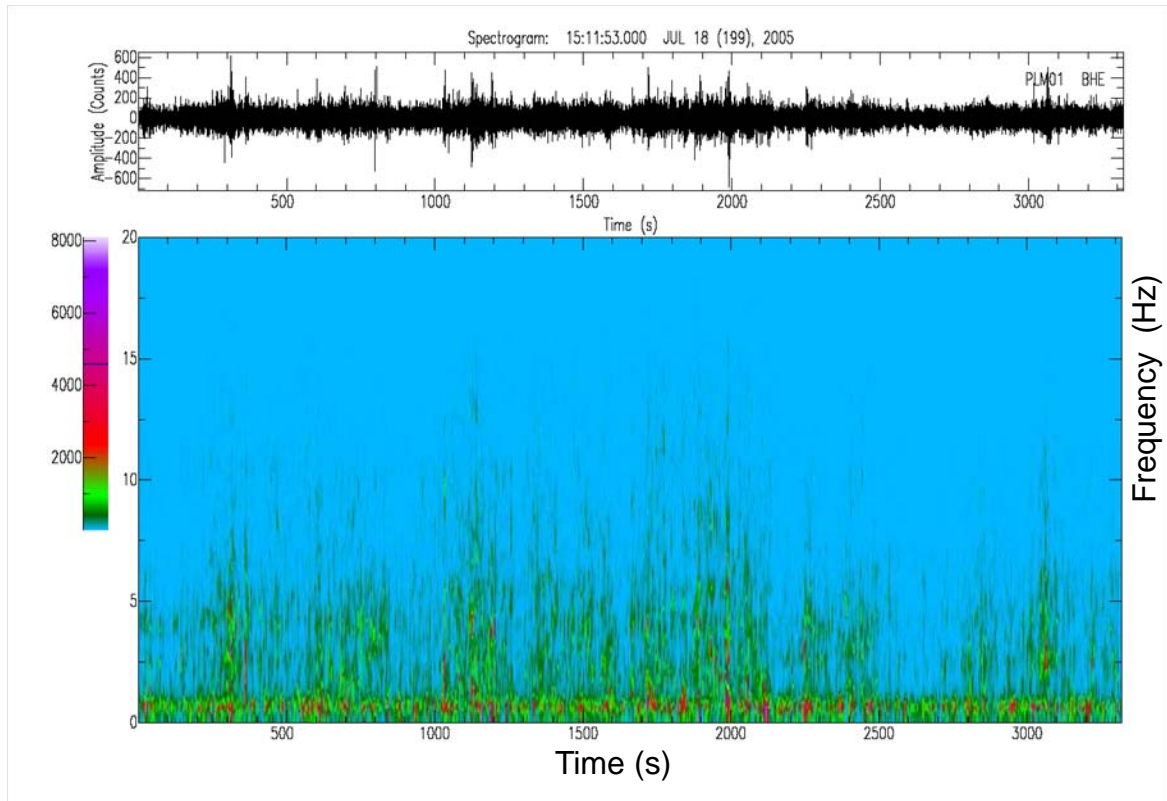


Figure 2-4. One continuous hour of tremor signal (top) and spectrogram (bottom). Color bar (center left) indicates power spectrum of frequency content. Tremors visible as small bursts of signal above noise in the seismogram at top correspond to patches of elevated power (green-red) in the spectrogram below. Note the tremor power is concentrated between  $\sim 1 - 10$  Hz.

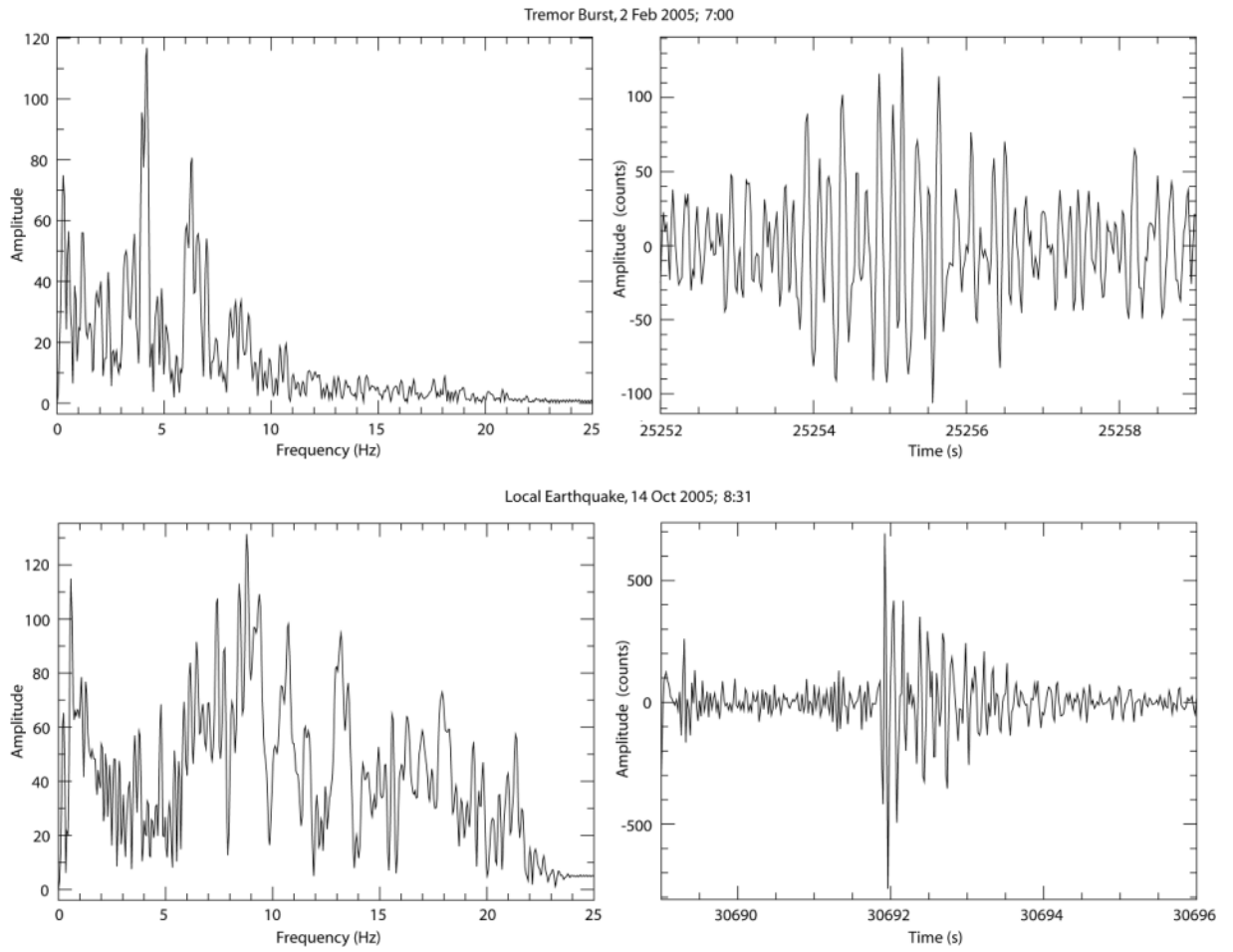


Figure 2-5. Comparison of a tremor burst and local earthquake near the epicentral area of NVT. Frequency analysis. (A) Spectral content of tremor burst. (B) Seismogram of tremor burst. (C) Spectral content of local earthquake (D) Seismogram of local earthquake.

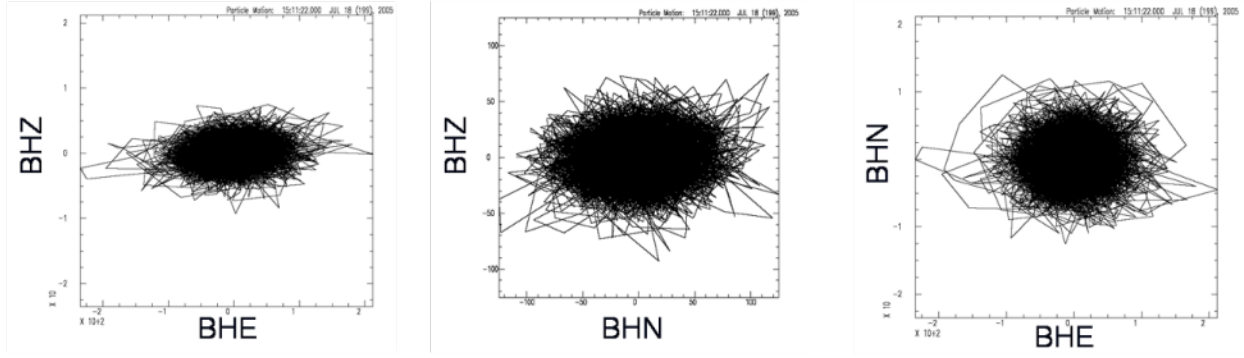


Figure 2-6. Particle motion diagram of NVT signal. BHZ, vertical component; BHN, horizontal N-S component; BHE horizontal E-W component. Note the more energetic motion on the horizontal components, indicating the tremors propagate primarily as S waves.

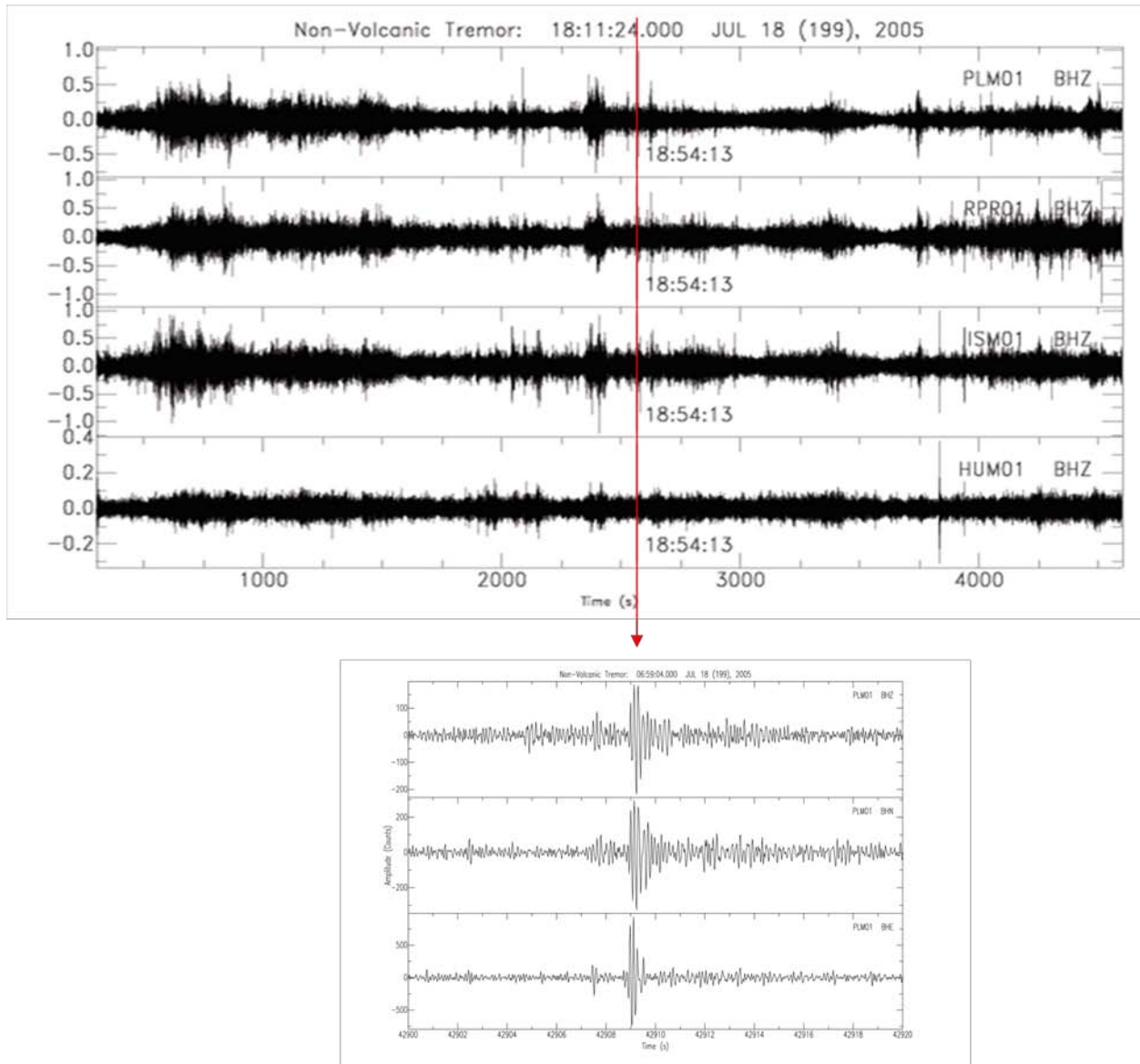


Figure 2-7. Amplification of a LFE within tremor signals (top) observed at 4 stations (PLM, RPR, ISM, HUM). Red arrow indicates time of the LFE in the raw seismograms, top. Amplified signal (bottom) represents 20 s of seismogram at station PLM.

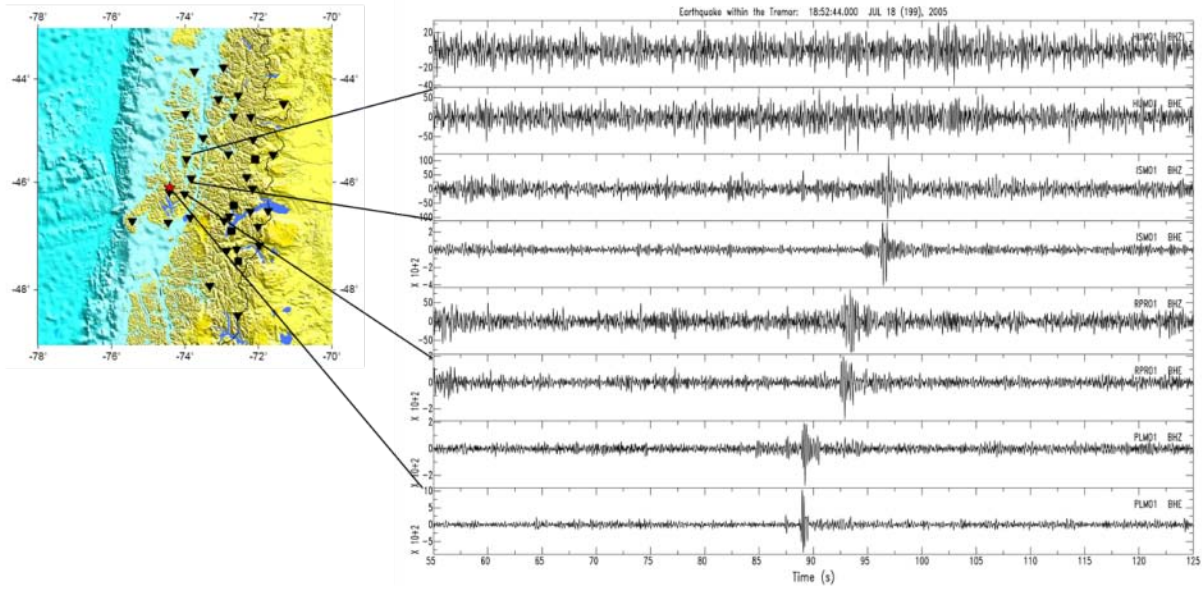


Figure 2-8. Epicentral location of LFE using vertical (BHZ) and horizontal (BHE) arrivals of P- and S-waves at 4 stations (HUM, ISM, RPR, and PLM). Red star indicates epicentral location.

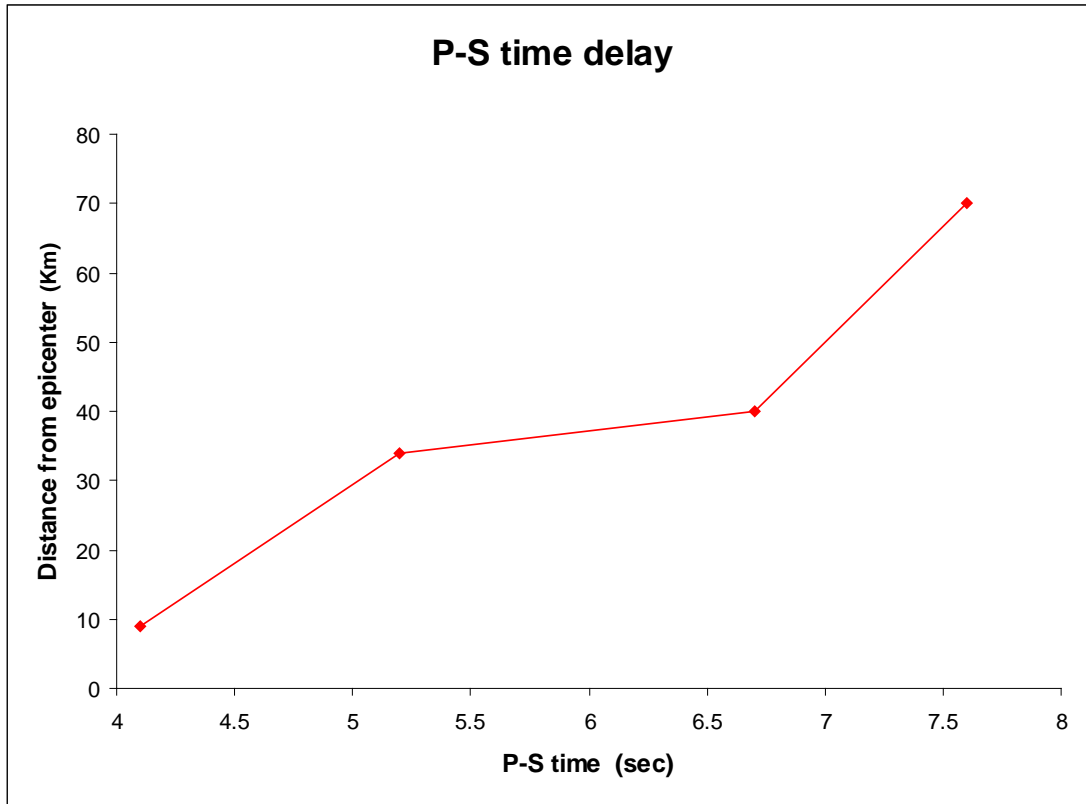


Figure 2-9. Delay time between P and S waves for a LFE. Red dots are S-P time for stations located at 10, 34, 39 and 72 km from the epicenter.

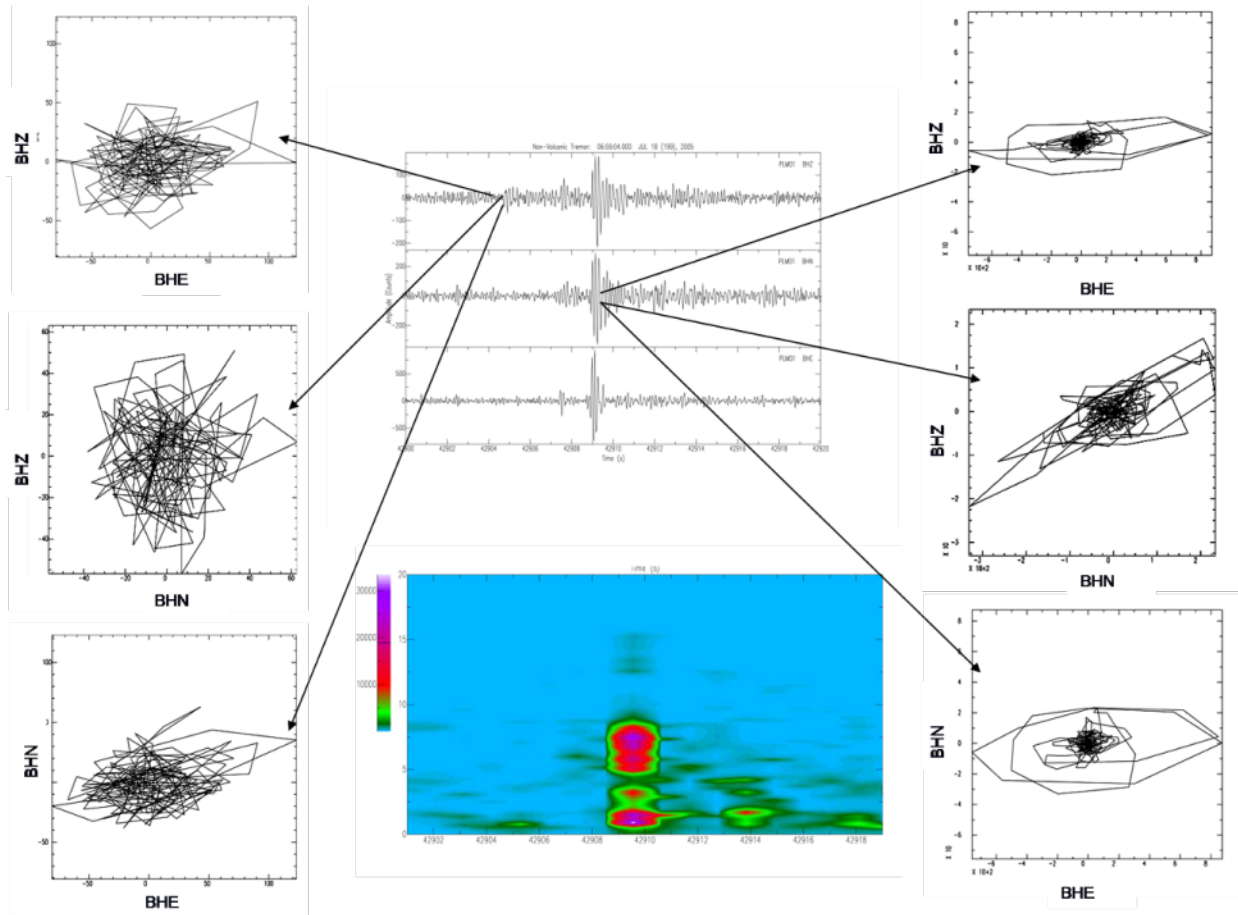


Figure 2-10. LFE earthquake analysis. Particle motion diagram of P- (left column) and S-wave (right column) and spectrogram (center, bottom).

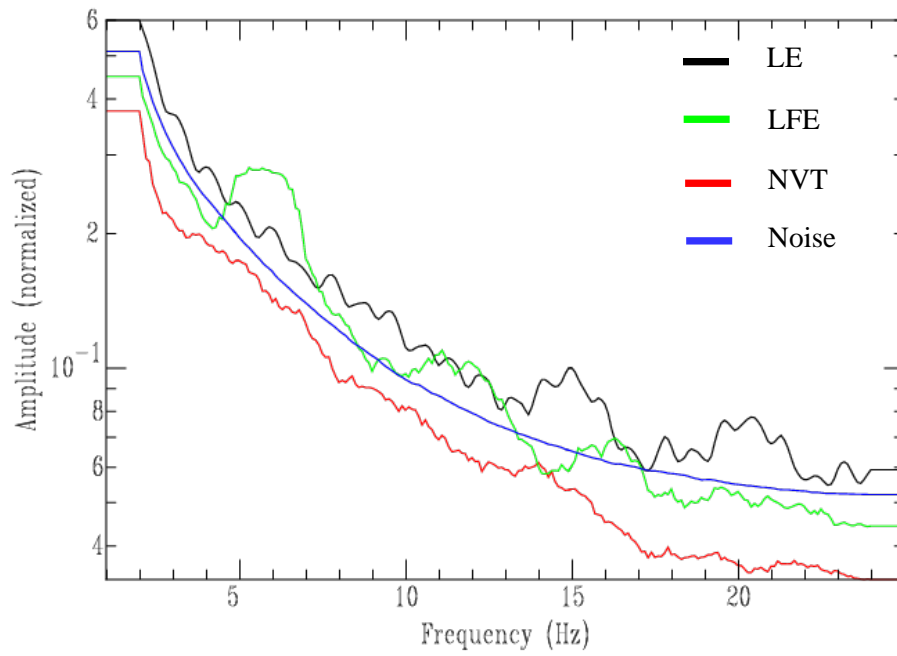


Figure 2-11. Frequency comparison between Local Earthquakes (LE), low frequency earthquakes (LFE), non volcanic tremor (NVT), and background noise.

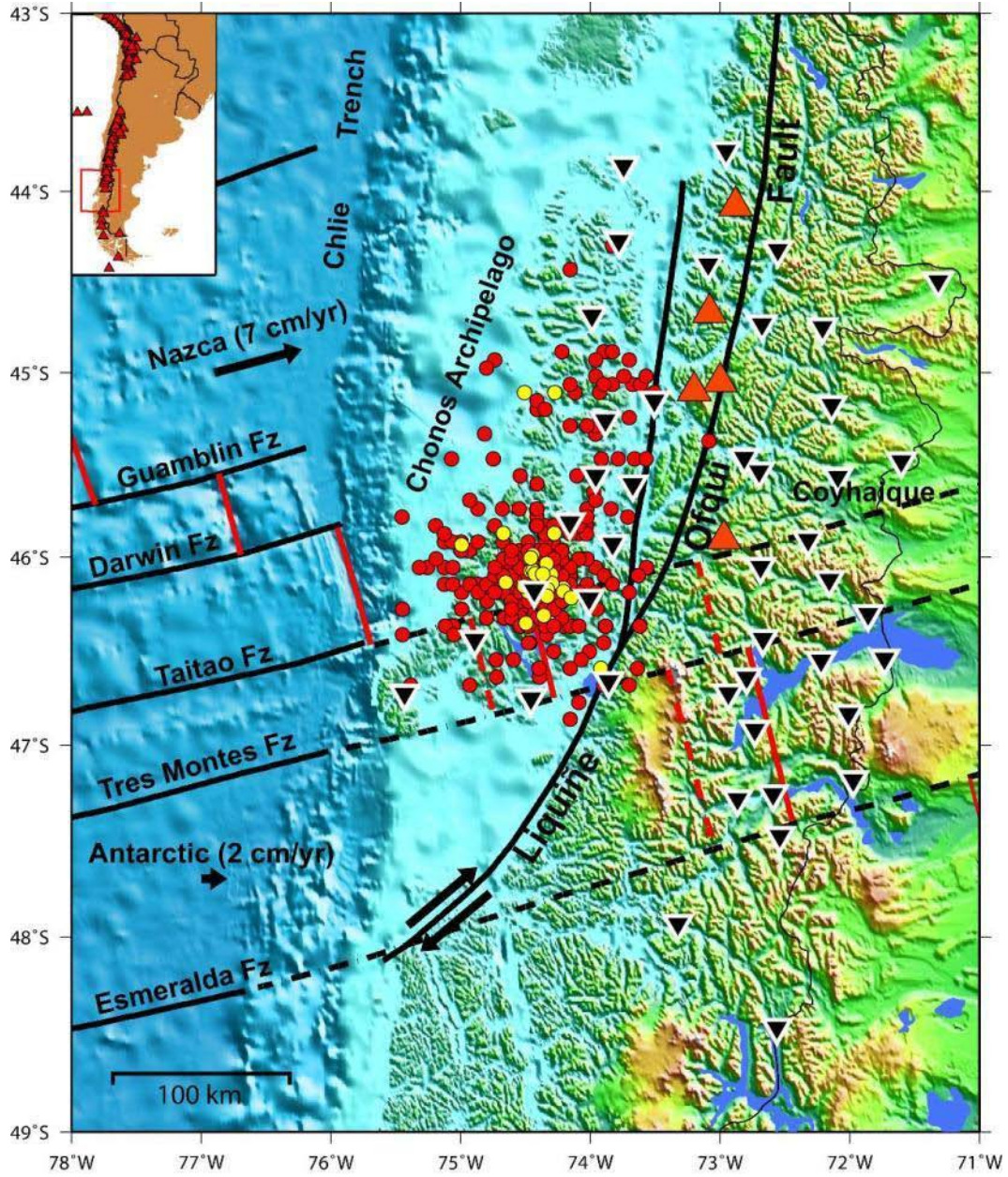


Figure 2-12. Epicentral locations of NVT and LFE. Red dots represent epicenters of tremor bursts found using the SSA algorithm. Yellow dots are epicenters of micro-earthquakes and LFE within tremors, located using HYPO71.

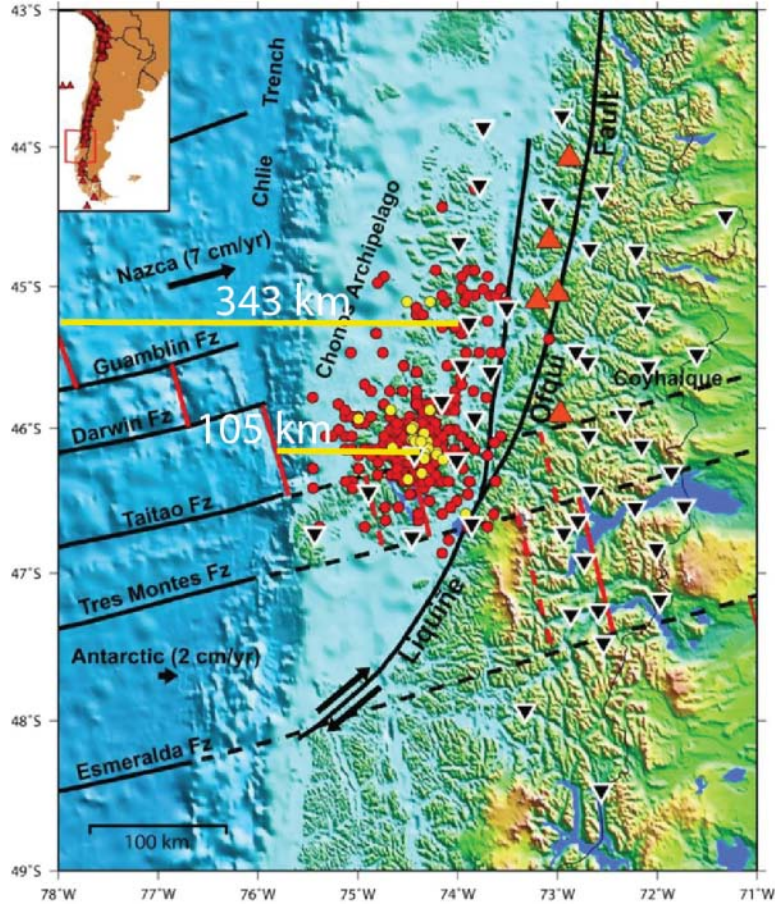


Figure 2-13. Yellow lines represent the distance (white numbers) from the active Chile ridge to the center of the northern and southern cluster of NVT.

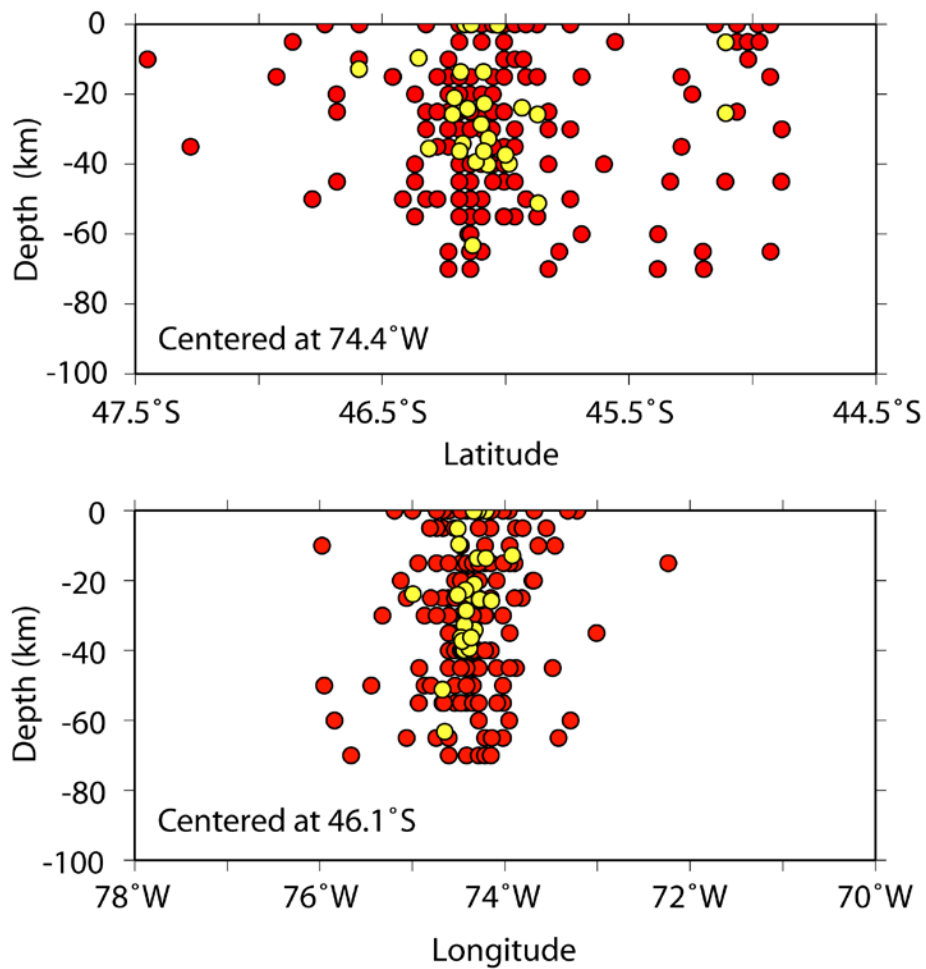


Figure 2-14. Vertical sections of NVT hypocenters. Red dots are locations of NVT with depth; yellow dots are locations of LFE. A) N-S section centered at 74.4°W. B) E-W section centered at 46.1°S.

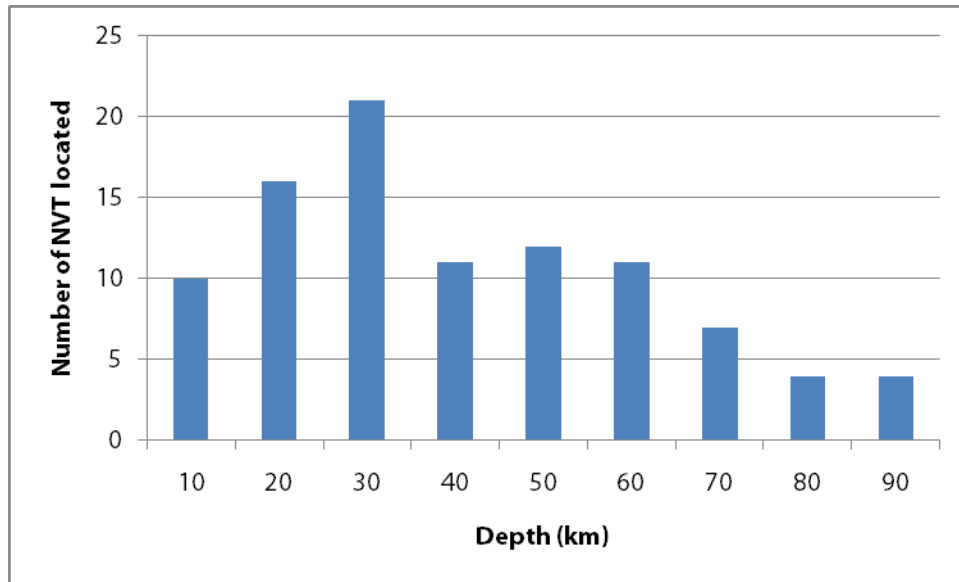


Figure 2-15. Number of NVT located with SSA as a function of depth.

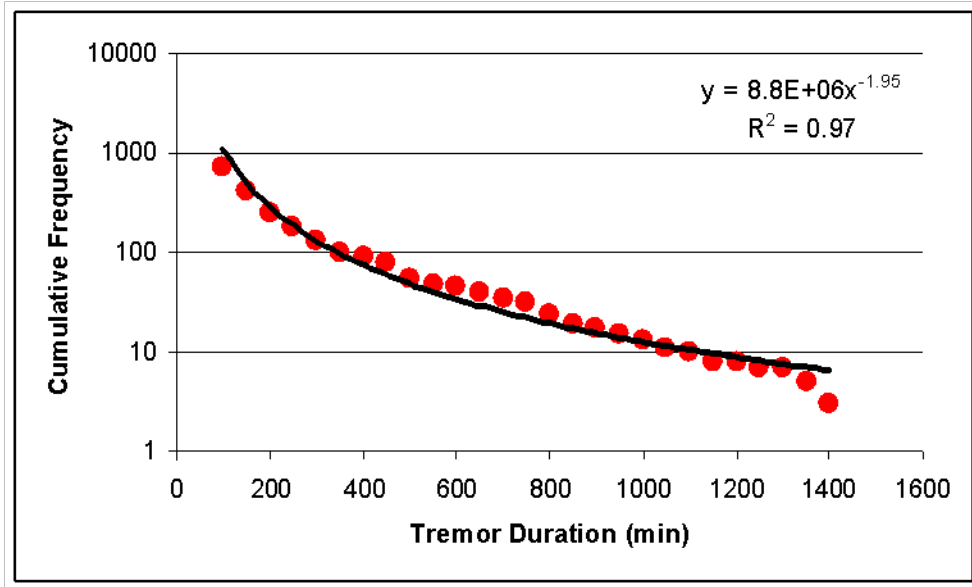


Figure 2-16. Cumulative frequency of NVT at the Chile Triple Junction. Red dots represent the number of NVT with duration equal to or greater than x-axis time. Black line represents the best fitting power-law curve to the distribution.

CHAPTER 3  
TIDAL CONSTITUENTS IN NON VOLCANIC TREMORS AT THE CHILE TRIPLE  
JUNCTION

**1.9 Introduction**

The influence of tidal gravity on seismic phenomena has been studied for many years with relative success (Heaton 1975, Tolstoy et al. 2002, Cochran et al. 2004). At the Juan de Fuca Ridge, correlation between minimum tidal ocean loading and earthquake swarms results from the reduction in confining pressure that decreases the normal stress across faults at the Ridge, facilitating the triggering of small earthquakes (Tolstoy et al. 2002). Cochran et al. (2004) decomposed calculated solid Earth tidal stresses and ocean loading into normal and shear stresses acting on the fault planes of 2027 thrust earthquakes, demonstrating a good correlation between high tides and shallow thrust earthquakes. A better correlation has been found between tides and volcanic activity. At Mayon volcano, coincidence between tides and magmatic activity results from tidal ocean loading and solid Earth tides that modify the ambient stress balance, reducing or increasing the normal internal pressure generated in volcanic vents (Jentzsch et al. 2001).

Solid Earth tides in the crust produce stress changes that can exceed 2 kPa, and, in ocean basins, water loading can change stresses by nearly 50 kPa (Heaton 1975). The high stress necessary to trigger earthquakes ( $10^2$ - $10^4$  kPa), compared with the small stresses produced by tides, results in a generally weak correlation between earthquakes and tides (Beeler and Lockner 2003). However, stress change rate is on the order of 2 kPa/h for tides but only 0.03 kPa/h for tectonic stresses, and 0.04 kPa/h for SSE with duration of several days, and Nakata et al. (2008) have shown recently that nonvolcanic tremors are probably more sensitive to stress change rate than to absolute stress change. Recently, in the Japan and Cascadia subduction zones, and at depth along the San Andreas Fault, NVT have shown a strong correlation with solid Earth tides

and, where appropriate, tidal ocean loading. Tremor amplitude (Nakata et al. 2008, Rubinstein et al. 2008, Thomas et al. 2009) and tremor occurrence (Gallego et al. 2007) is strongly modulated at diurnal (24h) and semidiurnal (12 h) tidal periods; Gallego et al. (2007) also showed a strong correlation of tremor duration and occurrence with the long period monthly solid Earth tide. These authors agree that stresses necessary to trigger tremors are much smaller than stresses involved in earthquake production, and the faults involved are very close to failure. Nakata et al. (2008) calculated the Coulomb failure stress change from the theoretical solid Earth tide and ocean tidal loading. Tidal stress was estimated in the epicenter of the tremor assuming a thrust fault mechanism. Their results demonstrate a good correlation between NVT and the rate of tidal stressing. These stresses are also on the order of the stress rate generated by SSE.

Triggering of tremors has also been observed when surface waves originating from distant earthquakes traverse areas prone to NVT. The surface waves produce a small change in the stress level necessary for fault slip (Peng and Chao 2008, Rubinstein et al. 2009), or a change in the volumetric strain, increasing the fluid flow (Miyazawa and Brodsky 2008) resulting in fault slip. These observations lend support to the idea that NVT can be triggered by small stresses such as those produced by tides and surface waves. Tidal displacements could affect tremors occurring on highly-pressured faults or slip surfaces if the displacements have the effect of unclamping the fault surfaces or enhancing shear stress along fault surfaces (Cochran et al., 2004, Shelly et al. 2006). The solid Earth tidal displacements diminish with depth (e.g., Melchior, 1983), and thus must involve differential strain. For a suite of variably oriented slip surfaces, such as might be found in either the subducting Nazca plate crust and lithosphere, or in the overriding South American forearc, this strain might be compressive, dilatational or shear.

Solid Earth tides are caused by lunar and solar gravitation, and yield sub-meter displacements near the surface of the earth (Xu and Knudsen 2000). Semidiurnal constituents produce the largest body tide contribution to distortion of the Earth, diurnal constituents the second largest, and long-period the smallest such amplitudes. In this study, two years (2005 and 2006) of NVT activity and computed time series of solid earth tides were analyzed. The spectral content of tremor time series were calculated to determine tidal constituents in tremor occurrence, and time series of three component tidal displacements were cross-correlated to recover preferential strain directions favoring tremor occurrence.

### **1.10 Methodology**

In order to determine the arrival times and durations of tremor the seismograms were visually inspected. To overcome the low SNR ratio, the signal was detrended, demeaned, highpass filtered at 5 Hz, decimated at 10 Hz, and normalized. The time-series was formed by binarizing the tremor occurrence at a 1-hour sample interval, i.e., the signal is 1 when tremor is detected and 0 when no tremor was visible (Figure 3-1). Although other studies utilized tremor signal amplitude (Rubinstein et al. 2008), we used tremor occurrence instead to make the analysis independent of the tremor intensity. Stations with the greatest activity (ISM, PLM) near the active tremor cluster in the south were used for the analysis.

Fourier spectra of the tremor time series (Figure 3-2, Figure 3-3) were calculated from the binarized signal and their amplitude were normalized. Spectrograms for stations ISM (Figure 3-4) and PLM (Figure 3-5) were calculated with a time-moving window of 720 h and a slice time of 360 h. The three components (Z, N, E) of solid Earth tidal displacement were computed using the program solid (Milbert 2007). The algorithm produced time series of the tidal displacement at 1-hour sample interval in the area of the southern tremor cluster (46.5 S, 74.5 W).

The near-surface tidal displacement in the CTJ area is thus a time-varying vector in three dimensions. We can get a sense of the orientations of the slip surfaces that produce tremors modulated by tides if we can show that the modulation depends on the direction of the tidal displacement. To estimate the maximum correlation of Chilean NVT with regional solid Earth tides, the three components of the tidal displacement vector time series were correlated (Pearson) with the tremor series at a series of different phase shifts. The calculation was repeated with both time series filtered at semidiurnal, diurnal, and long-term tidal periods.

### **1.11 Results**

Power spectra of the tremor time series (Figure 3-2) reveals strong tidal modulation of tremor occurrence at diurnal, semi diurnal, and long tidal periods. The spectra include prominent peaks at periods of 12.4 hours, 25.8 hours, 23.9 hours, 27.8 days, 16.2 days, 10.3 days, 12 hours, and 2.6 days, in order of decreasing amplitude. For comparison, the vertical amplitudes of solid Earth tidal constituents, in decreasing order, are: 12.4 hours, 23.9 hours, 12 hours, 25.8 hours, 12.7 hours, 24.1 hours, 11.9 hours, 13.7 hours, and 27.6 days (Wahr 1995) Note the excellent correspondence in periods between the two sets of time series. In general, the amplitudes of solid Earth tidal displacement coincide with the amplitudes of NVT power spectral peaks, high amplitudes for semi-diurnal tides, medium amplitudes for diurnal, and low amplitudes for long-period tides. Note three observed peaks in the tremor spectra occur at periods unrelated to tidal displacements, those at 16.2, 10.3, and 2.6 days (Figure 3-2). In detail, four diurnal tidal constituents (Figure 3-3) are present in the tremor power spectra, at 25.82, 23.93, 24.08, and 24.01 hours. This excellent correspondence between the NVT and tidal spectra has not been observed before.

Spectrograms (Figure 3-4, Figure 3-5) of tremor signals at stations PLM and ISM show

strong spectral content at semidiurnal, diurnal and long-period continuously throughout the two years of data collected. Diurnal periods appear stronger during November-February (Austral summer), and spectral gaps for the three periods appear during winter time. One month (8 Nov and 8 Dec, 2005) of the tremor time series during the period of high spectral amplitudes reveals that tremor activity increased during periods of low tidal amplitude (Figure 3-6). In other words, high tides tend to suppress tremor, and low tides enhance tremor activity.

The cross-correlation between NVT time series and computed near-surface displacement of the solid Earth tides was calculated using narrow-band filtered signals at semi-diurnal (0.08 cph), diurnal (0.04 cph) and long (0.002 cph) periods. The maximum cross-correlation value, trend, and plunge directions for semi-diurnal, diurnal and long periods are, respectively: 0.55, S66°W, 17°; 0.55, N16°W, 56°S and 0.54, N86°W, -3°. For signals filtered at periods outside the tidal band periods, the correlation coefficient decreased to 0.2, and for a random tremor signal filtered at the tidal periods yielded a correlation coefficient of just 0.02.

### **1.12 Discussion**

Spectral analysis of NVT time series reveals a strong tidal modulation of CTJ tremor occurrence. The amplitudes of tremor power spectral peaks (Figure 3-2) mimic the amplitudes of the semi-diurnal, diurnal and fortnightly tidal displacements (Table 1). Two mechanisms have been invoked to explain the production of NVT: The first entails the presence of slab dehydration fluids near the plate interface increases pore pressure, thereby decreasing the effective normal stress, and producing hydraulic fracturing (Obara 2002). The second mechanism posits that tremors occur by shear on fractures produced by long-duration series of small-magnitude LFE (Ide et al. 2007, Shelly et al. 2007, La Rocca et al. 2009). In the CTJ, the strong correlation ( $>0.55$ ) between tremor activity and tidal displacements (Table 2) in certain orientations indicates that small stresses produced by the gravitational forces of the moon and

sun can trigger tremor activity. For the first tremor production mechanism, tidal stresses could produce volumetric changes facilitating fluid flow and fracturing; for the second model, tidal stresses could activate indurated faults at high pore pressure that are already close to failure.

If we assume that the maximum correlations between tidal displacement and tremor occurrence occur because the tides unclamp existing indurated (high pore pressure) fault surfaces, or because they enhance shear stress along such faults, accelerating slip episodes, then the directions of these tidal displacement at the three periods studies (semidiurnal, diurnal, long) should indicate the orientations of the fault surface in question. At semi-diurnal periods, the maximum Pearson cross-correlation (0.55) occurs when the displacement on the Earth's surface trends S66°W and plunges shallowly at 17°. Fault surfaces perpendicular to this direction, as they must be to be unclamped by such a displacement, strike N24°W and dip 73°E. A population of faults with orientation similar to this ideal attitude exists in the CTJ region in the form of the many crustal normal faults formed in the Nazca Plate during spreading of the Chile Ridge. The Chile Ridge segment now at the trench at the CTJ in fact strikes N15°W, and we know from marine geophysical studies (Herron et al. 1981, Bangs et al. 1992) that the normal faults dip steeply. Tremors of the CTJ margin occur in Nazca lithosphere that has subducted. The effect of downthrusting beneath South America on the orientations of the Nazca crust normal faults should be to steepen the dip of the faults by around 10-15°, but should only have a slight effect on the faults' strike, tending to rotate them slightly to the northwest. A similar analysis shows that the best-correlation long period tidal displacement can unclamp faults oriented N4°E, 87°W, i.e., faults also with a very similar orientation to the subducted normal faults in the Nazca Plate. Numerous studies of the oceanic lithosphere show such ridge-formed normal faults to be pervasive, and thus tidal unclamping and slip on these faults – post

subduction – is a realistic source of tremor production.

Invocation of the other potential mechanism for linking tremors and tides, shear on existing faults enhanced by tidal displacements, involves a different geometry between the tidal displacement and the fault surface that can be affected. Shear on a plane is enhanced by motions at angles of, typically, 30-60° to the planar surface. The maximum correlation between diurnal tidal displacements and tremors occurs for tidal displacements that trend nearly E-W (N86°W) and are nearly horizontal (-3°). Planes that lie at the angles to this displacement necessary to enhance shear have poles that form cones about the maximum correlation vector. Obviously, there are an infinite number of such planes, but in reality, the likely fault surfaces that exist in the vicinity of the Nazca-South American interplate interface (i.e., where the tremors occur) include both the pervasive normal faults formed by spreading at the Chile Ridge, mentioned above, and also the transform faults that offset the Chile Ridge segments that have now subducted beneath South America. The latter includes the Taitao transform fault that lies beneath the Taitao Peninsula very close to the southern cluster of very active tremors. Depending on their post-subduction dips, both sets of faults also lie at the requisite angles to the diurnal tidal displacement vector that produces the maximum tide-tremor correlation.

Thus, existing fault and fracture populations within the subducted Nazca crust are properly oriented with respect to tidal displacements to yield tidally-triggered slip, thereby producing tremors. The stress rate of tidal forces is likely sufficient to trigger tremors on slip surface subjected to high pore fluid pressures, thus diminishing the need for large stresses (Nakata et al. 2008).

### **1.13 Conclusions**

Episodes of NVT detected at the Chile Triple Junction occur near and at the Nazca-South America interplate interface and within the overriding plate. A clear correlation between

the occurrence of NVT and soli-lunar tides was observed in the CTJ area. Tremor triggering probably occurs when fractures close to failure are activated by the small change in stresses produced by tides. The correlation between tremor occurrence and tidal displacements is a maximum when the strain caused by semi-diurnal, diurnal, and fortnightly tidal displacements unclamps or enhances shear on existing populations of faults in the Nazca plate crust.

Table 3-1. Tidal constituents of the solid earth tide, a product of lunar and solar gravitational attraction (Wahr 1995). Cph, cycles per hour.

| Period Name         | Period     | Cph     | Vert amp (mm) | Horiz amp (mm) |
|---------------------|------------|---------|---------------|----------------|
| <b>Semi-diurnal</b> |            |         |               |                |
| M2                  | 12.421 hr  | 0.08051 | 384.83        | 53.84          |
| S2                  | 12 hr      | 0.08333 | 179.05        | 25.05          |
| N2                  | 12.658 hr  | 0.079   | 73.69         | 10.31          |
| K2                  | 11.967 hr  | 0.08356 | 48.72         | 6.82           |
| <b>Diurnal</b>      |            |         |               |                |
| K1                  | 23.934 hr  | 0.04178 | 191.78        | 32.01          |
| O1                  | 25.819 hr  | 0.03873 | 158.11        | 22.05          |
| P1                  | 24.066 hr  | 0.04155 | 70.88         | 10.36          |
| Φ1                  | 23.804 hr  | 0.04201 | 3.44          | 0.43           |
| Ψ1                  | 23.869 hr  | 0.0419  | 2.72          | 0.21           |
| S1                  | 24 hr      | 0.04167 | 1.65          | 0.25           |
| <b>Long</b>         |            |         |               |                |
| Mf                  | 13.661 day | 0.00305 | 40.36         | 5.59           |
| Mm                  | 27.555 day | 0.00151 | 21.33         | 2.96           |
| Ssa                 | 0.5 yr     | 0.00023 | 18.79         | 2.6            |
| lunar               | 18.61 yr   | 0.00001 |               |                |
| Sa                  | 1 yr       | 0.00011 | 2.97          | 0.41           |

Table 3-2. Maximum cross-correlation of NVT signal and solid Earth tidal displacement. Tremor signal was band passed at diurnal, semi-diurnal and long tidal periods. A random signal was generated and filtered at the same periods.

| Filter               | Max Correlation | Lag (hr) | Dip | Direction |
|----------------------|-----------------|----------|-----|-----------|
| <b>Tremor Signal</b> |                 |          |     |           |
| No filter            | 0.25            | 0        | 127 | 270       |
| Semi-diurnal         | 0.55            | 0        | 107 | 246       |
| Diurnal              | 0.55            | 0        | 146 | 344       |
| Long                 | 0.54            | 0        | 87  | 274       |
| 0.05-0.07            | 0.22            | 2        | 95  | 330       |
| 0.01-0.03            | 0.2             | 2        | 100 | 335       |
| <b>Random Signal</b> |                 |          |     |           |
| No filter            | 0.02            | 4        | 87  | 185       |
| Semi-diurnal         | 0.1             | 5        | 110 | 330       |
| Diurnal              | 0.02            | 6        | 87  | 184       |
| 0.05-0.07            | 0.02            | 5        | 86  | 183       |
| 0.01-0.03            | 0.02            | 0        | 89  | 346       |

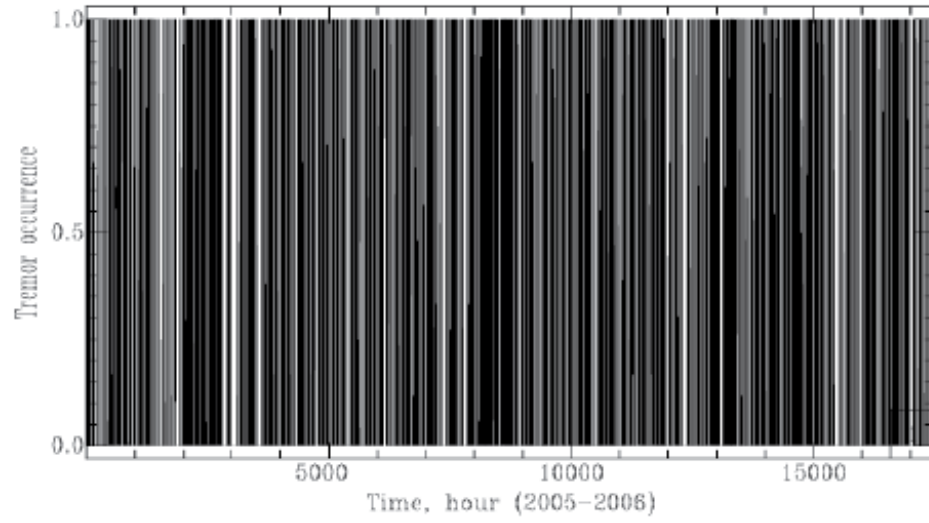


Figure 3-1. Binarized signal of tremor duration time series per hour, 1 signifies tremor present, 0 when no tremor activity for each hour.

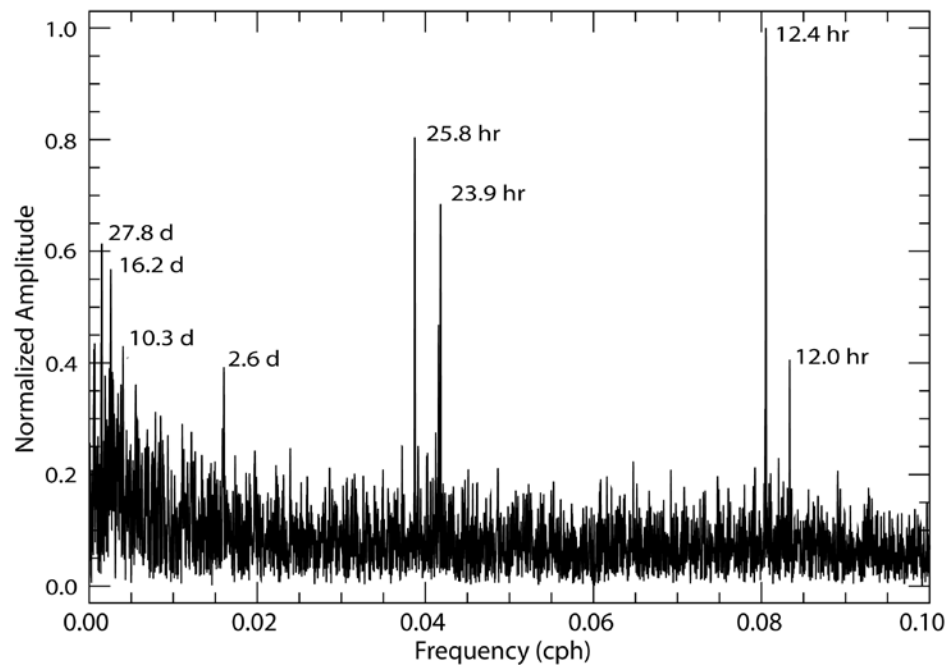


Figure 3-2. Power spectrum of binarized tremor time series. Frequency expressed in cycles per hour (cph); amplitudes have been normalized.

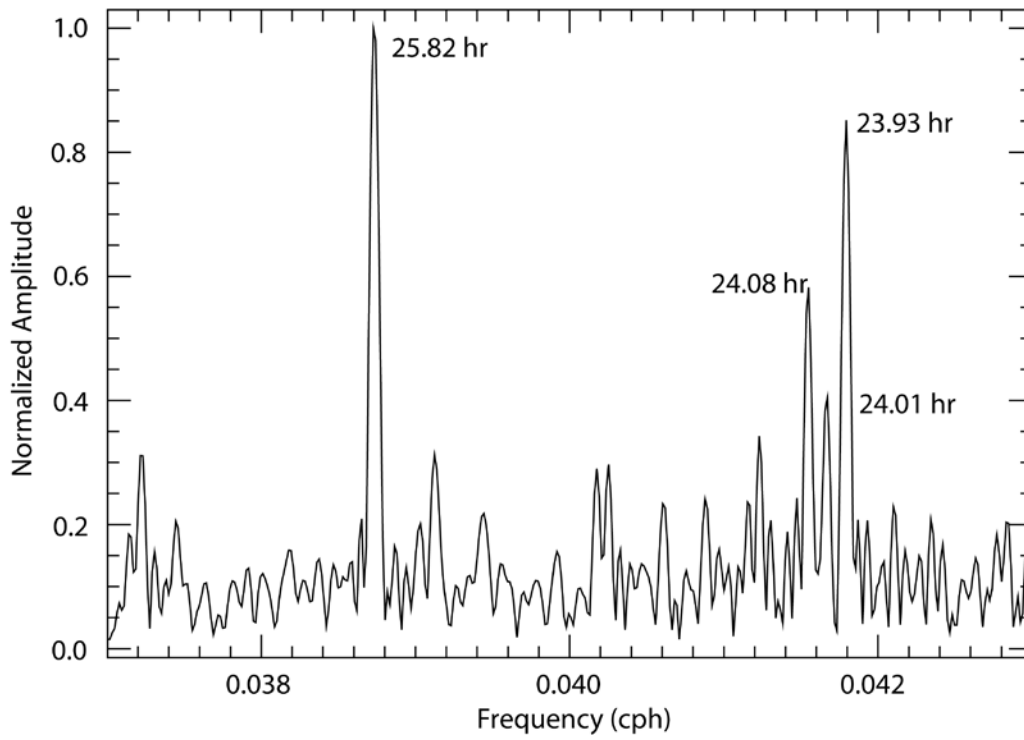


Figure 3-3. Power spectrum of binarized tremor time series for diurnal periods. Frequency expressed in cycles per hour (cph); amplitudes have been normalized.

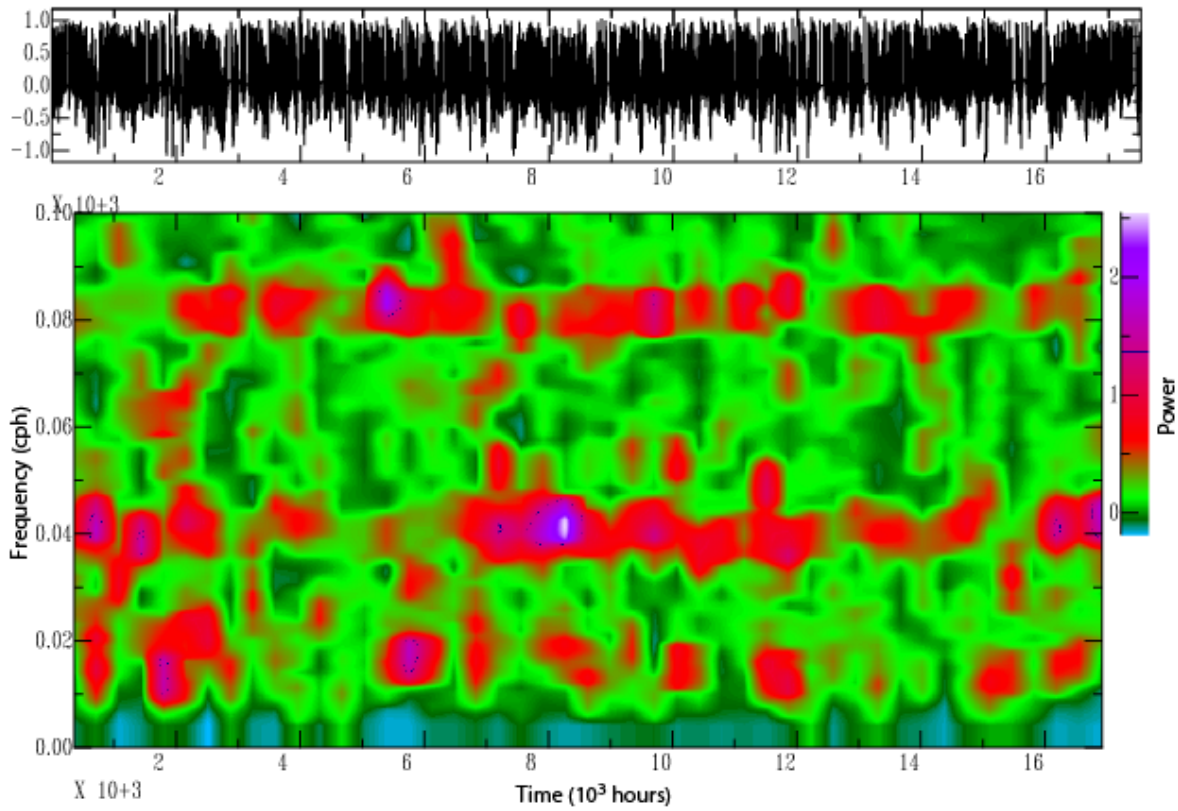


Figure 3-4. Station ISM spectrogram. Top: detrended and demeaned binarized signal for 1720 hours. Bottom: spectrogram, with frequency in cycles per hour (cph) on the vertical axis, and time in hours for two years of data (2005 and 2006) on the horizontal axis. Color scale indicates spectral power.

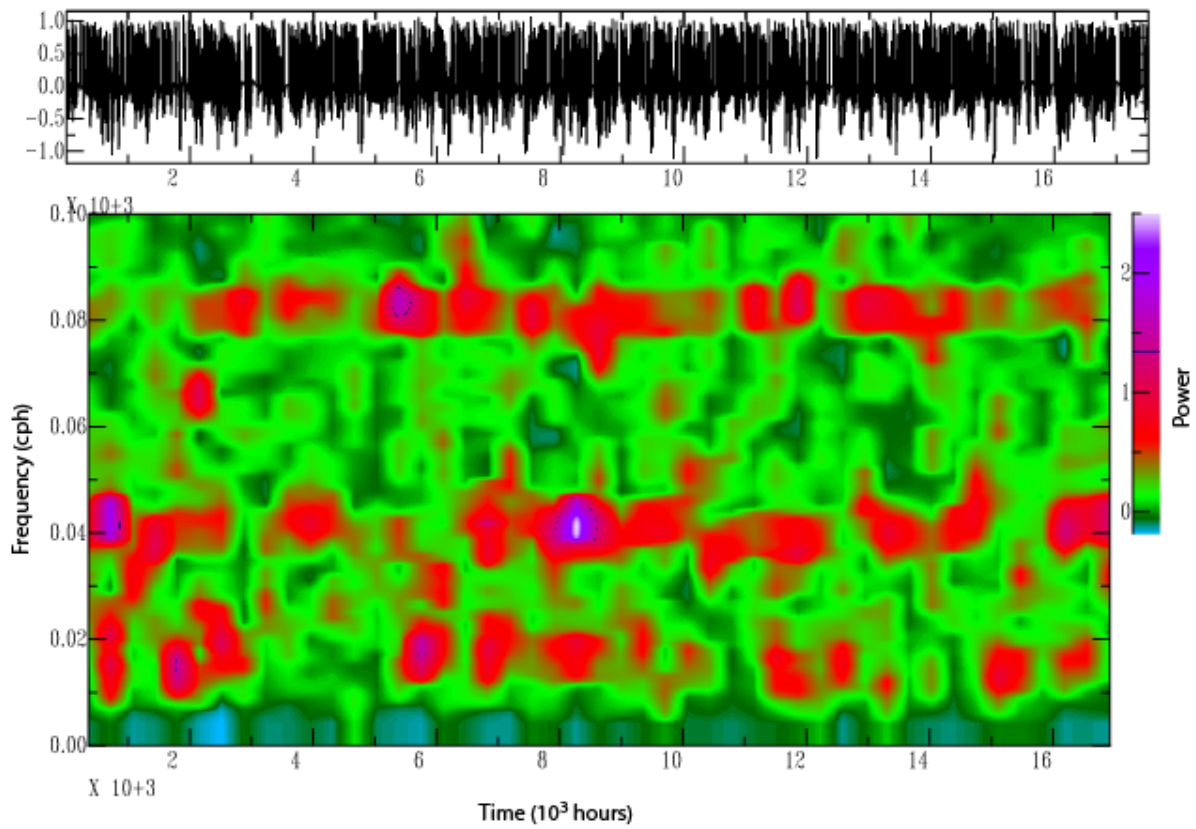


Figure 3-5. Station PLM spectrogram. Top: detrended and demeaned binarized signal for 1720 hours. Bottom: spectrogram, with frequency in cycles per hour (cph) on the vertical axis, and time in hours for two years of data (2005 and 2006) on the horizontal axis. Color scale indicates spectral power.

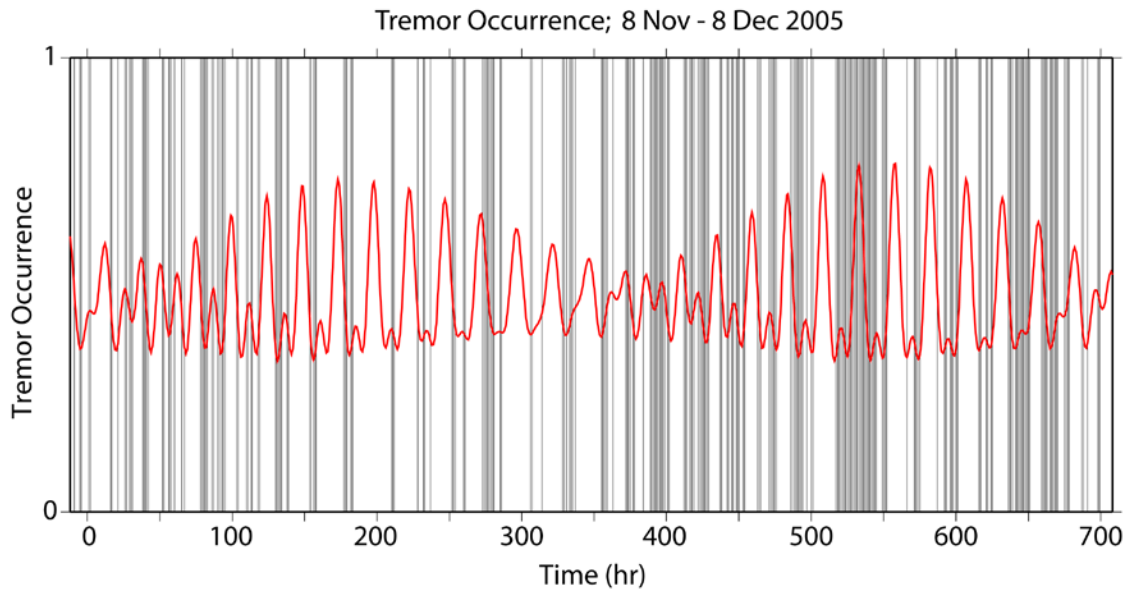


Figure 3-6. Tidal amplitude (red line) and tremor activity (dark bars) during a period of 700 hours.

## CHAPTER 4 SEISMIC NOISE TOMOGRAPHY IN THE CHILE RIDGE SUBDUCTION REGION

### 1.14 Introduction

Studies of scattered sound waves in inhomogeneous media (Lobkis and Weaver 2001, Larose et al. 2004) have found recent application in seismology in a new technique called ambient noise tomography, whereby it is possible to invert for seismic velocities of the lower and upper crust without having recourse to either passive or active seismic sources (Campillo and Paul 2003, Shapiro and Campillo 2004, Snieder 2004, Shapiro et al. 2005, Gerstoft et al. 2006, Bensen et al. 2007, Lin et al. 2007). Long period seismic noise from sources such as ocean waves generates long-period surface waves that travel in the earth's crust. At long distances, attenuation due to scattering eventually reduces the coherence of the signal and original direction of propagation. However, it is possible to enhance the signal coherence and obtain a Green's function of the surface wave propagation by cross-correlating long time series of inter-seismic noise seismograms between stations pairs (Shapiro and Campillo 2004, Snieder 2004).

In a typical tomographic inversion, propagation of seismic waves along the path between the localized source (earthquake or shot) and receiver (seismic sensor) yields the travel time of the seismic waves from origin to terminus. In this new method, seismic noise signals received simultaneously at two sensors placed at regional distances are cross-correlated to obtain the ballistic wave field response (Green's function) at one station due to an impulse source at the other (Lobkis and Weaver 2001, Snieder 2004). The ballistic wave Green's function includes travel time information for propagation in either direction between the two receivers, a phenomenon called time reversal. Thus, the impulse response can be recovered from either causal ( $t > 0$ ) or acausal ( $t < 0$ ) propagation (Larose et al. 2004). Correlation of

scattered waves yields the Green's function when the waves scattered from points near the interstation path interfere constructively; in this scenario, time reversal is equivalent to propagation of scattered energy in either direction along the interstation path (Snieder 2004).

In the ideal situation where seismic noise sources or scatterers are uniformly distributed between two stations, the cross-correlated noise signal will be a symmetric function with respect to the arrival time. However, when the noise source is concentrated along one azimuth, the cross-correlation will be one sided (Gerstoft et al. 2006). Because longer period scattered waves correspond to propagation at deeper levels, different frequency bands can be used to resolve velocity models at specific depth ranges (Gerstoft et al. 2006, Bensen et al. 2007, Lin et al. 2007).

### **1.15 Data**

In this study, we used ambient seismic noise data obtained from 44 broad band sensors (Figure 1-7) deployed between December 2004 and February 2007 in the CTJ region. Unlike other parts of the Andes, seismic activity near the CTJ is rare, with an almost complete absence of events larger than magnitude 4 (Figure 1-6). Thus, the study area is a nearly ideal place for tomography derived from ambient seismic noise. The area is very remote and sparsely inhabited, so cultural noise is also virtually non-existent. The analyzed signal is the continuous broadband vertical component seismic data recorded at 50 samples/second at the CRSP stations during the period from December 2004 to January 2007. For each station pair, a minimum of 30 days and a maximum of one year (2006) of continuous data was used. Because some of the CRSP stations did not operate during the entire deployment, only 38 station pairs met the requirement of more than 30 days of simultaneous recording. This limitation yielded 703 ( $38 \times 37/2 = 703$ ) interstation paths traversing an area approximately of 400 x 700 km, including the CTJ forearc, arc, and back-arc regions.

## 1.16 Methodology

### 1.16.1 Cross-Correlation of Noise

All signals were band-pass filtered at periods of 2.5–100 sec, downsampled to 0.5 sec, detrended, and demeaned. Then the signal was single-bit binarized, retaining just the sign of the signal amplitude (+1 for positive, -1 for negative). This truncation is effective in reducing the influence of any local earthquakes or non coherent noise included in the time window that could potentially modulate the interstation cross-correlation (Campillo and Paul 2003, Bensen et al. 2007).

24 hours of data for each station pair were cross-correlated independently and then stacked day by day into one time series that represents the Green's function dominated by Rayleigh wave energy for the given station pair. The time series were bandpass filtered at 5-10, 10-20, and 20-30 sec and normalized by the maximum amplitude, and the maximum amplitude of the envelope calculated, yielding the group velocity waveform of the scattered Rayleigh wave traveling from one station to the other. The cross correlation thus also yields the interstation travel time of forward and (in some cases) reverse propagating surface waves, as discussed above.

Two time series for stations HOP and HUD, located to the west and in the center, respectively, of the CRSP network, illustrate the cross-correlation technique. Station HOP (Figure 4-1) was located at the western extreme of the network on the Taitao Peninsula. Its cross-correlated signals with all other stations each show a strong causal, forward-propagating wave, indicating ocean waves were the principal source of the long period noise generating the interstation Rayleigh waves. For each of these interstation cross-correlograms, the amplitude of the anticausal back-propagating wave is very small and difficult to observe, but, when visible, symmetric in time with the forward propagating scattered wave. The highest peak amplitude,

also shows an increase in the lag time as a function of the station pair distance. Cross-correlograms for station HUD (Figure 4-2), located at the center of the network, show causal correlations along paths to stations located to its east, and also to those lying to its west, and the anticausal, back-propagating scattered waves are small but symmetric. The spectra (Figure 4-3) of the cross-correlated signals show peaks between 7 to 10 sec, due to the influence of ocean noise on the resulting Green's function, and white noise was added to the data to flatten the spectra.

To quantify the effect of our sensor distribution in the results (Figure 4-4), the number of station-pairs as a function of azimuth was plotted for distances between 0-100, 100-200, 200-300 and 400-500 km. Most of the paths trend north-south, but this trend is more prevalent for short paths (< 300 km). Longer paths tend to yield a wave velocity that is an average of the crustal heterogeneity, whereas short paths yield more variable velocities because averaging of structures is less along shorter paths.

The interstation velocities, determined from the interstation distances and travel times (Figure 4-5a,b), converge to the average crustal velocity as distance increases, as expected, but are more scattered for short distances. There is also a bias toward high velocities for short paths, relative to velocities less than the average, which cannot be explained by the station distribution. In part, these highly dispersed values result from low SNR (Figure 4-5e,f) for long wave periods (20-30 sec) which are not well developed in short station path and short wave periods (5-10 sec) attenuated at long distances.

The interstation velocities (Figure 4-5c,d), vary more for paths trending north-south than for other azimuths. The main source of seismic noise in this region is ocean waves along the N-S trending coast, which produces larger amplitude scattered waves along paths trending

E-W than N-S. Correlations are thus stronger for E-W trending interstation paths. As shown below, once signal-to-noise ratio is taken into account, this velocity variability with path azimuth is minimized.

### **1.16.2 Signal to Noise Ratio, SNR**

The quality of the signal was estimated for the three period bands via a signal-to-noise ratio (SNR), defined as the ratio between the maximum amplitude of a 50 sec window centered at the time of the main scattered arrival, and the standard deviation of a 50 sec window centered 475 sec before the arrival time (i.e., true noise only). The SNR was calculated for both the causal and acausal sides of the time series. Plots of SNR versus velocity (Figure 4-5e,f) show that calculated interstation velocities are more variable for low SNR ratio ( $< 6$ ) signals, which result predominantly for long period (20-30 sec) correlations. Signal quality is highest for shorter periods (5-10 sec). With respect to interstation path azimuth, SNR (Figure 4-5g,h) is high for stations pairs trending east-west. SNR is high for paths trending W ( $270^\circ$  in Figure 4-5g) and E ( $90^\circ$  in Figure 4-5h), depending on which station of the cross correlation pair is nearer the coast.

In order to minimize the effects of low SNR cross correlations in the travel time inversion, station pairs with SNR values larger than 6 were selected, considering the maximum SNR from either the positive or negative lag (causal or acausal). The interstation distance was required to be greater than 1.5 times the wavelength ( $\lambda$ ) of the highest cut-off period ( $\tau = 10, 20$  and  $30$  sec), and, assuming a phase velocity,  $c$ , of 4 km/s (Bensen et al. 2007), the minimum path lengths are 60 km for the 5-10 sec band, 120 km for 10-20 sec waves, and 180 km for 20-30 sec waves. The velocities of the interstation pairs retained after discarding the low SNR correlations (Figure 4-6) are considerably smoother with respect to path azimuth. However, a systematic variation of crustal velocity with path azimuth is visible in Figure 4-6: the highest

velocity paths trend N-S (around 0° and 180° azimuth) for the longest period waves (blue). This variation is a consequence of the sensor distribution (Figure 4-4) and possibly also azimuthal anisotropy in the crust (Murdie and Russo 1999). Of the 703 potential interstation paths, 640 5-10 sec wave paths were retained with an average velocity of 3.0 km/sec and a variance of 0.02, 454 10-20 sec wave paths with mean velocity of 3.1 km/sec and a variance of 0.01, and 200 20-30 sec wave paths with mean velocity and variance of 3.2 km/s and 0.05. Note that the longer period waves are more sensitive to higher seismic velocities of the deeper crust.

### 1.16.3 Dispersion and Rayleigh Wave Group Velocities

A frequency-time dispersion analysis (FTAN) was included to estimate group velocity as a function of period (Levshin et al. 1992) and the sensitivity of the period wave to the depth. First, the cross-correlated signal was transformed to the frequency domain, and the spectrum was flattened and normalized by weighting the complex signal by the smooth amplitude spectrum. Then, the analytical signal that discard the negative frequencies with no loss of information was calculated (Bensen et al. 2007).

$$S_a = s(\omega)(1 + \text{sgn}(\omega)) \quad \text{sgn} = \begin{cases} j & \omega > 0 \\ -j & \omega < 0 \end{cases} \quad (4-1)$$

For each station-pair waveform, the signal was filtered in a narrow band using a Gaussian filter.

$$F(\omega - \omega_i) = \exp \left[ -\alpha_i \left( \frac{\omega - \omega_i}{\omega_i} \right)^2 \right] \quad i = 1, \dots, N \quad (4-2)$$

Where  $\omega_i$  is the central frequency for periods between 5 and 30 sec with intervals of 1 sec, and  $\alpha$  is the relative width of the filter, which is distance dependent. The dispersed signal is constructed by weighting the analytical signal with the gaussian filter:

$$Sa = s(\omega)(1 + \text{sgn}(\omega))F(\omega - \omega_i) \quad (4-3)$$

The resulting waveform was transformed to the time domain and the logarithm of the symmetric signal calculated, averaging the positive and negative lagged signals, thereby yielding a matrix with period and group velocity arrival time. Values between grid points were calculated using a spline interpolation were calculated.

The dispersion curve (Figure 4-7) was obtained from the local maxima for each period. To eliminate spectral holes in the dispersion curves, the local maximum was calculated in a time window of 30 sec centered around the maximum of the previous period. Curves with large velocity jumps and gaps were disregarded, yielding a total of 407 dispersion curves (Figure 4-8). The averaged group velocity of the dispersion curve for each period was used to estimate a 1D velocity model (Figure 4-9), with an iterative weighted inversion method (Herrmann and Ammon 2002). The initial model was constructed with eleven 5 km thick layers, each with constant  $V_s = 3.5$  km/s,  $V_p = 6$  km/s, and density = 2.5 kg/m<sup>3</sup>. The sensitivity of the wave period with respect to the crustal depth (Figure 4-10) was estimated using the derivative of the calculated model with respect to the initial model.

#### **1.16.4 2-D Travel Time Inversion**

A 2D travel time inversion was performed using the least-squares method (Tarantola 2005). The area was parameterized as cells of 30 x 30 km. Wave propagation paths were assumed to be straight lines, given the small effect of earth curvature at these propagation distances. The forward velocity model was estimated by inverting the linear model,  $d=Gm$ , where  $G$  contains the lengths of segments formed by the intersections of ray paths and the cell boundaries,  $m$  is the matrix of slownesses of each cell block, and  $d$  is the inter-station travel time, obtained from the cross-correlation of stations pairs. The new model is obtained by solving the inverse problem:

$$m = m_{prior} + C_M G^t (G C_M G^t + C_D)^{-1} (d - G m_{prior}) \quad (4-4)$$

where  $G^t$  is the transpose of  $G$ ,  $m_{prior}$  is the a priori velocity model, assumed constant with values of 3.0 km/s for the 5-10 sec period correlograms, and 3.1 km/s for those of the 10-20 sec period signals.  $C_D$  is a diagonal matrix of travel time errors (assumed to be 2 sec), and  $C_M$  is the covariance matrix, derived from the exponential covariance function:

$$C(x, x') \sigma^2 \exp\left(\frac{-\|x - x'\|^2}{L}\right) \quad (4-5)$$

where  $\sigma$  is the variance of the velocity,  $(x-x')$  is the distance between cells and  $L$  is the smoothness, assumed to be 20 km, of the variation between contiguous cells. For large distances, the covariance tends to zero. The resolution matrix is:

$$R = (G^t C_D^{-1} G + C_M^{-1}) \quad (4-6)$$

Thus two 2D models were produced for the selected cross-correlated waveforms at 5-10 and 10-20 sec period. 640 ray paths were used for the 5-10 sec inversion (Figure 4-11), and 454 paths for 10-20 sec model (Figure 4-12). Ray density is higher at the center of the network, which is evident in the maps of inversion resolution (Figure 4-13, Figure 4-14). Resolution falls below the acceptable threshold only near the edges of the CRSP network. The velocity model for 5-10 sec band (Figure 4-15 & Figure 4-9) corresponds to the shallow crust above 10 km, and that derived from the 10-20 sec band is representative of crustal structure between 10 to 20 km depth (Figure 4-16 and Figure 4-9).

### 1.16.5 3-D Travel Time Inversion

A 3D velocity (Figure 4-17) model was also determined using the 407 dispersion curves derived from the group velocity analysis (Figure 4-8). For each period band between 5 and 20 sec, we inverted the travel times, obtaining 25 velocity models. For each cell we inverted

the 25 group velocities (Herrmann and Ammon 2002) using the initial model of eleven layers with layer thicknesses of 5 km,  $V_s = 3.5$  km/s,  $V_p = 6.0$  km/s and density =  $2.5$  g/cm<sup>3</sup>, obtaining a 3D model of the velocity perturbation respect to the initial model.

### **1.17 Results**

Rayleigh wave group velocities for 5-10 sec and 10-20 sec period bands are shown in Figure 4-15 and Figure 4-14, respectively. S wave velocities from the surface wave dispersion analysis are shown in Figure 4-17, and the 1-D S wave crustal model for the study area is shown in Figure 4-9. The 1D crustal model (Figure 4-9) shows a velocity increase from 3.2 km/s to 3.6 km/s between 0 and 20 km depth, and a deeper increment of velocity from 3.6 km/s to 3.9 km/s could indicate a Moho depth of 30-40 km, but resolution deeper than 30 km is poor (Figure 4-10).

#### **1.17.1 5-10 Second Period Inversion**

The principal features visible in the map of group velocities derived from the 5-10 sec period (Figure 4-15) signals are an elongated low velocity (2.8-3.0 km/s) anomaly approximately between the two branches of the Liquiñe-Ofqui fault zone between 44.5-45.5°S; patches of low (2-6-2.8 km/s) velocity at the NE edge of the Golfo de Penas and extending to the east; and also along the Chile-Argentina border between 45-47°S, along the eastern edge of the study region. Shallow crustal velocities in the western Chonos Islands and Taitao Peninsula are generally low, but the eastern part of this area is marked by higher velocity anomalies (3.0-3.2 km/s). More restricted regions of relatively high velocity (3.2-3.6 km/s) occur in three small areas near the center-north of the map, and near the southeastern boundary of the region of resolved velocities. In general, the region lying 100-150 km to the east of the Liquiñe-Ofqui fault zone is characterized by relatively high velocities of 3.1-3.3 km/s.

### **1.17.2 10-20 Second Period Inversion**

Figure 4-16 shows the results for group velocities determined from the 10-20 s period signals. The overall pattern of velocity anomalies is similar to those visible in Figure 4-15, although the range of velocities is more restricted (2.8-3.3 km/s), and the scale of the anomalies appears to be smaller. Two high velocity anomalies (3.1-3.3 km/s) lie parallel to the Lower Cretaceous North Patagonian Batholith, and a low velocity (3.0 km/s) anomaly occurs where the volcanic arc is present. The Taitao Peninsula is also marked by low velocity (<2.9 km/s). Note the persistence of a high velocity (3.1-3.2 km/s) anomaly at the south eastern edge of the study area, and a low velocities (2.9-3.1 km/s) along the Chile-Argentina border between 45-47°S.

### **1.17.3 3-D Group Velocity Inversion**

The 3D model (Figure 4-17) obtained from the dispersion analysis is in a good agreement with the two 2D models. A high velocity anomaly is present between 2.5 and 20 km depth along the LPBC, and patches of lower velocity anomalies follow the volcanic arc and the Liquiñe-Ofqui fault. The low velocities along the eastern edge of the study area fade with depth. The extended low velocity at the Taitao Peninsula is present between 2.5 and 7.5 km, and low velocities anomalies beneath the Golfo de Penas also fade out at deeper levels.

## **1.18 Discussion**

Relative to other studies using the ambient seismic noise tomography technique, the Rayleigh wave group velocity anomalies obtained are somewhat high. For example, Shapiro et al. (2005) show velocities for 7.5 sec period Rayleigh waves in southern California that range from 1.4-4.0 km/s, with a definite preponderance of regional velocity anomalies at the low end of their scale (see their Fig. 2). Likewise, Lin et al. (2007) show Rayleigh wave group velocities ranging from 1.8-3.2 km/s for 8 and 13 sec period waves recorded in New Zealand.

In part, such differences may be due to differences in the analysis and inversion methods. However, we note that the geology of our study area - dominated by the glacially-stripped basement of Patagonian Batholiths at the surface - is distinctive and clearly lacks the extensive, deep sedimentary basins found in southern California and New Zealand. Also, Shapiro et al. (2005) found group velocities in the Sierra Nevada Batholith that are as high or higher than the values founded in this study for the LCPB (3.1-3.3 km/s).

The Rayleigh wave velocities obtained from travel time inversions of ambient noise cross-correlations and dispersion analysis correspond closely to known geologic features (Figure 1-3). The inversion of the 5-10 s period Green's functions (Figure 4-15) is more sensitive to shallow structure no deeper than 10 km (Figure 4-10), and should therefore correlate most closely with superficial geology. An elongated, north-south trending low velocity anomaly that coincides with the MPB and the Southern Volcanic Zone eruptive centers is observed north of the CTJ. This low velocity anomaly is also bounded by the two main strands of the Liquiñe-Ofqui fault zone. Velocities  $\sim 2.7$ - $2.8$  km/s, although not very low with respect to results from similar studies elsewhere (e.g., (Lin et al. 2007)), are noticeably low for the CRSP study region. The depth of magma chambers beneath the five arc volcanoes is uncertain, but hypocenters of earthquakes that occurred during the last eruption of Hudson volcano in 1991 were clustered between 2-20 km depth (Naranjo et al. 1993). High velocities west and east of the LOFZ correlate well with the exposures of the NPB in the eastern Chonos Islands/Taitao Peninsula and east of the LOFZ. The high velocity anomaly at the southeastern corner of the study area corresponds to the metamorphic units of the Devonian-Carboniferous EMC exposed at high elevations around Monte San Lorenzo (3,700 m).

The notable low velocity anomaly at the NE edge of the Golfo de Penas is probably

due to the one sedimentary basin extant in the study area, as this area is clearly the site of much recent glacial sediment fill brought to the Golfo by the rivers draining Campo de Hielo Norte, the northern Patagonian ice field; the extension of this anomaly to the east correlates with the presence of the ice field. The low velocity regions near the Chile-Argentina border in the NE part of the study area correlate with the Jurassic-Cretaceous units of the Patagonian Ranges.

The inversion of the 10-20 second period signals (Figure 4-16) is sensitive to depths between 10-20 km (Figure 4-10). The observed velocity variations for this inversion are less pronounced than those of the shorter periods, perhaps indicating a more homogeneous crust at these depths, or, alternatively, greater smoothing of velocity heterogeneities due to longer sampling period. The high velocity anomaly in the southeastern portion of the study region, also observed in the shallower crustal velocity model, persists at these greater depths, indicating that the high velocity units of the EMC outcropping at the surface in the vicinity of Monte San Lorenzo extend throughout the upper crust (Thomson and Herve 2002).

Two high velocity anomalies (3.1-3.4 km/s) at the east and west of the volcanic arc correlate with the LCPB, indicating the presence of the batholith at depth. Lower velocity between these two features correlates with the location of the volcanic arc. The low velocity anomaly (2.7-2.9 km/s) at the Taitao Peninsula is likely a result of elevated temperatures (manifested as active hydrothermal springs and recent volcanism) due to the subduction of an actively spreading segment of the Chile Ridge (Lagrabielle et al. 2000).

### **1.19 Conclusions**

Interstations time-domain Green's function were estimated from cross-correlation of ambient seismic noise recorded in the Chile Triple Junction region, the resulting interstation travel times were inverted to obtain a crustal shear wave velocity model. The results show that observed crustal seismic velocities correlate well with known geologic features. High crustal

velocities are where the North Patagonian Batholith outcrops or is likely present at depth, and relatively low velocities correlate with the active volcanic arc of the Southern Volcanic Zone and the Liquiñe-Ofqui intra-arc shear zone, the recent Chile Ridge subduction beneath the Taitao Peninsula, and a sedimentary sequence due to glacial sediment outflow into the NE Golfo de Penas. A pronounced high velocity anomaly in the southeastern portion of the study area correlates with high-elevation outcrops of highly compacted metamorphic rocks of the Paleozoic Eastern Metamorphic Complex

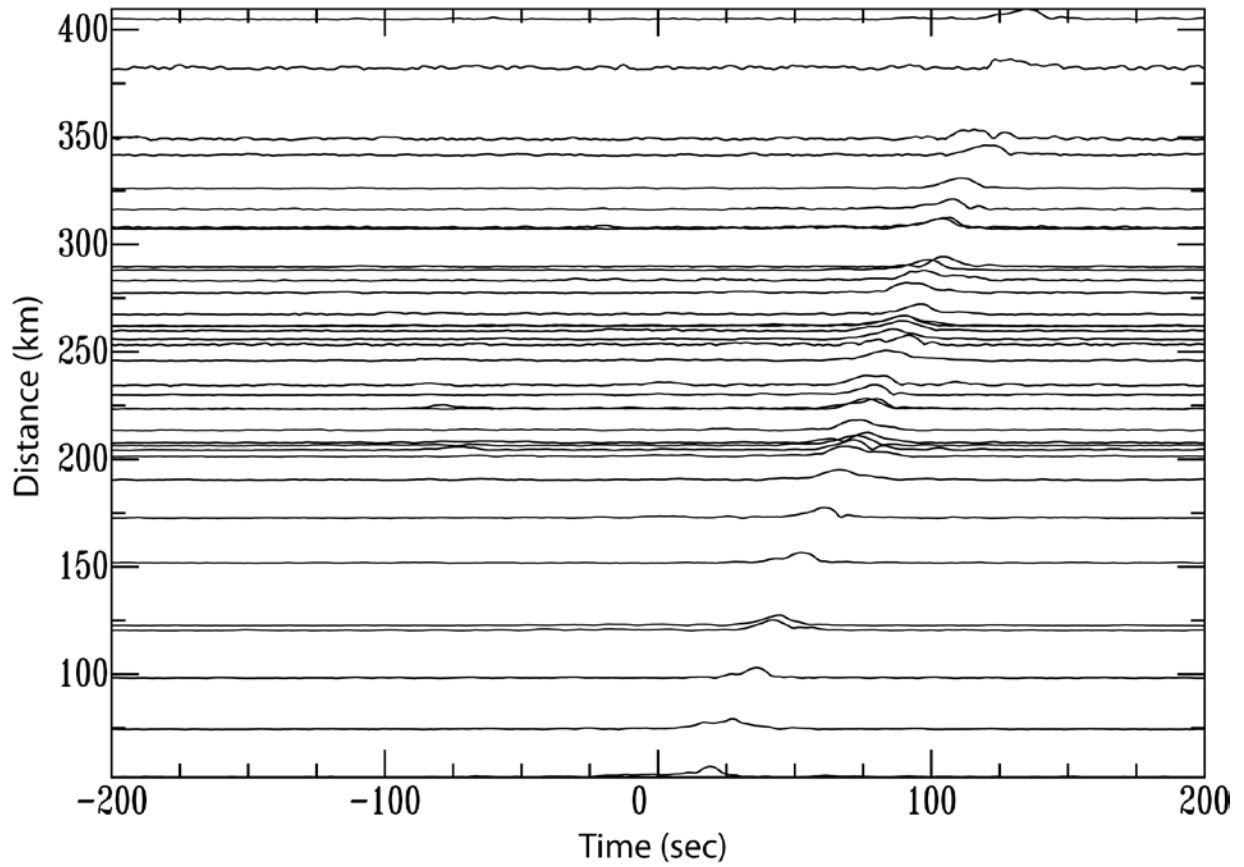


Figure 4-1. Time series of cross-correlation for station HOP01, located at the extreme west of the study area, near the coast, and other CRSP stations. Signal was band-pass filtered at 2.5-10 sec

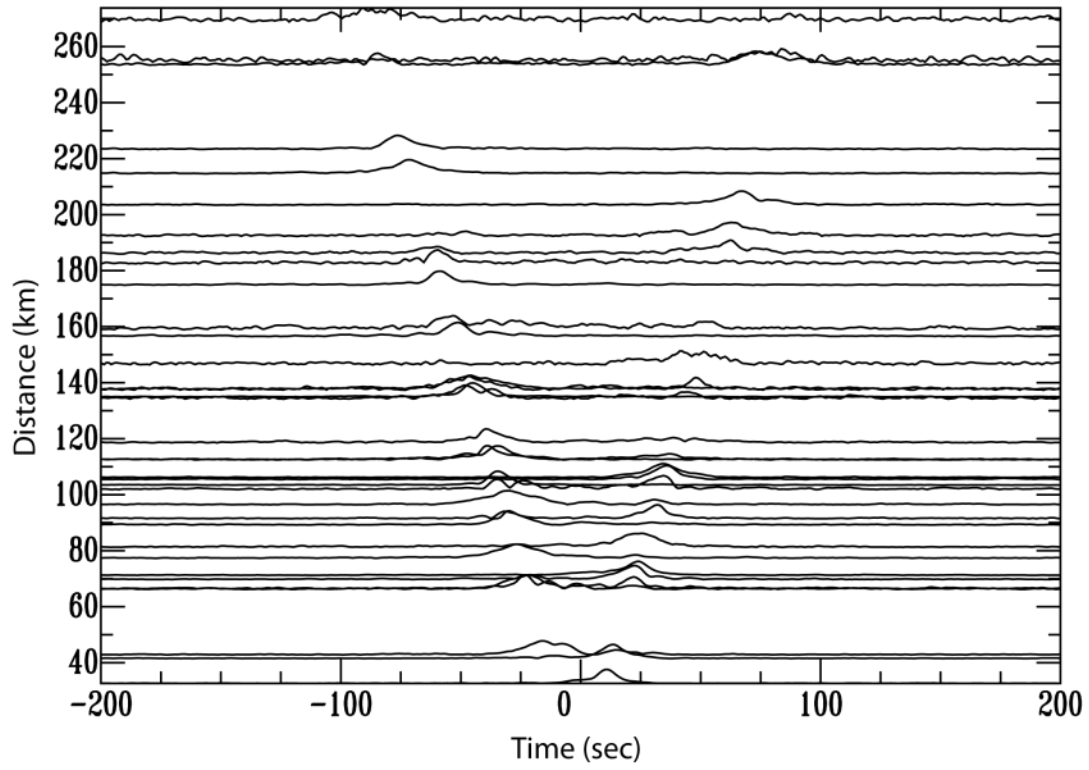


Figure 4-2. Time series of cross-correlation for station HUD01, located approximately at the center of the CRSP network. Signal was band-pass filtered at 2.5-10 sec.

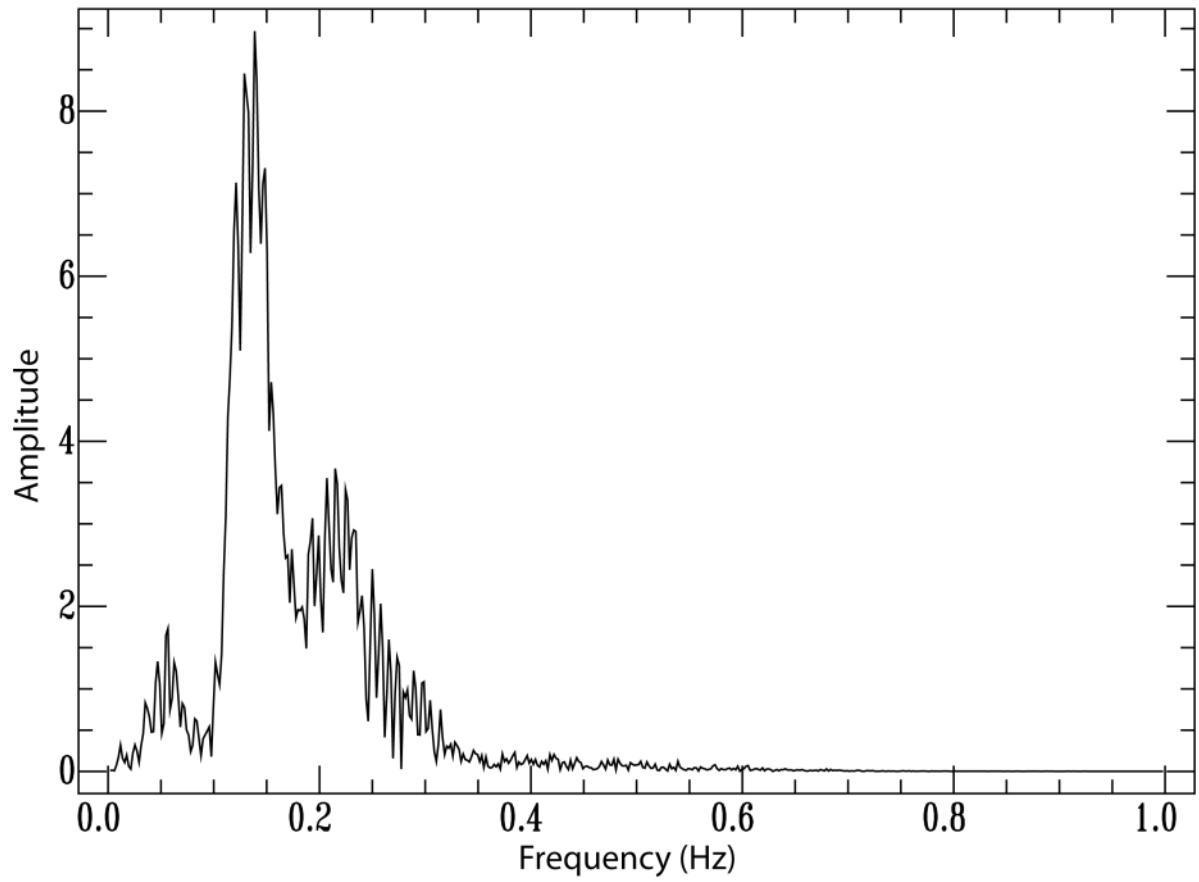


Figure 4-3. Frequency analysis of cross-correlated waveform between station PLM and IBJ

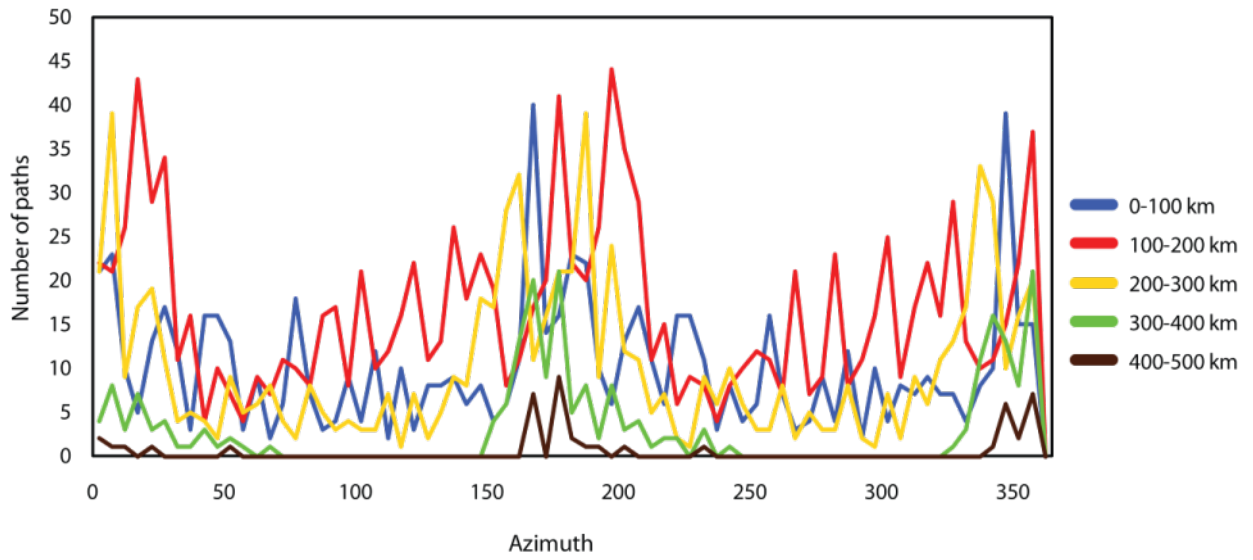


Figure 4-4. Azimuthal distribution of stations path, for distance range between 0-100, 100-200, 200-300, 300-400, 400-500 km.

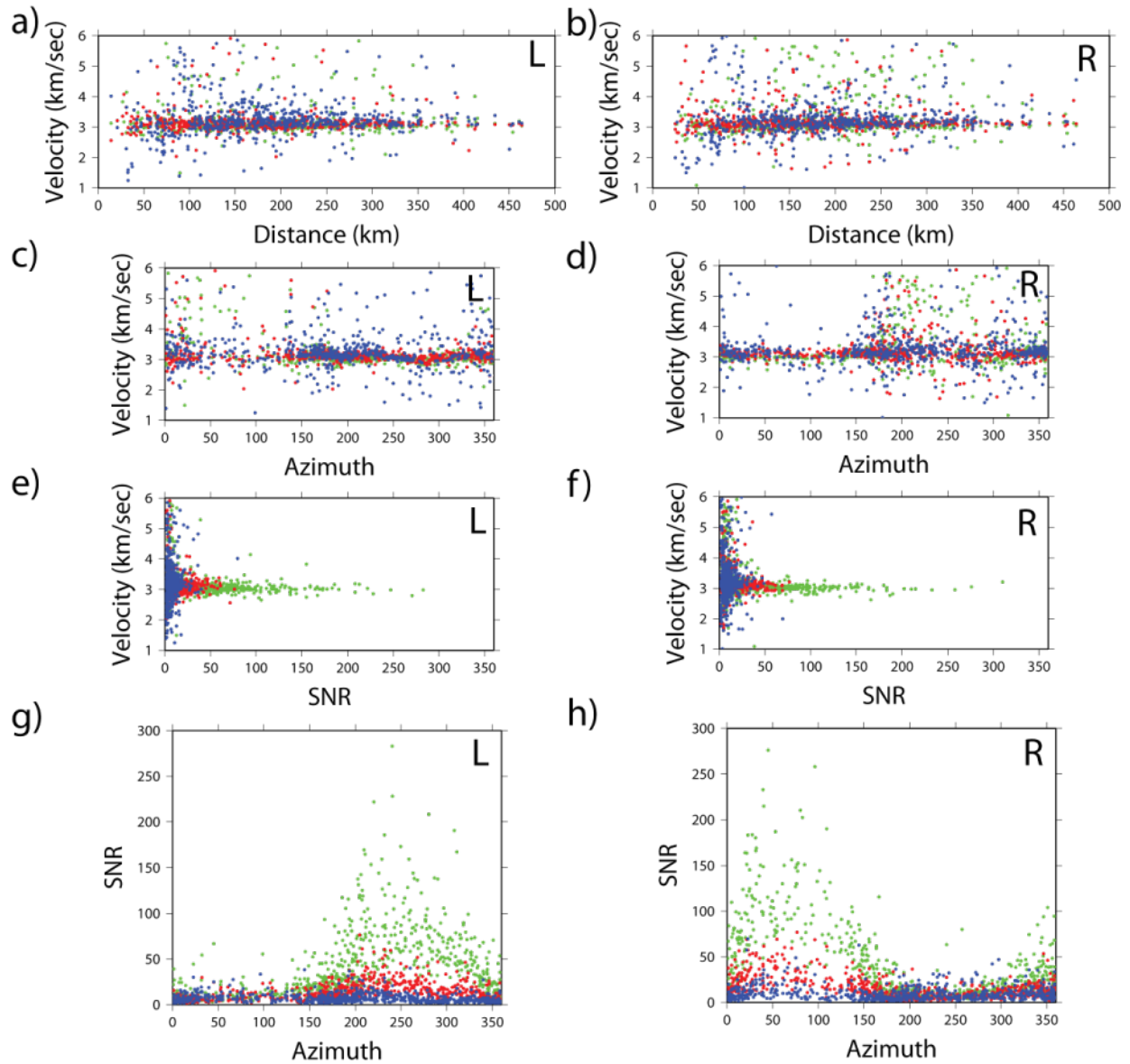


Figure 4-5. Data analysis for Right and Left side of the cross-correlation for three period bands. Green dots (5-10 sec), red dots (10-20 sec) and blue dots (20-30 sec). a-b. Average velocity for station pairs as a function of distance. c-d. Average velocity for station pairs as a function of azimuth. e-f. Average velocity as a function of SNR. g-h. SNR as a function of azimuth.

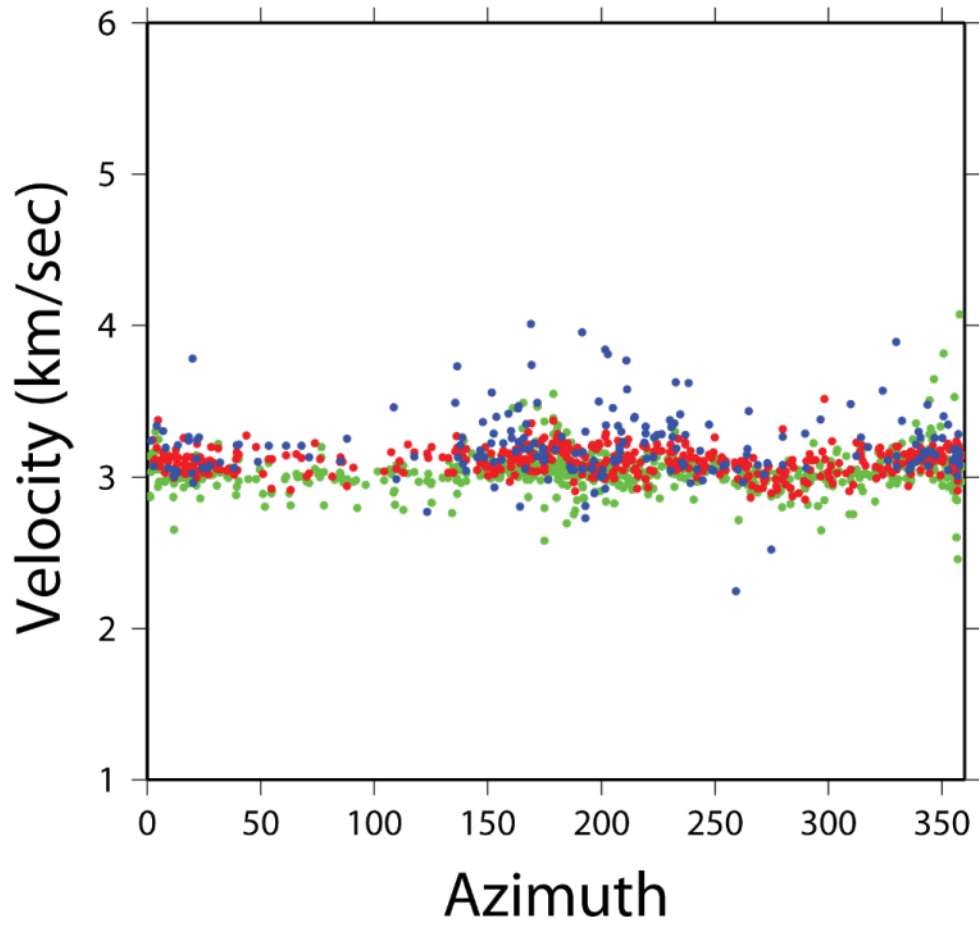


Figure 4-6. Selected velocities for station pairs with SNR > 6 and distance large than 1.5 the wavelength of the filter.

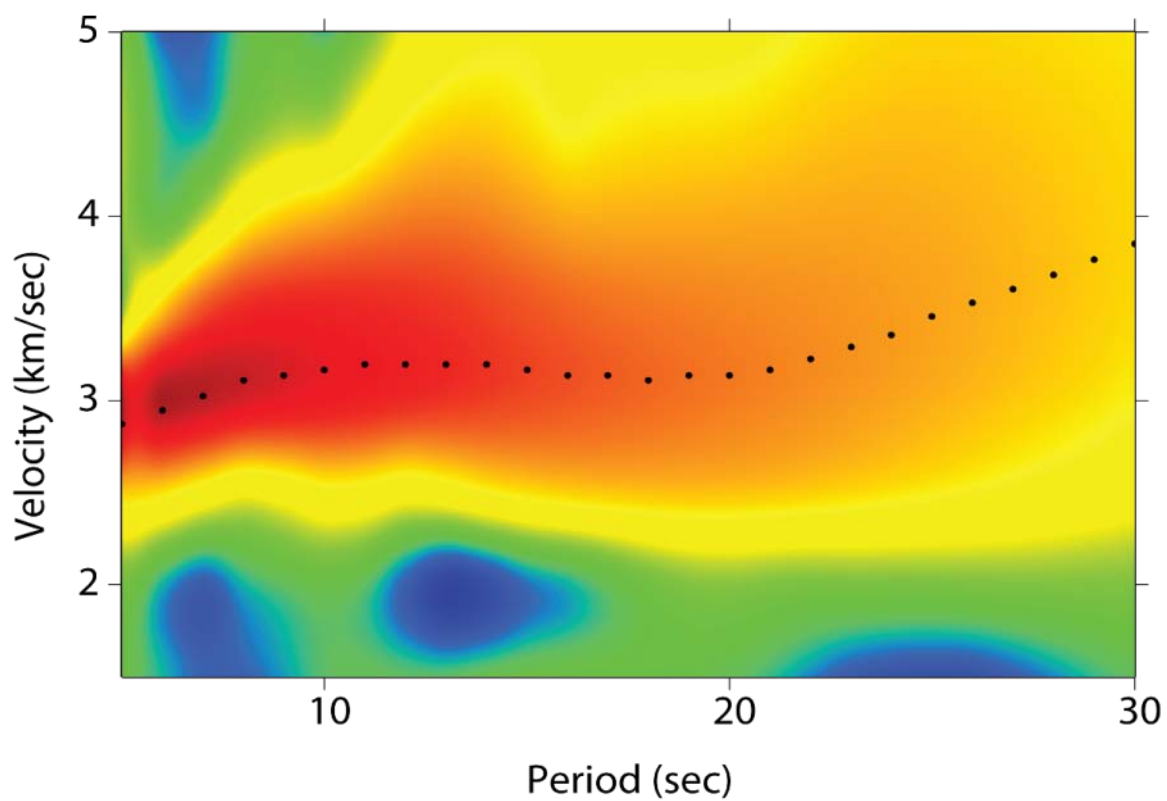


Figure 4-7. FTAN analysis for IBJ-PLM station pair, red colors indicate high amplitude of the cross-correlation after the Gaussian filter. Black dots indicate the highest amplitude for each period band.

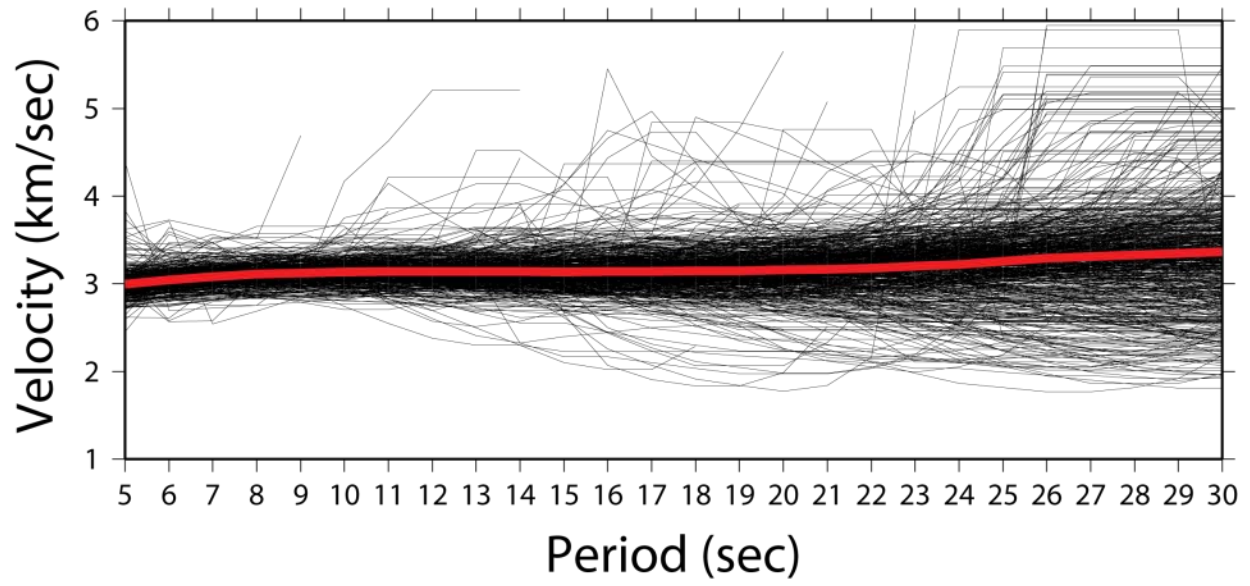


Figure 4-8. 407 curves dispersion curves (back) and the averaged group velocity at each period (red)

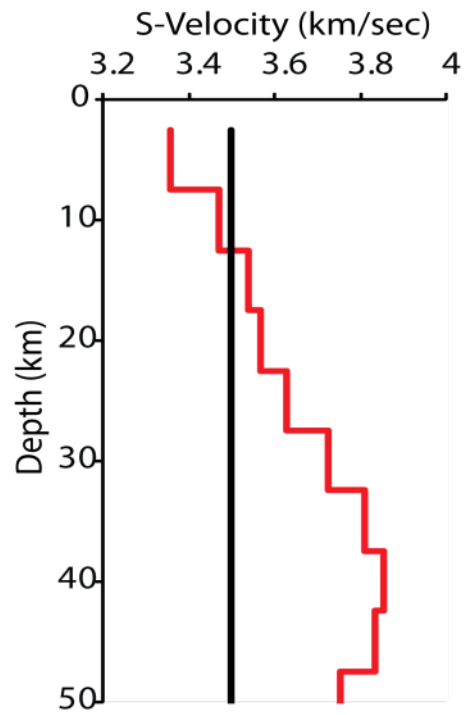


Figure 4-9. 1D inversion model (red line) for the averaged dispersion curves, the initial model (black line) is a constant  $V_s = 3.5$  km/sec.

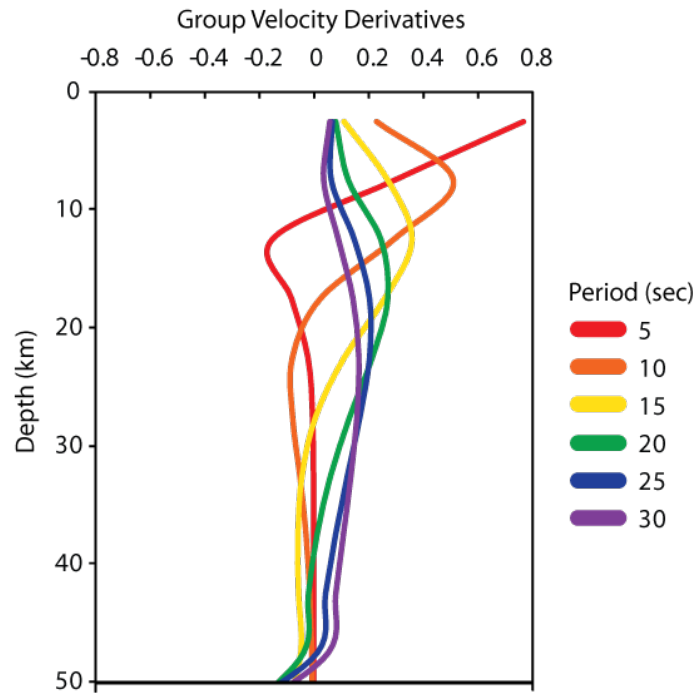


Figure 4-10. Group velocity derivatives of the calculated model with respect to the initial model.

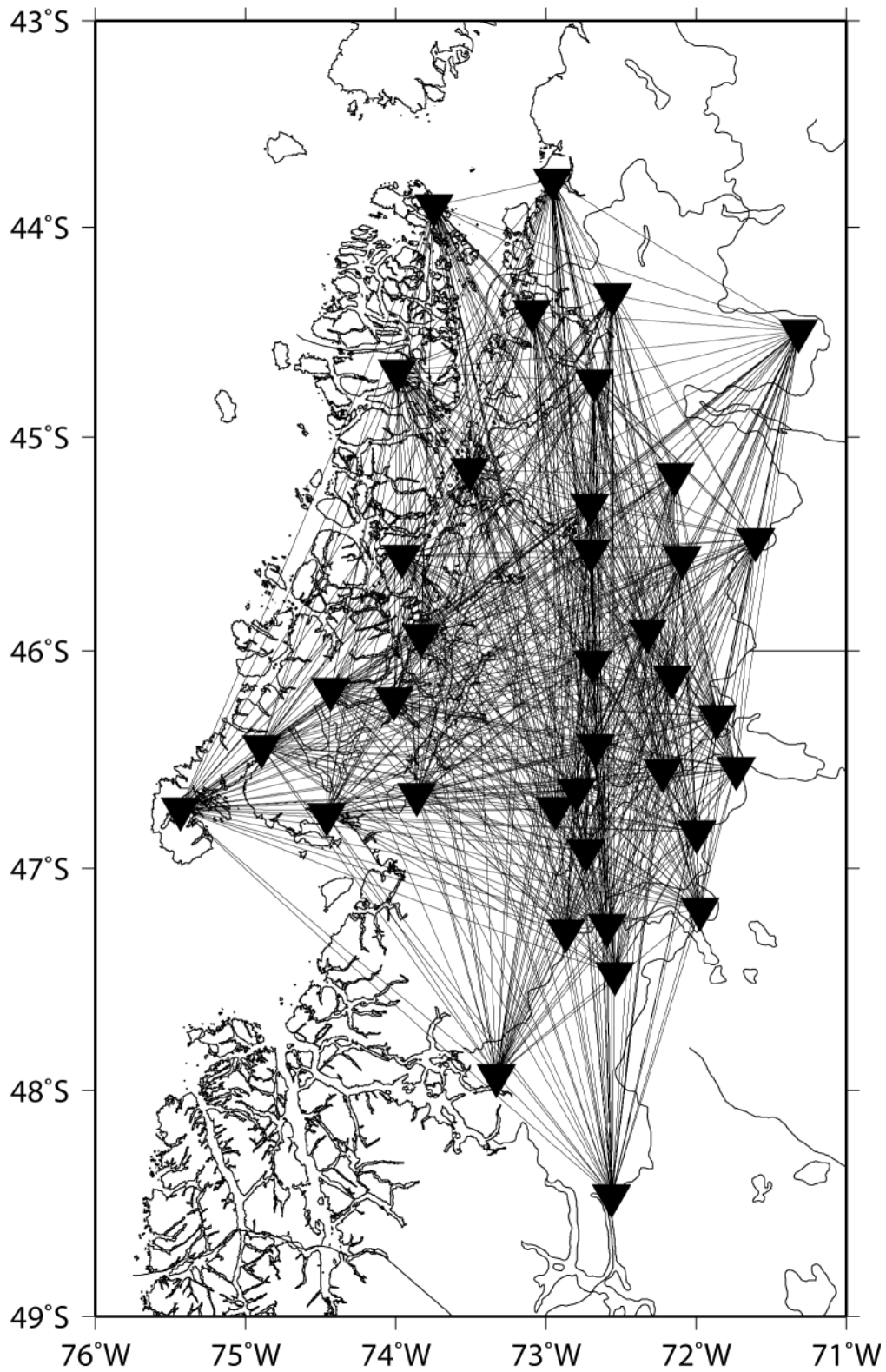


Figure 4-11. Interstation paths for group velocities derived from Green's functions filtered at 5-10 sec period. A total of 640 paths were selected

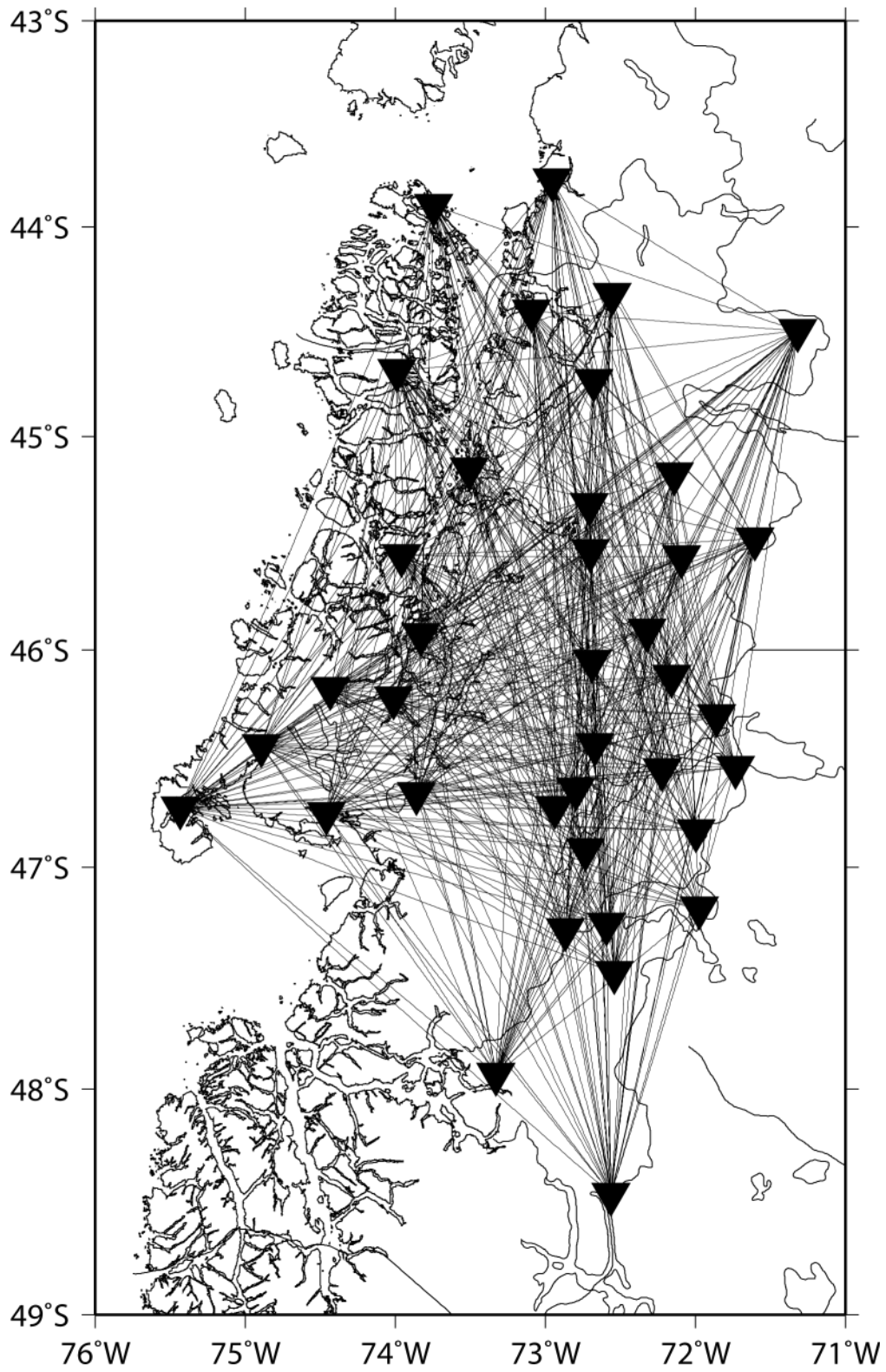


Figure 4-12. Interstation paths for group velocities derived from Green's functions filtered at 10-20 sec period. A total of 454 paths were selected

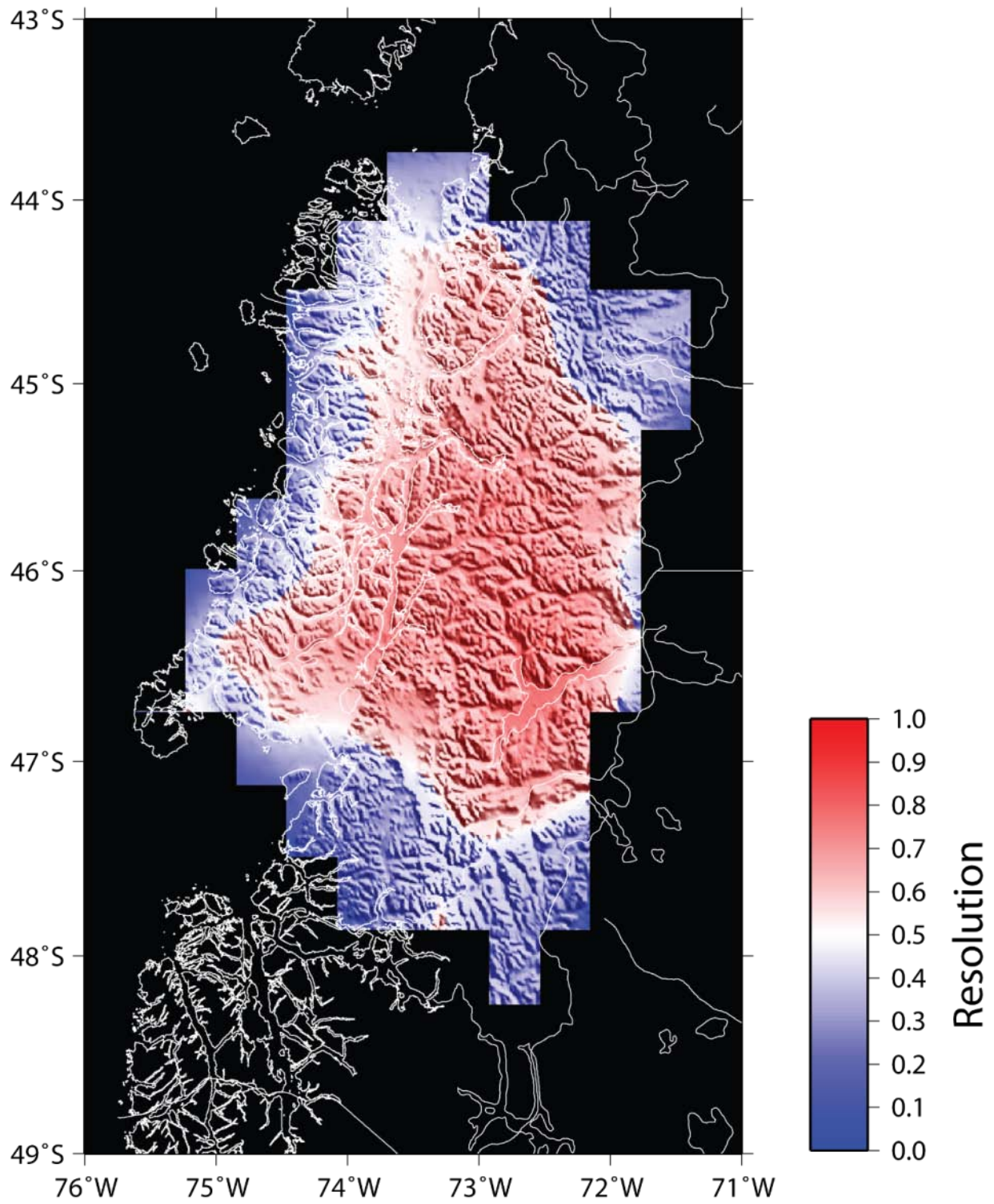


Figure 4-13. Resolution map for 5-10 sec period group velocities.

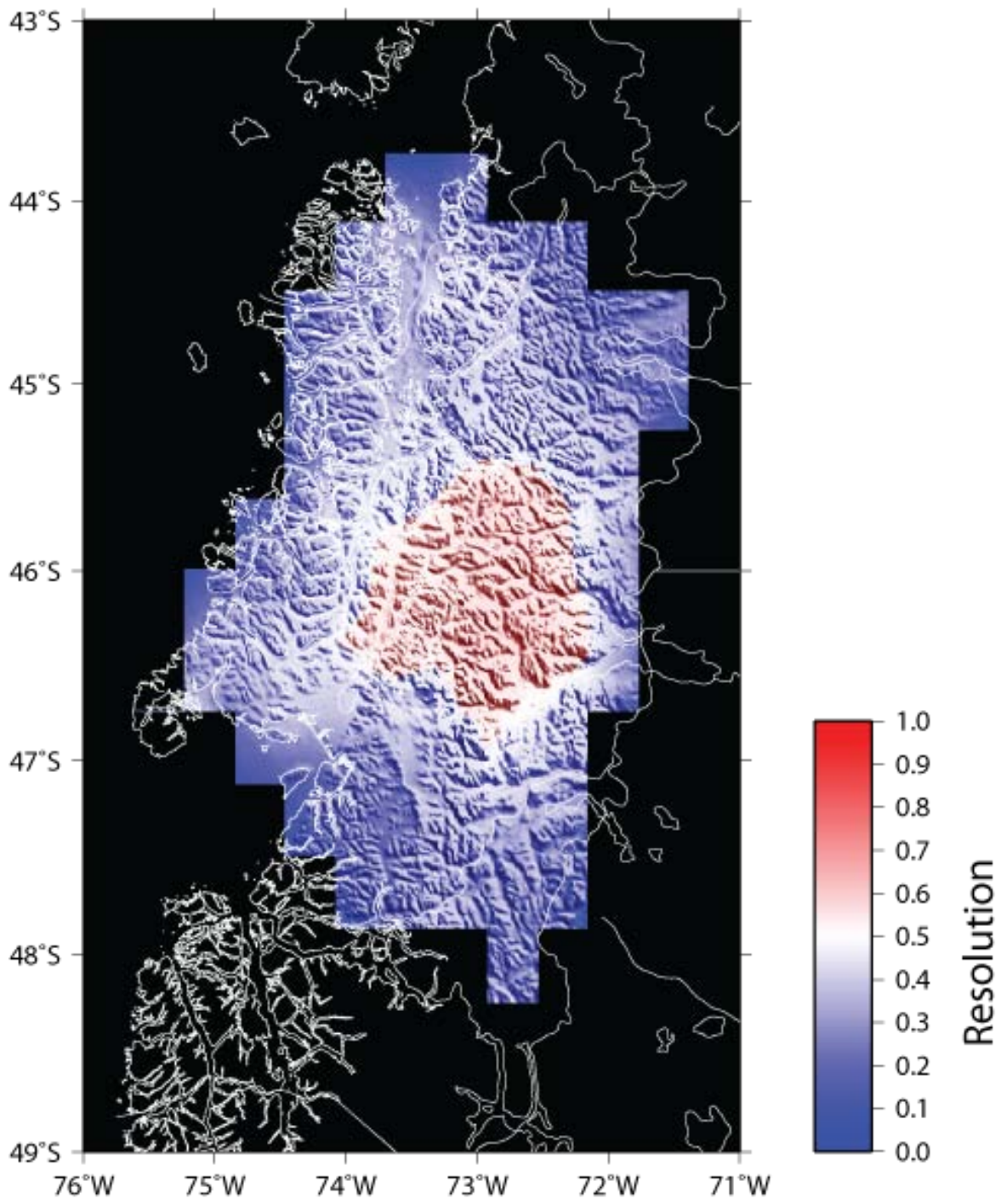


Figure 4-14. Resolution map for 10-20 sec period group velocities.

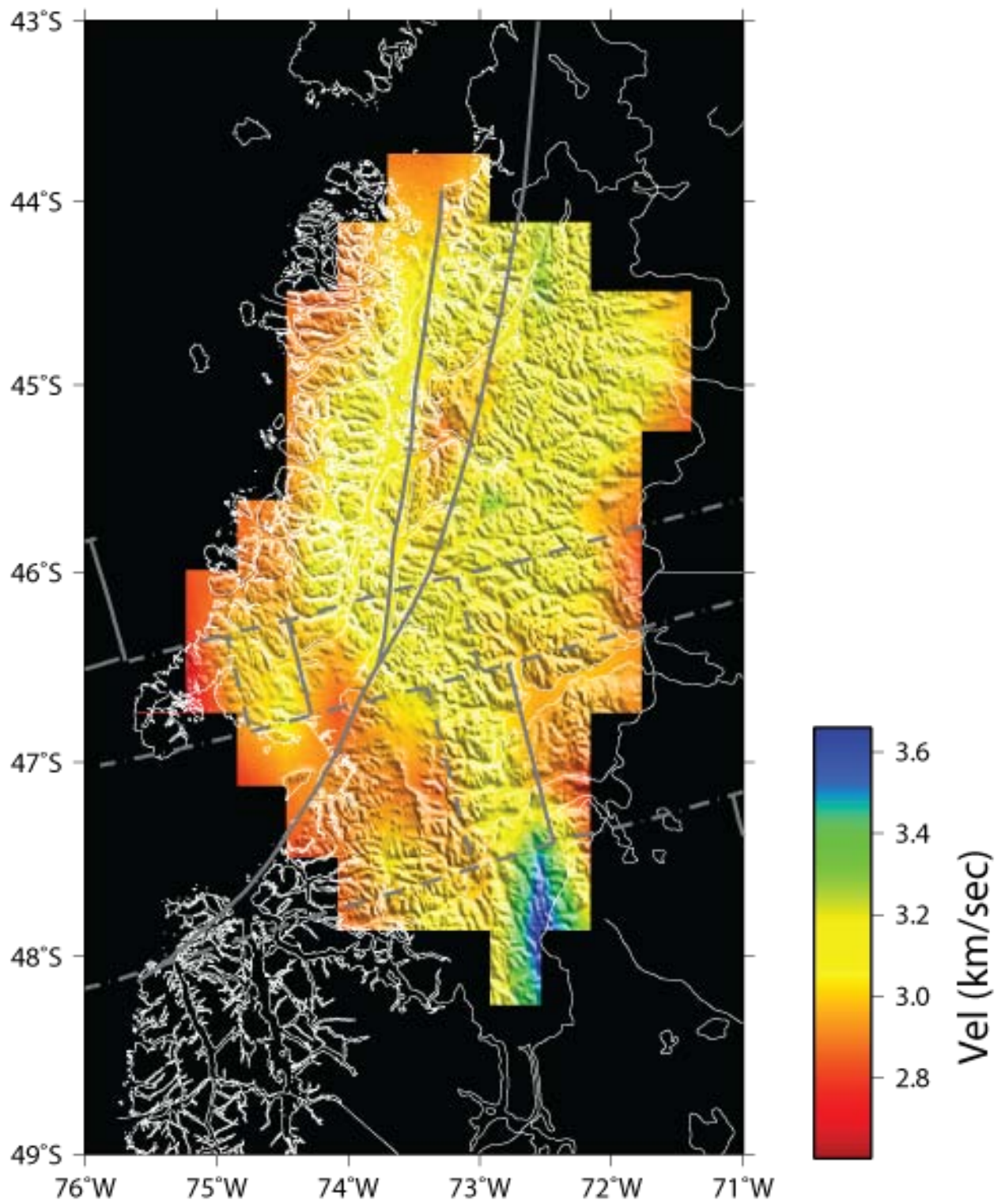


Figure 4-15. Group velocity model for 5-10 sec periods.

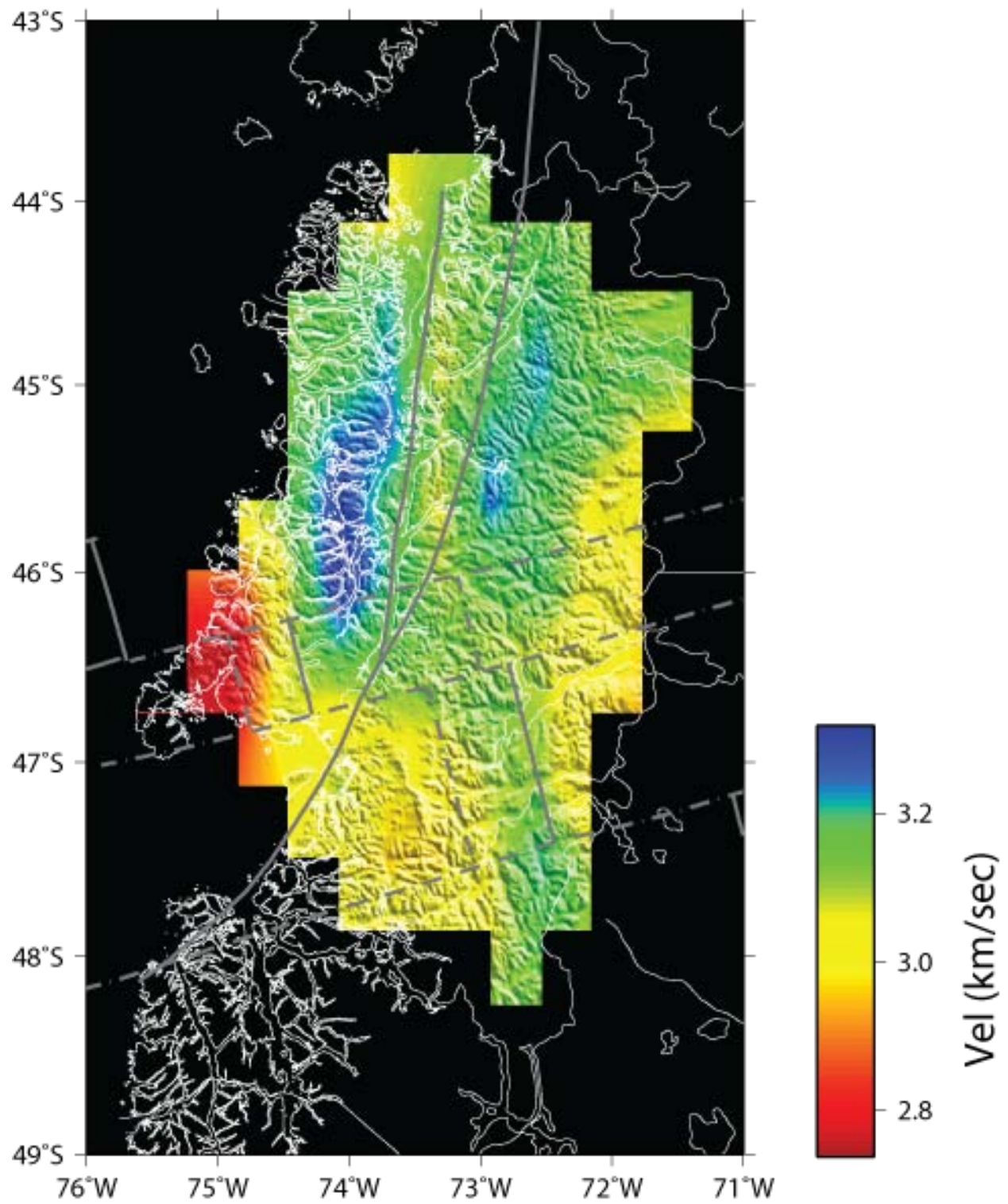


Figure 4-16. Group velocity model for 10-20 sec periods.

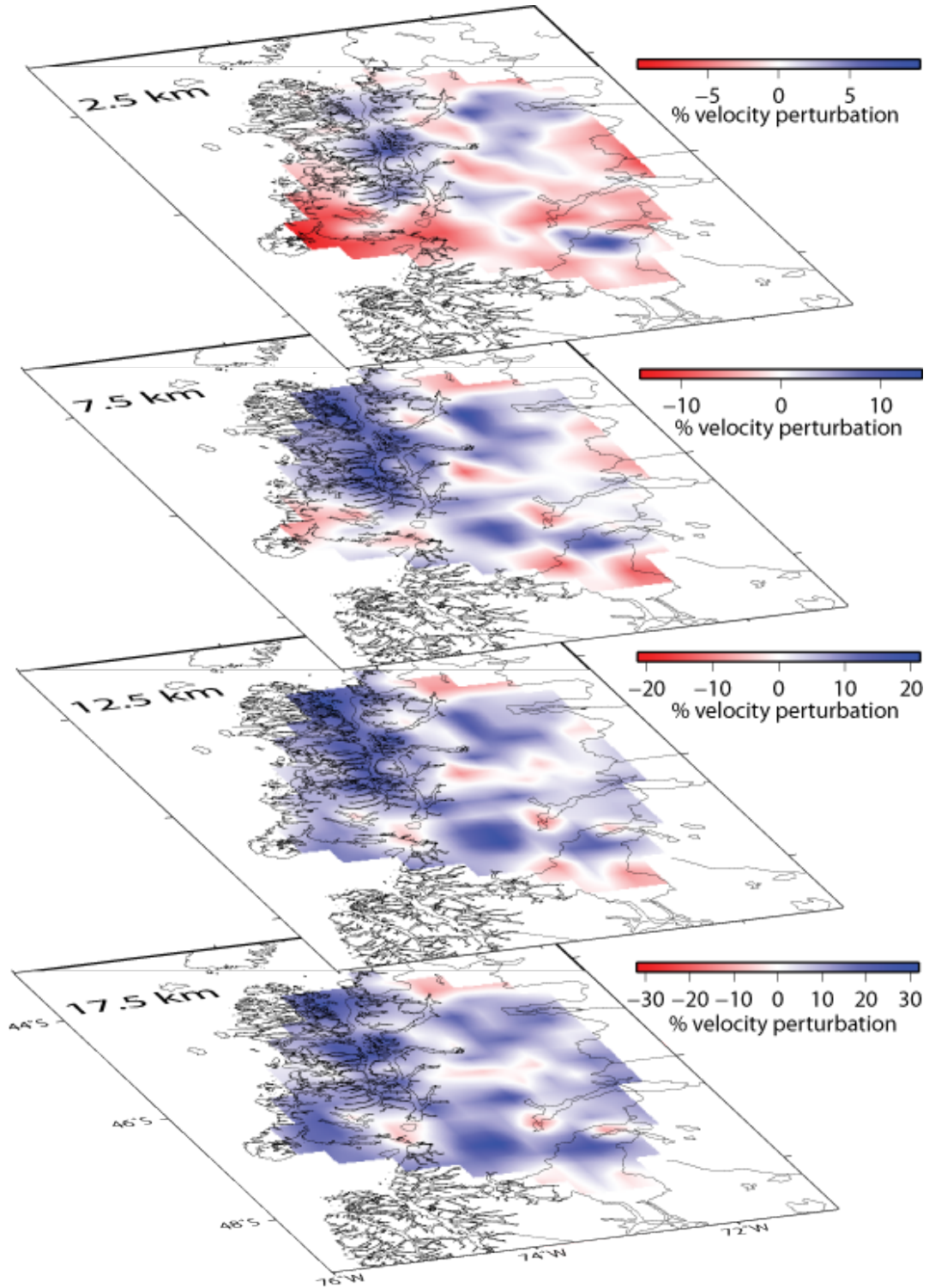


Figure 4-17. 3D inversion calculated using dispersion analysis, the color bands correspond to the percentage variation with respect to the initial model (3.5 km/sec)

CHAPTER 5  
AZIMUTHAL ANISOTROPY OF THE UPPER CRUST FROM AMBIENT SEISMIC NOISE  
AT THE CHILE TRIPLE JUNCTION

**1.20 Introduction**

At different length scales, measurements of seismic anisotropy have been broadly used to constrain the mineralogy and dynamics of the crust and mantle (Silver 1996, Maggi et al. 2006). The main effects of anisotropy on seismic wave propagation are variations of  $P_n$  velocities (Hearn 1996), S-wave splitting (Crampin 1994), Love and Rayleigh wave incompatibility (Anderson 1961), and the azimuthal variation of surface wave velocities (Smith and Dahlen 1973).

Azimuthal anisotropy is observed when seismic wave velocities vary as a function of horizontal direction. Shear waves traveling in the plane of layering are generally faster than shear waves traveling across the layers and the waves become split. The most likely cause of anisotropy in the mantle is the systematic crystal lattice preferred orientation of anisotropic crystals during the mantle flow (Hess 1964, Mainprice and Silver 1993). In the crust, variations of azimuthal anisotropy may result from lattice preferred orientation of minerals, opening of a set of parallel fractures due to horizontal crustal stress, shear deformation that produces strong fabrics in faults zones, sedimentary layering, parallel basaltic dikes, or presence of metamorphic foliations (Crampin 1984).

Assuming isotropic propagation, shear wave velocities derived from Love waves ( $S_H$ ) differ from shear velocities derived from Rayleigh waves ( $S_V$ ). This difference is usually attributed to radial anisotropy due to incompatibility of Love and Rayleigh wave phase velocities (Ekstrom and Dziewonski 1998).  $S_H$  velocity inferred from the dispersion of Love waves is typically observed in horizontal fast layers, and  $S_V$  velocity inferred from the

dispersion of Rayleigh waves is equal in slow and fast horizontal layers, and thus, radial anisotropy is expected to occur in sediments or sedimentary rocks, planar igneous bodies, or rocks with horizontal foliations. Differences in shear velocity are also produced by differences in the shape and size of the averaging areas for both waves, so the dispersion may correspond to dispersion curves averaging different structures.

Several studies have used short period waves (1-20 s) originating from earthquakes to infer the phase velocity and azimuthal anisotropy in the upper crust (Levshin et al. 1992, Li and Detrick 2003, Su et al. 2008). However, (Yao and van der Hilst 2009) used ambient seismic noise, to resolve the azimuthal anisotropy in the upper crust and mantle, and also demonstrated that incoherent noise has little effect (<1%) on the resulting isotropic phase velocities or azimuthal anisotropy.

Previous studies of seismic anisotropy in the upper mantle of the CTJ area were based on shear wave splitting of SKS and S phases. Results reveal that fast axes are parallel to the subducted spreading ridge segments of the Chile Rise, probably as a result of along-axis asthenospheric flow (Murdie and Russo 1999). Subsequently, Russo et al. (2010a,b) showed that anisotropy in this area is highly variable, with fast shear wave propagation typically parallel to the trench north of the CTJ, but more nearly normal to the trench near and south of the Taitao Peninsula, where an actively spreading segment of the Chile Ridge subducted 3 million years ago (Cande and Leslie 1986, Forsythe et al. 1986, Guivel et al. 2006).

This chapter presents results attempting to resolve the complex crustal deformation in the CTJ area due to the Chile ridge collision and the oblique subduction of the Nazca plate using ambient seismic noise. Rayleigh and Love wave phase and group velocities were obtained by cross-correlation of ambient seismic noise recorded at stations between 43°-49°S and 71°-76°W.

Radial anisotropy was resolved from vertical and horizontal shear waves and azimuthal anisotropy from Rayleigh wave phase velocities.

## 1.21 Methodology

### 1.21.1 Radial Anisotropy from Group Velocity of Love and Rayleigh Waves

Rayleigh and Love wave group velocities obtained from dispersion curves (Figure 5-1) of ambient noise cross-correlation (Section 4.3.3) were used to invert for a 2D depth-dependent shear wave velocity structure. In order to obtain Love wave group velocities, the horizontal components (N, E) were rotated into the station-pair azimuth direction. The 2D models were calculated in two inversion steps:

In the first step,  $S_H$  and  $S_V$  velocities were extracted from dispersion curves of Love and Rayleigh waves to obtain a 1D velocity model. The inversion was performed using a linearized least-squared inversion method (Herrmann and Ammon 2002), which minimizes the misfit between the observed and calculated model. The technique evaluates the partial derivatives of group velocity with respect to layers with shear and compressional velocity (Hwang et al. 2003):

$$\Delta C(T_j) = \sum \left( \frac{\partial C(T_j)}{\partial \beta_i} \right) \Delta \beta_i \quad (5-1)$$

where  $\Delta C$  is the difference in phase or group velocity at period  $T_j$ ,  $\Delta \beta$  is the resulting difference in velocity in layer  $i$  with respect to the initial model, and  $N$  is the number of layers. The initial starting model was parameterized as a stack of flat layers 2 km thick with velocities for S wave set to 4.5 km/s and that for P waves set 8.0 km/s. These constant, high (mantle) velocities were chosen to allow the inversion routine to change the model without introducing any sharp velocity discontinuities that would persist during the inversion.

In the second step, the 1D inversion for  $S_H$  and  $S_V$  velocities for each station pair was

used to invert for a 2D model of  $S_H$  and  $S_V$  velocities at 2, 6, 12 and 18 km depth. The inversion was carried out using the Tarantola (2005) least-squares inversion method (Section 4.3.4). The study area was parameterized with cells of 30 x 30 km and for each cell, the calculated radial anisotropy  $\xi$  (Figure 5-2) is:

$$\xi = (S_h/S_v)^2 \quad (5-2)$$

### 1.21.2 Azimuthal Anisotropy from Phase Velocity Rayleigh Waves

Seismic wave velocities in an anisotropic medium depend on the direction of propagation or polarization of the wave, causing azimuthal variations of the surface wave velocities. The wave velocity is not independent of the medium's elastic parameters, so the inversion for velocity also yields the value of these parameters and the trade-off between them.

The azimuthal dependence of Love or Rayleigh wave velocity in a mildly anisotropic medium has  $2\theta$  and  $4\theta$  dependence (Smith and Dahlen 1973), and can be written:

$$C(\omega, \theta) = C_0(\omega) + A_1(\omega) \cos 2\theta + A_2(\omega) \sin 2\theta + A_3(\omega) \cos 4\theta + A_4(\omega) \sin 4\theta \quad (5-3)$$

where  $C$  is the phase velocity,  $\omega$  is the frequency of the wave, and  $\theta$  corresponds to the azimuth along the path. The coefficient  $A_0$  is the isotropic term, while the remaining  $A_i$  are the anisotropic coefficients that govern azimuthal dependence of phase velocity. The coefficients  $A_i$  depend on the combinations of the elastic moduli through depth integration. The constant  $C_0$  is an average velocity over all azimuths, and depends on five independent parameters,  $A, C, F, L,$  and  $N$  (Love, 1944)

The elastic moduli for anisotropic materials contain 21 independent components  $C_{ij}$  that relate the stress and strain tensor. Using the formulation provided by Montagner and Nataf (1986), the notation of the anisotropic moduli with the 1-axis oriented  $N$  and the 2-axis oriented

East can be written as:

$$A = \rho P_h^2 = \frac{3}{8}(C_{11} + C_{22}) + \frac{1}{4}C_{12} + \frac{1}{2}C_{66} \quad (5-4)$$

$$C = \rho P_v^2 = C_{33} \quad (5-5)$$

$$F = \frac{1}{2}(C_{13} + C_{23}) \quad (5-6)$$

$$N = \rho S_h^2 = \frac{1}{8}(C_{11} + C_{22}) - \frac{1}{4}C_{12} + \frac{1}{2}C_{66} \quad (5-7)$$

$$L = \rho S_h^2 = \frac{1}{2}(C_{44} + C_{55}) \quad (5-8)$$

The  $\cos 2\theta$  and  $\sin 2\theta$  terms of equation (5-3) are related to:

$$B_C = \frac{1}{2}(C_{11} - C_{22}) \quad (5-9)$$

$$G_C = \frac{1}{2}(C_{55} - C_{44}) \quad (5-10)$$

$$H_C = \frac{1}{2}(C_{13} - C_{23}) \quad (5-11)$$

$$B_S = C_{16} + C_{26} \quad (5-12)$$

$$G_S = C_{54} \quad (5-13)$$

$$H_S = C_{36} \quad (5-14)$$

The  $\cos 4\theta$  and  $\sin 4\theta$  depend on the depth integrals of:

$$E_C = N - C_{66} \quad (5-15)$$

$$E_S = \frac{1}{2}(C_{16} - C_{26}) \quad (5-16)$$

Love waves depend on  $N$ ,  $L$ ,  $G_c$ ,  $G_s$ ,  $E_c$ , and  $E_s$ , and Rayleigh waves depend on all coefficients except  $N$ . The variation of Rayleigh phase velocity can be expressed in terms of the derivatives

for the transverse isotropic elements as:

$$\begin{aligned}
\delta C_R &= \frac{\partial C_R}{\partial A} (\delta A + B_C \cos 2\theta + B_S \sin 2\theta + E_C \cos 4\theta + E_S \sin 4\theta) \\
&+ \frac{\partial C_R}{\partial C} \delta C + \frac{\partial C_R}{\partial F} (\delta F + H_C \cos 2\theta + H_S \sin 2\theta) \\
&+ \frac{\partial C_R}{\partial L} (\delta L + G_C \cos 2\theta + G_S \sin 2\theta)
\end{aligned} \tag{5-17}$$

The variation of Love phase velocity can be expressed in terms of the derivatives for the transverse isotropic elements as:

$$\begin{aligned}
\delta C_L &= \frac{\partial C_L}{\partial L} (\delta L - G_C \cos 2\theta + G_S \sin 2\theta) + \\
&+ \frac{\partial C_L}{\partial N} (\delta C - E_C \cos 4\theta - E_S \sin 4\theta)
\end{aligned} \tag{5-18}$$

$\partial C_R / \partial L$  is the dominant partial derivative for Rayleigh waves, and  $\partial C_L / \partial N$  for Love waves.

Then the surface waves can be resolved by the combination of:

$$\delta \hat{L} = \delta L + G_C \cos 2\theta + G_S \sin 2\theta \tag{5-19}$$

and

$$\delta \hat{N} = \delta N - E_C \cos 4\theta - E_S \sin 4\theta \tag{5-20}$$

The  $\delta \hat{L}$  parameter controls the SV velocity and the  $\delta \hat{N}$  parameter controls the SH velocity, with both waves propagating horizontally with azimuth  $\theta$ .

The amplitude of the  $2\theta$  azimuthal anisotropy is defined as:

$$\psi_{2\theta} = \sqrt{A_1^2 + A_2^2} \tag{5-21}$$

And the direction of the fast wave is defined to be:

$$\phi = \frac{1}{2} \arctan \left( \frac{A_2}{A_1} \right) \tag{5-22}$$

### 1.21.3 2-D Travel Time Inversion for Anisotropic Terms

The azimuthal variation of phase velocity was obtained from inversion of travel time phase velocities. Using the least-squared inversion (Section 4.3.4) developed by Tarantola (2005), the phase velocity of Rayleigh waves was inverted simultaneously for the spatial distribution of the isotropic  $A_0$ , and anisotropic  $A_1$  and  $A_2$  terms. These terms were included in the matrix inversion (4-4).

The inversion is mainly controlled by three parameters, the damping,  $L$ , the a priori standard deviation of isotropic terms,  $\sigma_i$ , and the standard deviation for anisotropic terms,  $\sigma_a$  in the equation (4-5). The optimal values for these parameters were selected by applying two synthetic checkerboard (Figure 5-3) tests and a Chi-squared statistical analysis. The first checkerboard tests was constructed with blocks of  $120 \text{ km}^2$  with velocity anomaly of  $2 \text{ km/s}$  with a fast shear propagation direction oriented  $90^\circ\text{N}$ , and velocity anomaly cells of  $3 \text{ km/s}$  with fast shear propagation oriented  $0^\circ\text{N}$ . The inversion was performed using 665 ray paths, which is the number of ray paths obtained from the dispersion analysis for the 6 sec period. The second checkerboard test was constructed with a homogeneous layer with phase velocity of  $2 \text{ km/s}$  and fast shear propagation oriented EW, and an elongated N-S velocity anomaly of  $3 \text{ km/s}$ ,  $60 \text{ km}$  wide, and fast shear propagation oriented N-S, simulating a shear zone of the LOFZ with fast ray parallel to the fault (Figure 5-3). For the joint inversion, a good balance between over- and under-fitting data was obtained using a damping parameter of  $L = 63.2 \text{ km}$ , standard deviations of  $\sigma_1$  equal to  $0.005 \text{ km/s}$  for the isotropic term and  $\sigma_2$  equal to  $0.005 \text{ km/s}$  for the anisotropic term. The checkerboard test inversion (Figure 5-3a, c) was well resolved for isotropic and anisotropic terms. The elongated anomaly (Figure 5-3b, d) representing the LOFZ was also well resolved, for both isotropic and anisotropic terms, especially between  $44^\circ\text{S}$  and  $46^\circ\text{S}$ . At

the edge of the ray path coverage, the recovery of the resulting model presents some deviation from the synthetic model. The resulting inversion maps (Figure 5-4 to Figure 5-14) can then be directly compared with the tectonic (Figure 1-1) and geologic maps (Figure 1-3) of the region.

The discrepancy between the initial model and the observed model can be determined using the Chi-square test obtained from:

$$\chi^2 = (Gm_{prior} - d_{obs})^t (GC_M G^t + C_D)^{-1} (Gm_{prior} - d_{obs}) \quad (5-23)$$

The null hypothesis establishes that the calculated travel times obtained with the new velocity model have a similar distribution to the observed travel times, and are independent. The lower the significance level, the more the data must diverge from the null hypothesis to be significant; a significance level of 0.05 assures a balance between over- and under-fitting data.

Resolution maps of the isotropic and anisotropic-joint inversion were included in the analysis. Resolution depends on ray path density, the frequencies of the Rayleigh waves, and the smoothing length used in the inversion.

The phase velocity maps presented in Figure 5-4 to Figure 5-14 include an isotropic-only model, determined without the  $A_1$ , and  $A_2$  terms; an anisotropic-only model without the  $A_0$  term; a joint inversion with the  $A_0$ ,  $A_1$  and  $A_2$  terms, and the resolution map. In total, ten 2D phase velocity models of Rayleigh waves were selected. The measurements correspond to period bands between 5 and 15 sec. Inversions for periods greater than 15 s resulted in poor ray coverage and were not included.

## 1.22 Results

Resulting average dispersion curves of Love and Rayleigh waves (Figure 5-1) for the CTJ area show higher velocities for Love waves than Rayleigh waves. Radial anisotropy models for shear wave velocity were obtained from inversion of Rayleigh and Love group

velocity. 2D inversion maps at 0, 6, 12 and 18 km depth (Figure 5-2) show the radial anisotropy index  $\xi$ . The maps reveal higher values of radial anisotropy at deeper levels. The most consistent anomalies are a highly anisotropic region west of the Chonos Archipelago, and low radial anisotropy in the SW of the study area and along the two strands of the LOFZ.

Inversion of Rayleigh wave phase velocities resulted in ten 2D models of azimuthal anisotropy for periods between 5 and 15 s (Figure 5-4 to Figure 5-14).

West of the study area, between 44°S and 47°S, the joint inversion for phase velocities at periods between 5 - 13 s reveals high anisotropy (>1%) and a high phase velocity (3.2-3.6 km/s). The fast direction of anisotropy is consistent at all periods, striking NNE. At all periods, for the region east of the volcanic arc and the LOFZ, the joint and isotropic inversions exhibit an elongated anomaly with medium to high velocity (>3.0 km/s), and patches of high velocity (>3.2 km/s) that correspond to the LCPB. In general, the anisotropy is lower (<1%) here relative to other units. At longer periods (14-15 s), there is a clear difference between a high anisotropy region west of the LOFZ, and a region of lower anisotropy to the east. This area also presents the lowest anisotropy in the anisotropic model.

Between the two branches of the LOFZ, where the MPB is emplaced, the joint inversion yields areas of relatively low velocity (2.9-3.0 km/s) and anisotropy > 1%. The fast shear wave propagation trend is consistently oriented subparallel to the LOFZ, and is more evident for periods longer than 10 sec. In the anisotropic model, the coincidence between the fast shear wave direction and the strike of the LOFZ is noticeable. South of the CTJ, in the Taitao Peninsula and Golfo de Penas, all periods show a low velocity anomaly (<2.9 km/s) and high anisotropy (>1.55%). In the joint and anisotropic models, the fast shear wave trend exhibits a gradual change in orientation from NNW in the Taitao Peninsula to NNE in the Golfo de Penas.

In the SE, for periods between 5 and 9 s in the joint model, the presence of the EMC coincides with the greatest anisotropy (>2%), with fast shear wave trend oriented NNW and phase velocity (>3.1 km/s). The high velocity anomaly in the isotropic model is larger in extent in comparison with that seen in the joint inversion. For periods between 5 to 9 s, more restricted regions of relatively low velocity (< 2.9 km/s) and anisotropy > 1% with NNW-trending fast shear propagation appear in two small areas to the east that correlate with volcanoclastic deposits of the Patagonian Range, with a high anisotropy trending NNW.

### 1.23 Discussion

The radial and azimuthal anisotropic inversion maps include features that can be correlated in straightforward fashion with the surface geology of the study area. In general, the major velocity and anisotropic anomalies that appear in both the isotropic and anisotropic joint inversions can also be seen in the isotropic-only and anisotropic-only model, indicating that the inclusion of the anisotropic terms does not introduce major artifacts into our final model.

Average Rayleigh (Figure 5-1) wave phase velocities range between 3.0 km/s, at 5 s, to 3.2 km/s at 20 s, typical of upper crust values (Dziewonski and Anderson 1981). Between 5 and 11 s, phase velocities increase from 3.0 km/s to 3.13 km/s, probably due to the presence of sedimentary and pyroclastic deposits restricted to the shallow crust, transitioning to granitic and metamorphic rocks at deeper levels. Between 11 and 16 s, a decrease in velocity from 3.13 to 3.11 km/s could indicate magma infiltration of some areas associated with the volcanic arc, and geothermal areas near the Taitao Peninsula. Between 16 and 20 s an increase in velocity from 3.11 to 3.2 km/s is probably related to less differentiated rocks of the LCPB, since seismic velocities decrease as the silica content decreases (Christensen and Mooney 1995).

High phase velocities (>3.1 km/s) and variable anisotropy occur in the region where the LCPB outcrops (Figure 5-4 to Figure 5-14). Two elongated bodies of high velocity east and

west of the MPB are well resolved primarily in the isotropic model, probably due to the low anisotropy of these granitic rocks. It is noticeable at 6-11 s, and especially at 9 s, that a low velocity region visible in the isotropic and joint model coincides with the presence of the slab window, which may indicate warming of the crust due to Chile Ridge subduction.

In the joint inversion, a consistent orientation of the fast shear wave trend parallel to the LOFZ, with 0.5% to 1% anisotropy and a relatively low phase velocity (3.0 km/s), occurs at all periods, and is especially pronounced at 12 and 15 s periods. This correlation is more evident for the anisotropic inversion, where the trend of the fast shear wave propagation coincides with the LOFZ along its entire length in the study area. The radial anisotropy is low ( $<0.8$ ) at all depths, indicating vertical fabrics or structures are dominant. The LOFZ includes two lineaments west and east of the MPB that correspond to a zone of ductile deformation (Cembrano et al. 1996). This zone was generally shortened in the E-W direction during subduction, and structures and fabric within the area strike  $\sim$ NS and  $\sim$ NE (Cande and Leslie 1986, Arancibia et al. 1999). Strong anisotropy with fast shear wave propagation trending parallel to the LOFZ shear zone at long periods may indicate that deeper levels of the fault are ductilely deformed, whereas the shallow LOFZ is a brittle zone.

West of the WMC, the highest radial anisotropy ( $\xi > 1.2$ ) at all depths and intermediate azimuthal anisotropy ( $>2\%$ ), with consistent N45°E orientation at all periods (5-15 sec), may be related to the highly foliated rocks of the western belt of the WMC. In contrast to the eastern belt, the schists of the western belt are nearly flat lying with a slight dip to the NE (Willner et al. 2000). The existence of abundant mica schists can contribute up to 45% of shear wave splitting in the crust (Godfrey et al. 2000). This occurs because shear waves oscillate faster in the plane of the layered schist than across the layers; thus radial anisotropy is stronger than

azimuthal anisotropy. The anisotropy in the eastern part of the WMC decreases to less than 1%, probably due to the absence of foliation in the eastern belt. The discontinuity in the anisotropy through this metamorphic unit may be related to differences in the thicknesses of the schists, which are thicker where the anisotropy is present at depth. Thinning of this unit can be explained by the rise of magma beneath the WMC during the emplacement of the LCPB.

South of the WMC and CTJ, at periods between 9-15 s, a change from intermediate velocities ( $>3$  km/s) to low velocities ( $<2.9$  km/s) occurs at 9 s in the joint model. This area presents low radial anisotropy ( $<0.9$ ) and strong azimuthal anisotropy ( $>2\%$ ) at periods between 5 to 12 s. The fast shear wave propagation trend gradually changes from NE at the Golfo de Penas basin to NW in the Taitao Peninsula. The high anisotropy and rotation of the fast shear wave trend may be related to the complex deformation due to the subduction of ridge segments, which strike  $N15^{\circ}W$ , and perhaps the right lateral motion of the LOFZ (Cembrano and Herve 1993, Arancibia et al. 1999).

In the SE, south of the EMC, for periods between 5 to 8 s, a region of very high velocities ( $>3.2$  km/s) and high anisotropy ( $>2\%$ ) with fast shear propagation trending NNW coincides with exposed rocks of the basement at the Bahia de la Lancha formation, a folded and metamorphosed succession of turbidites probably formed in the forearc during accretion (Bell and Suarez 2000). The absence of this anomaly for periods longer than 8 s probably indicates the formation does not extend to depth.

East of the study area, between  $44^{\circ}S$  and  $46^{\circ}S$ , a region of low phase velocity ( $< 2.9$  km/s) and variable anisotropy (1 - 2%) generally trending NNW, is visible at periods up to 13 s. This low velocity region coincides with the Jurassic and Lower Cretaceous volcanoclastic deposits of the Patagonian Range.

In the SW, a region of low phase velocity ( $< 2.8$  km/s) and high anisotropy ( $>1\%$ ) with variable fast shear wave trend is somewhat unexpected, due to the presence of the LCPB in major outcrops at the surface. However, this zone lies contiguous to the Golfo de Penas basin, which composed of more than 3 km of sediment that strikes roughly NNW (Forsythe and Nelson 1985).

#### **1.24 Conclusions**

Cross-correlation of ambient seismic noise collected with a network of 44 broadband sensors reveals azimuthal and radial anisotropy of the upper crust in the Chile Triple Junction area. Strong anisotropy with fast shear wave propagation directions trending parallel to the LOFZ is consistent with a wide area of shear deformation that increases at depth. Strong radial anisotropy and high seismic velocities coincide with foliated metamorphic rocks of the western belt of the Western Metamorphic Complex. Intermediate to high velocities and weaker anisotropy appear where the LCPB is present, and high phase velocities and strong anisotropy coincide with the presence of the EMC.

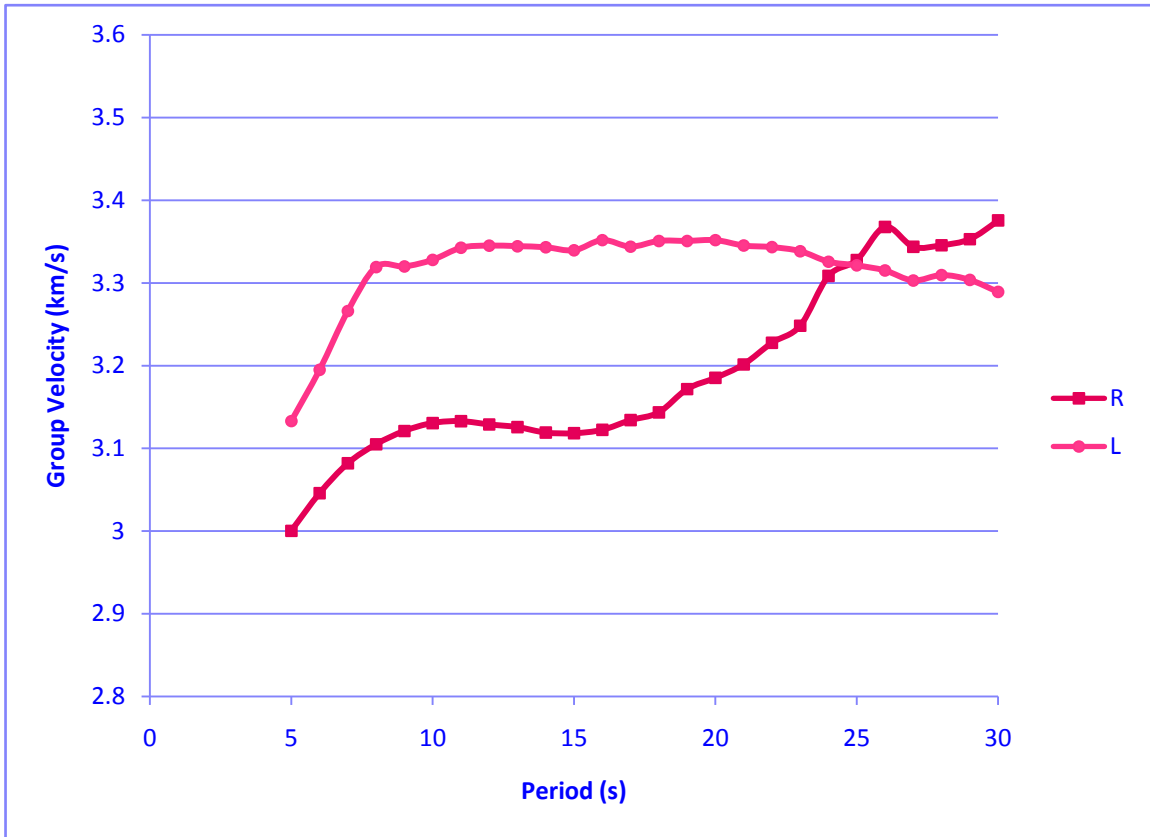


Figure 5-1. Dispersion curves for Rayleigh (R) and Love (L) wave group velocities.

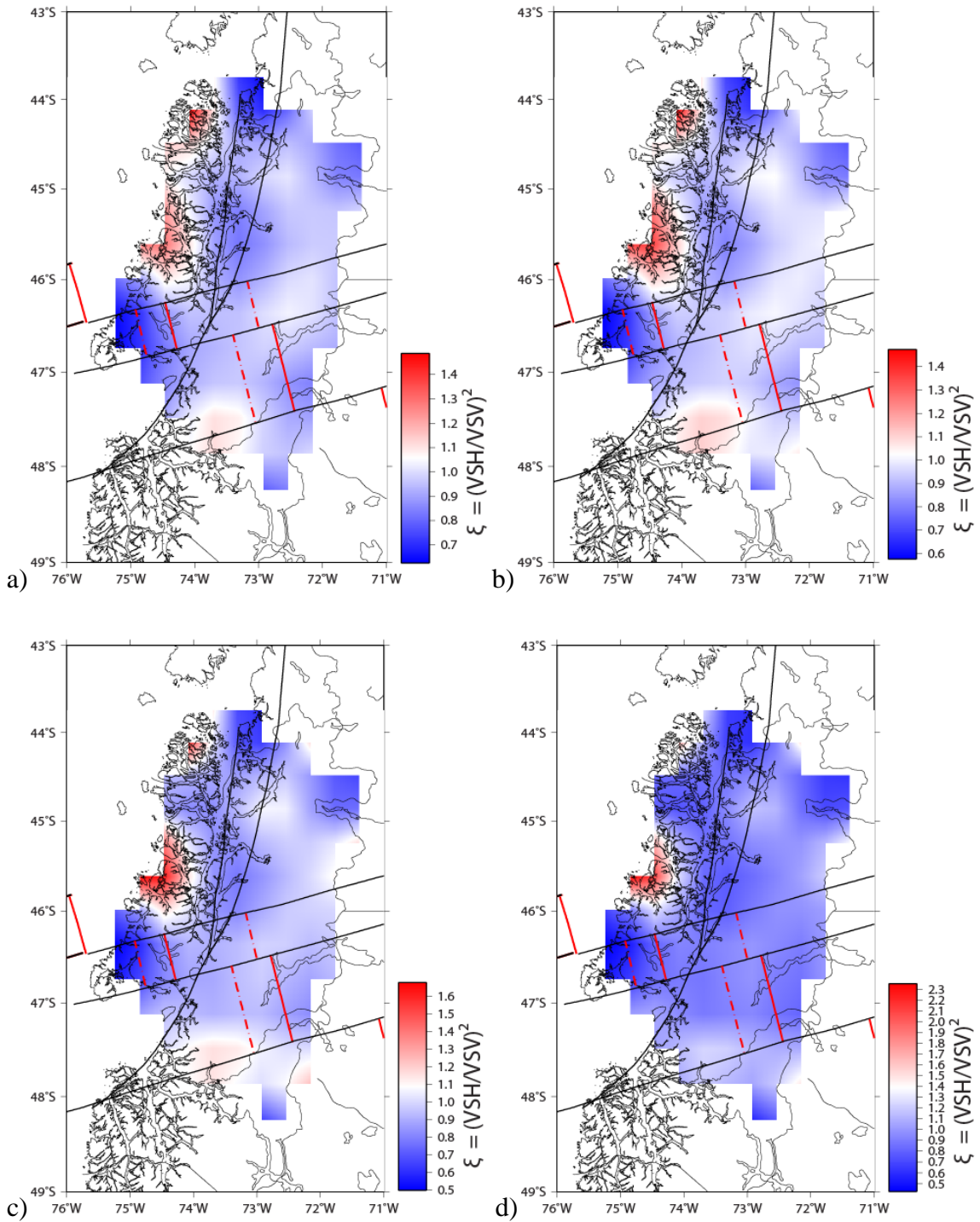


Figure 5-2. Radial anisotropy model in the upper crust at the CTJ. (a) Results of the inversion at 0 km depth. (b) Results of the inversion at 6 km depth (c) Results of the inversion at 12 km depth. (d) Results of inversion at 18 km depth.

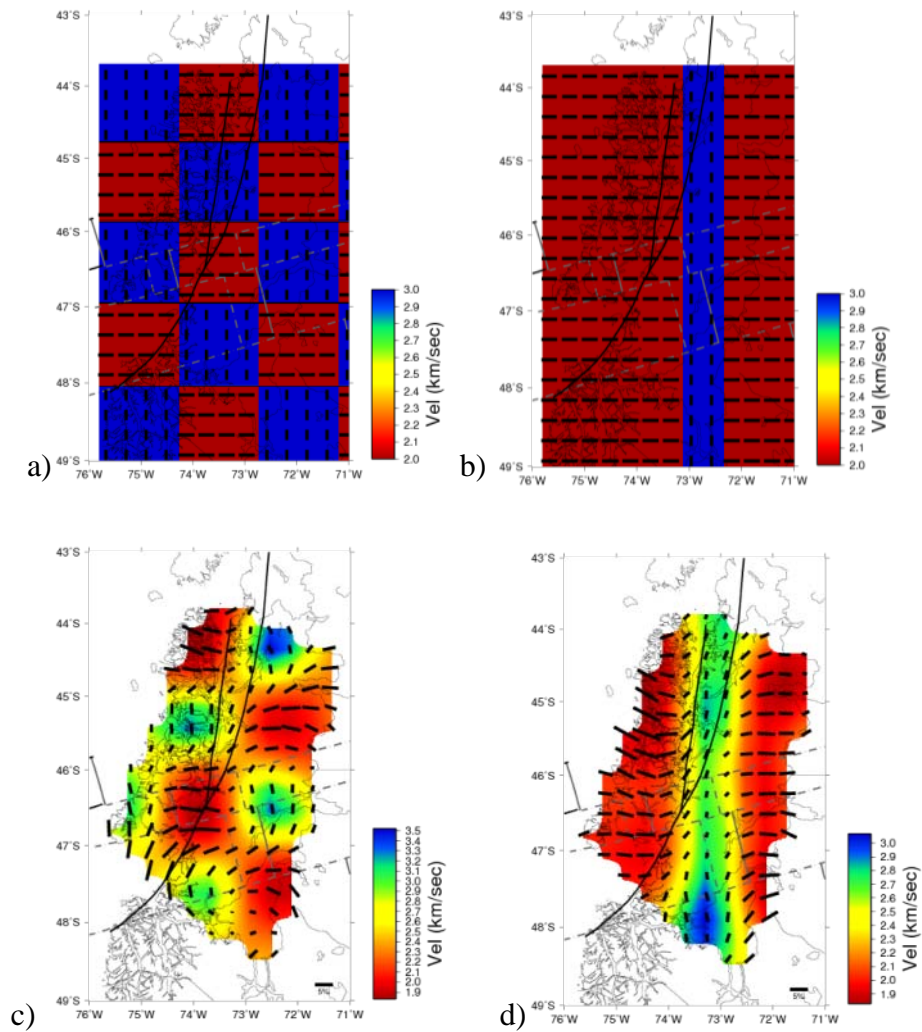


Figure 5-3. Checkerboard test of the study area. (a) Input anomalies, isotropic squares with velocities of 2 km/s and 3 km/s. (b) Input anomalies include homogeneous bands of 2 km/s with E-W anisotropy and an elongated narrow area with 3 km/s and N-S anisotropy. (c) Isotropic and anisotropic joint inversion using 665 ray paths from synthetic model (a). (d) Isotropic and anisotropic joint inversion using 665 ray paths from synthetic model (b).

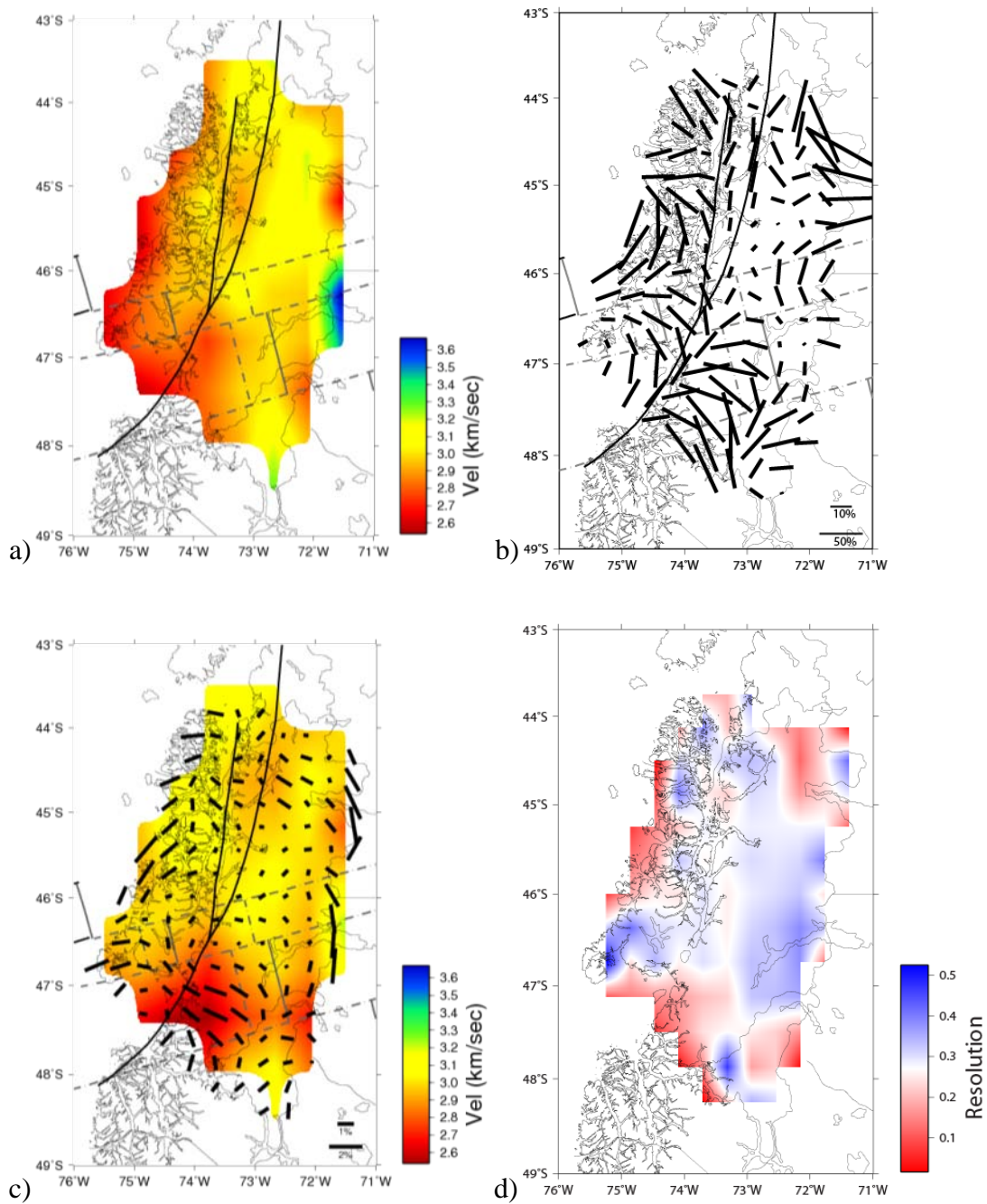


Figure 5-4. Inversion results for 5 sec period. (a) Isotropic inversion. (b) Azimuthal inversion. (c) Azimuthal and isotropic joint inversion. (d) Resolution of joint inversion. Black bars indicate magnitude and orientation of polarized fast ray.

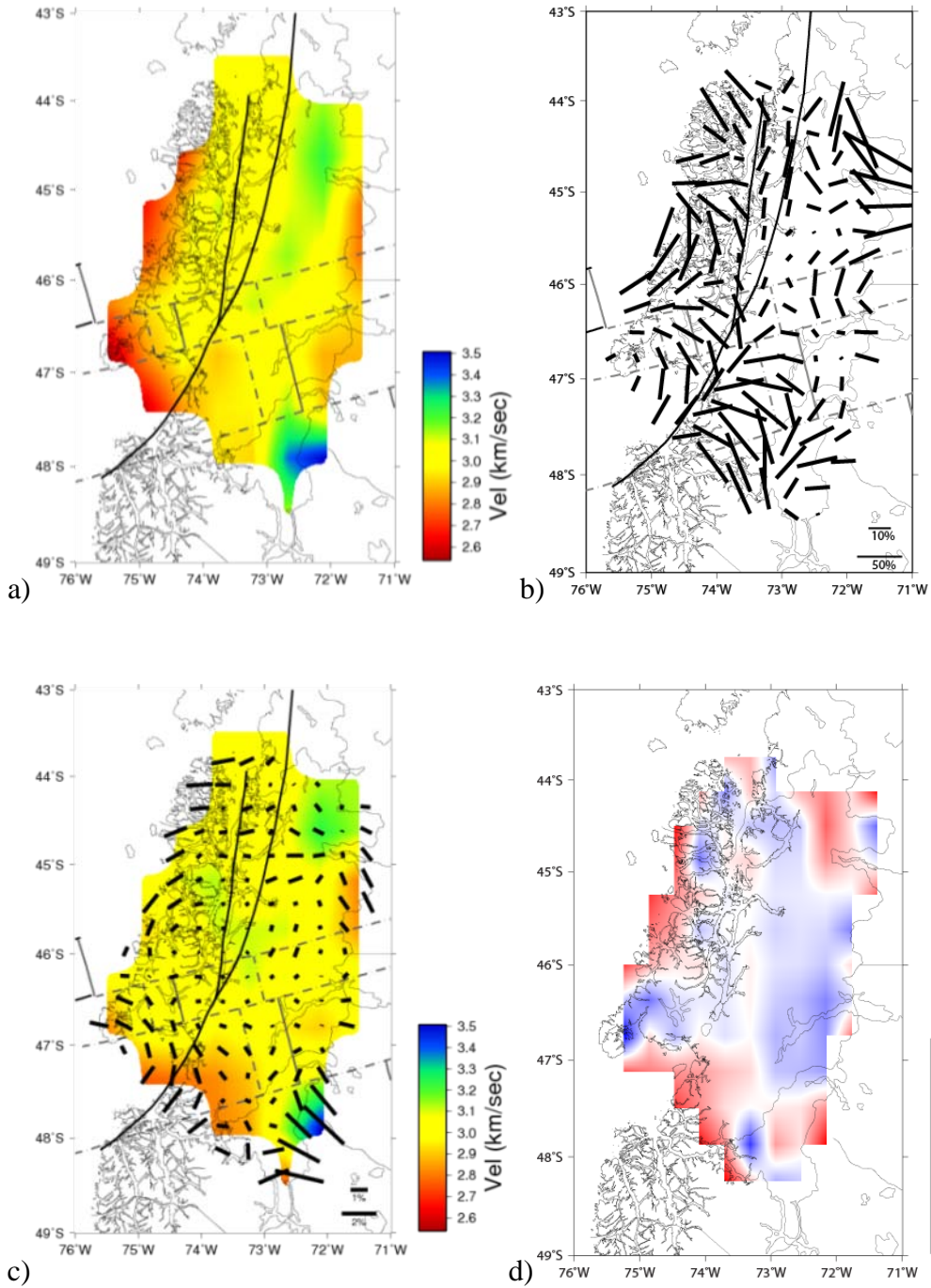


Figure 5-5. Inversion results for 6 sec period. (a) Isotropic inversion. (b) Azimuthal inversion. (c) Azimuthal and isotropic joint inversion. (d) Resolution of joint inversion. Black bars indicate magnitude and orientation of polarized fast ray.

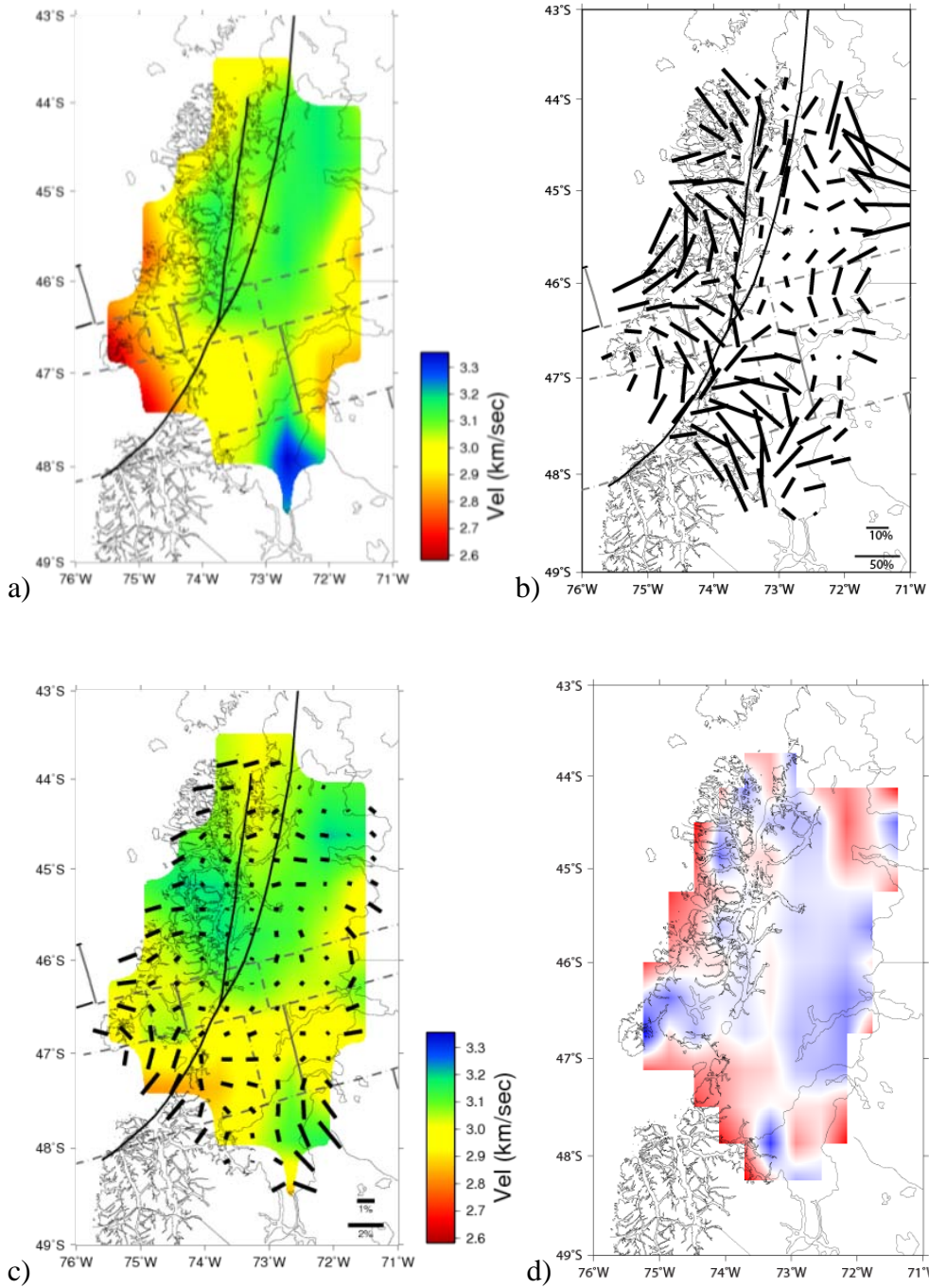


Figure 5-6. Inversion results for 7 sec period. (a) Isotropic inversion. (b) Azimuthal inversion. (c) Azimuthal and isotropic joint inversion. (d) Resolution of joint inversion. Black bars indicate magnitude and orientation of polarized fast ray.

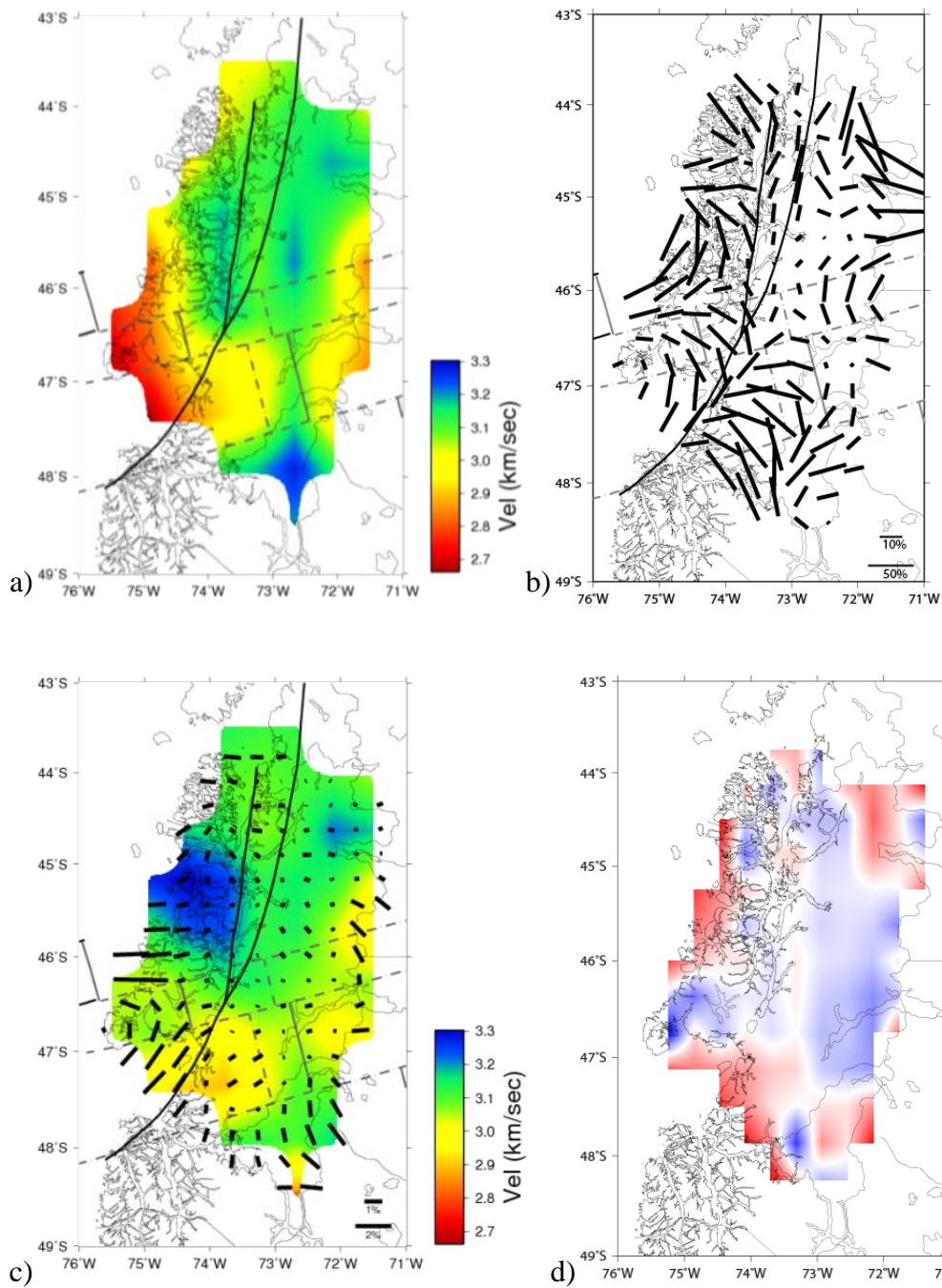


Figure 5-7. Inversion results for 8 sec period. (a) Isotropic inversion. (b) Azimuthal inversion. (c) Azimuthal and isotropic joint inversion. (d) Resolution of joint inversion. Black bars indicate magnitude and orientation of polarized fast ray.

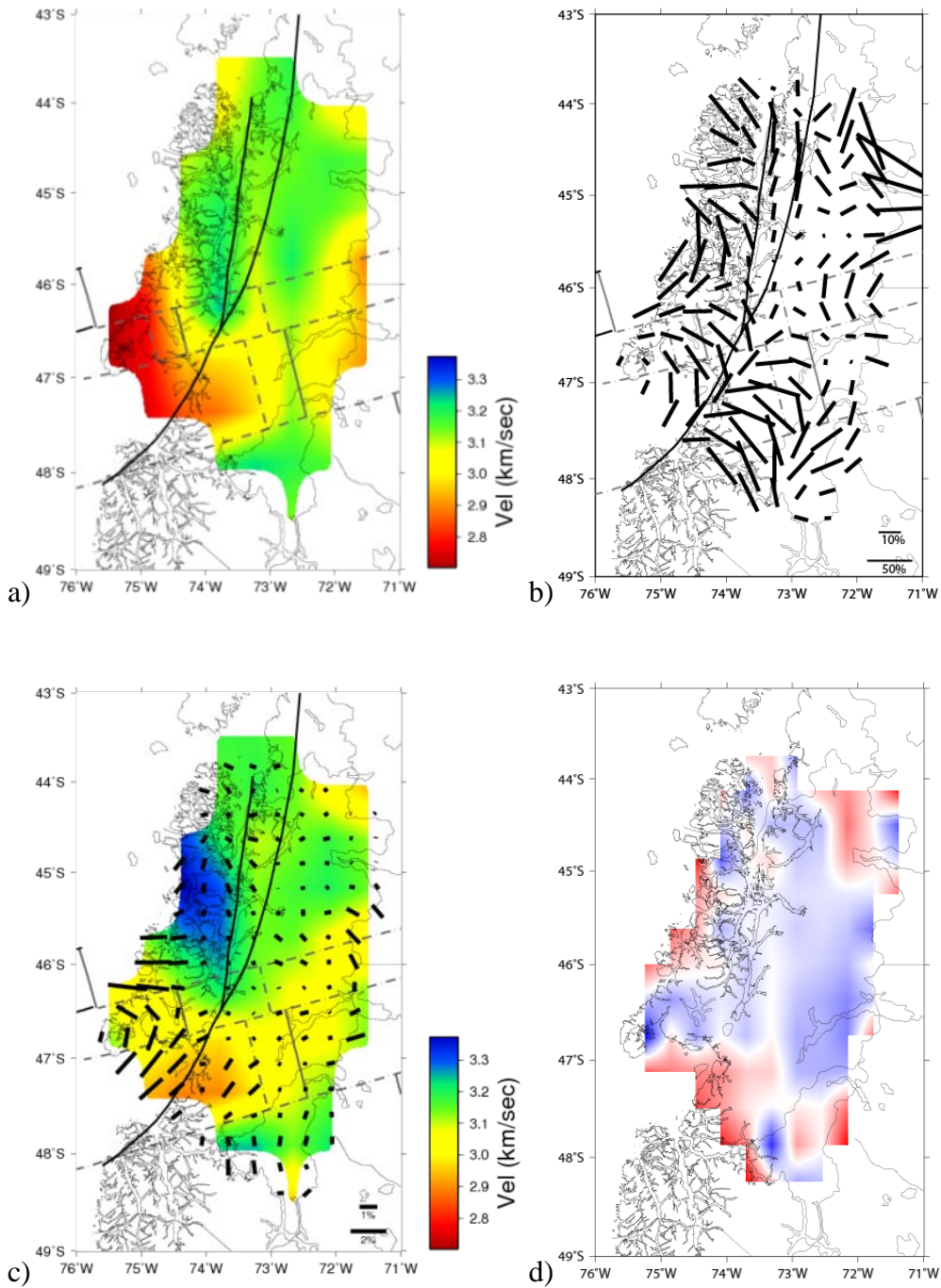


Figure 5-8. Inversion results for 9 sec period. (a) Isotropic inversion. (b) Azimuthal inversion. (c) Azimuthal and isotropic joint inversion. (d) Resolution of joint inversion. Black bars indicate magnitude and orientation of polarized fast ray.

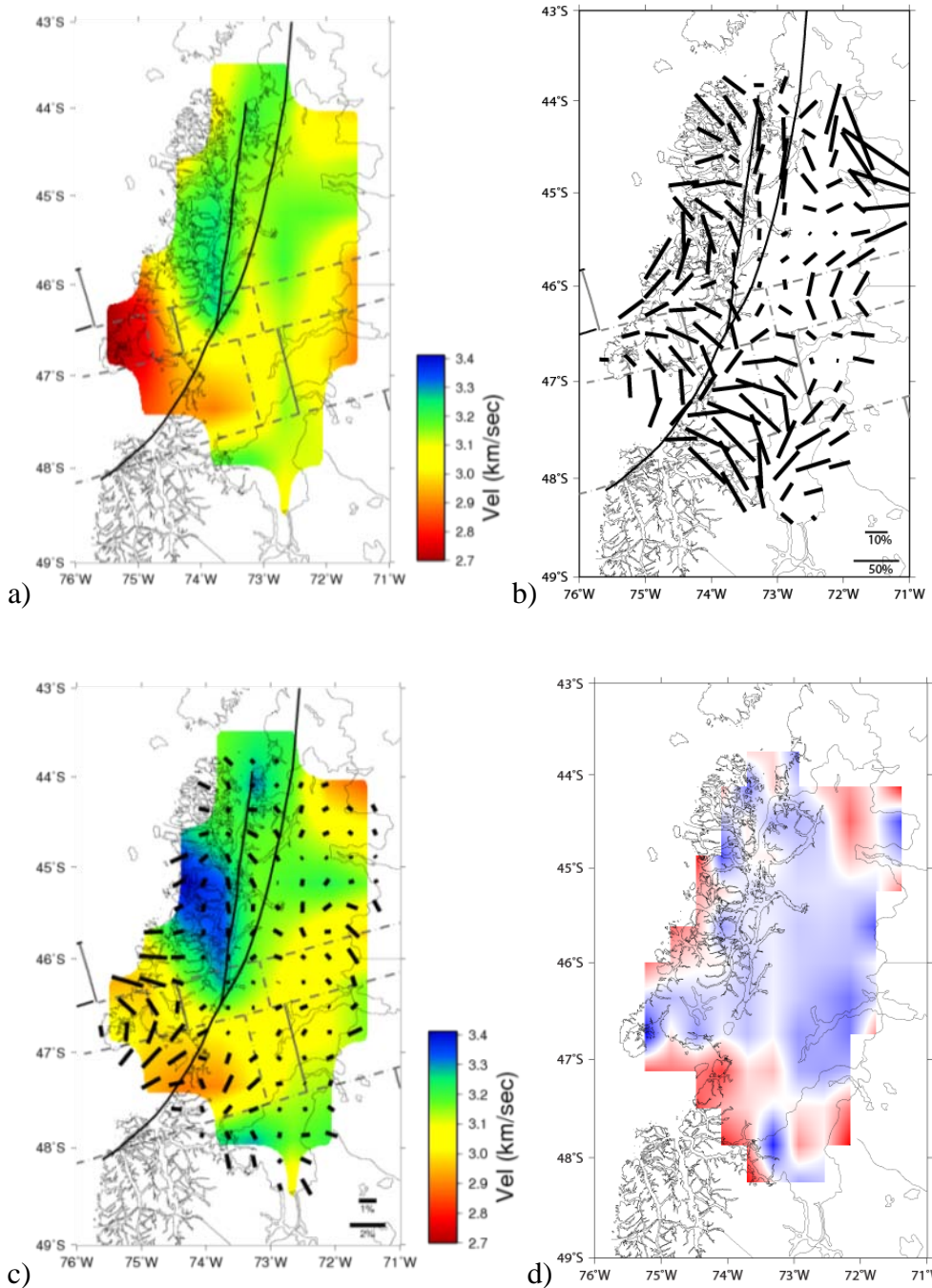


Figure 5-9. Inversion results for 10 sec period. (a) Isotropic inversion. (b) Azimuthal inversion. (c) Azimuthal and isotropic joint inversion. (d) Resolution of joint inversion. Black bars indicate magnitude and orientation of polarized fast ray.

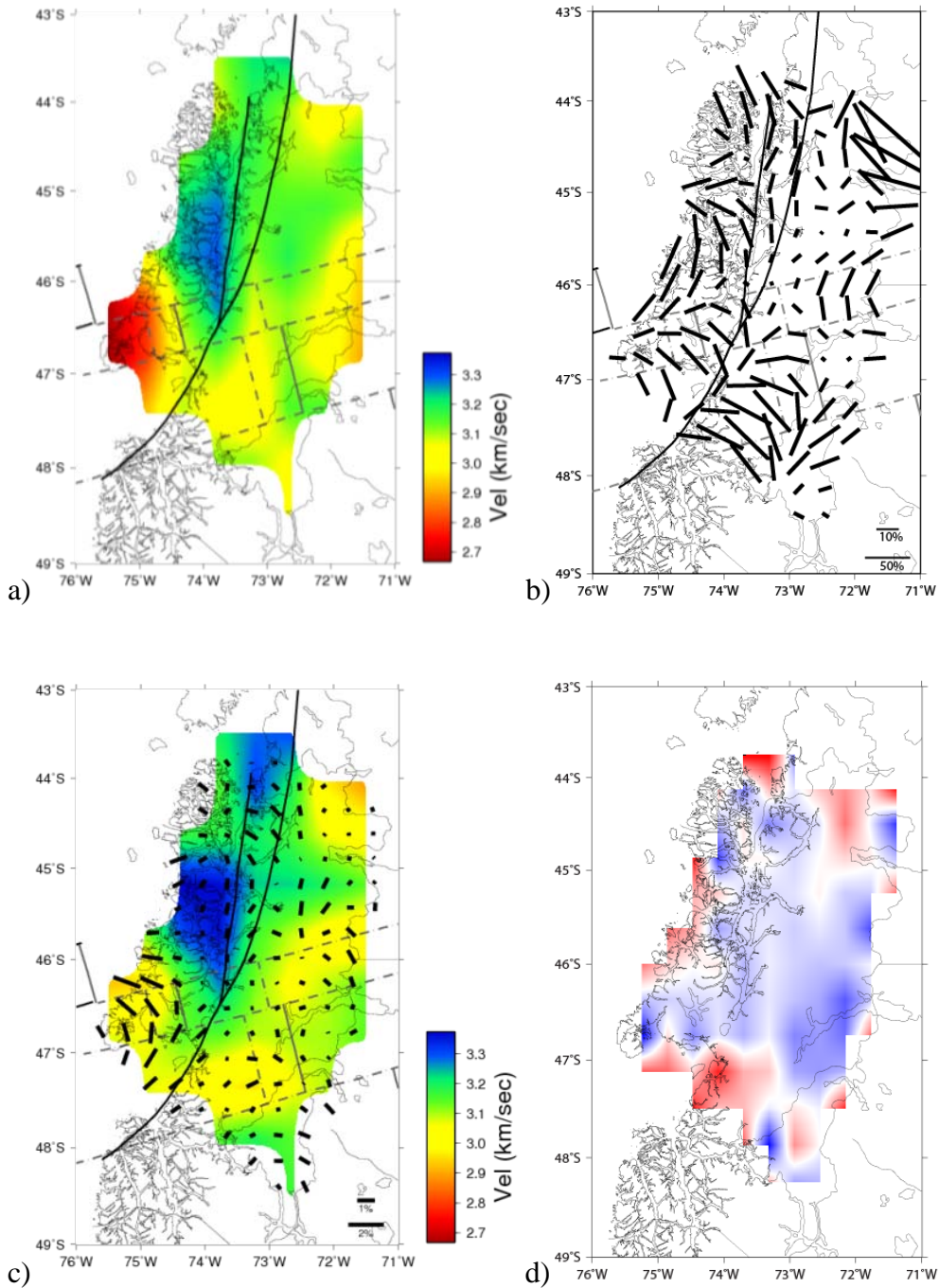


Figure 5-10. Inversion results for 11 sec period. (a) Isotropic inversion. (b) Azimuthal inversion. (c) Azimuthal and isotropic joint inversion. (d) Resolution of joint inversion. Black bars indicate magnitude and orientation of polarized fast ray.

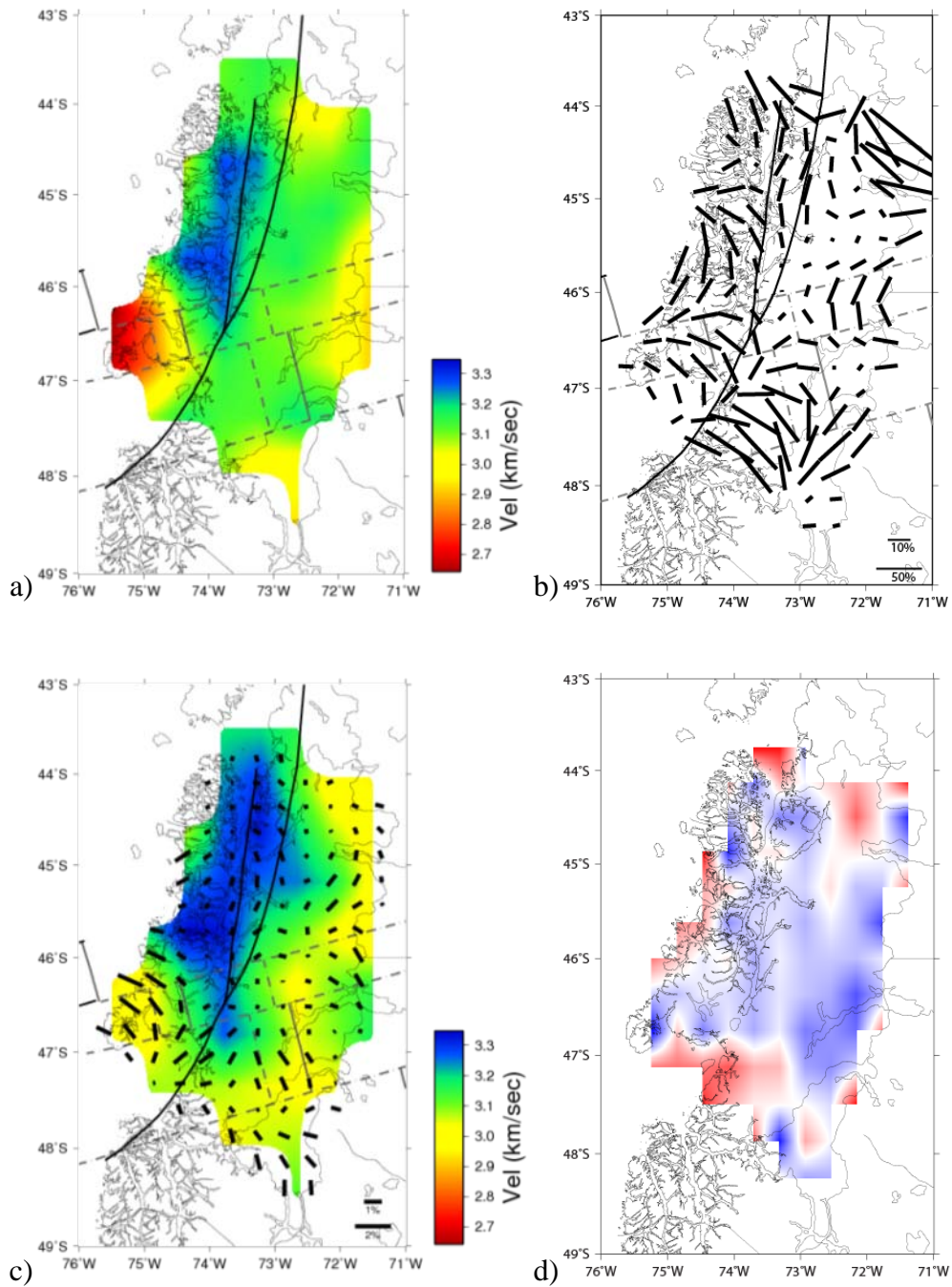


Figure 5-11. Inversion results for 12 sec period. (a) Isotropic inversion. (b) Azimuthal inversion. (c) Azimuthal and isotropic joint inversion. (d) Resolution of joint inversion. Black bars indicate magnitude and orientation of polarized fast ray.

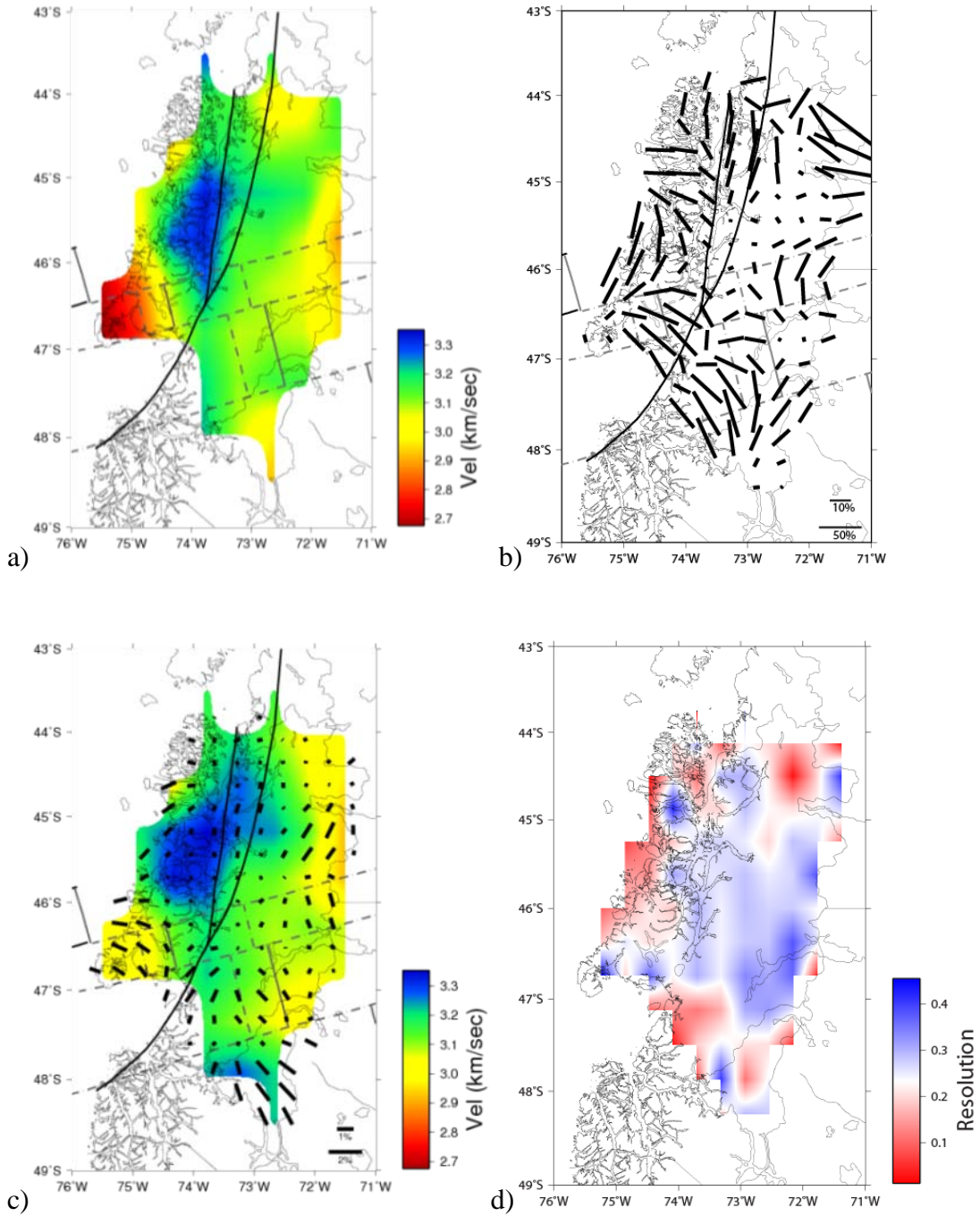


Figure 5-12. Inversion results for 13 sec period. (a) Isotropic inversion. (b) Azimuthal inversion. (c) Azimuthal and isotropic joint inversion. (d) Resolution of joint inversion. Black bars indicate magnitude and orientation of polarized fast ray.

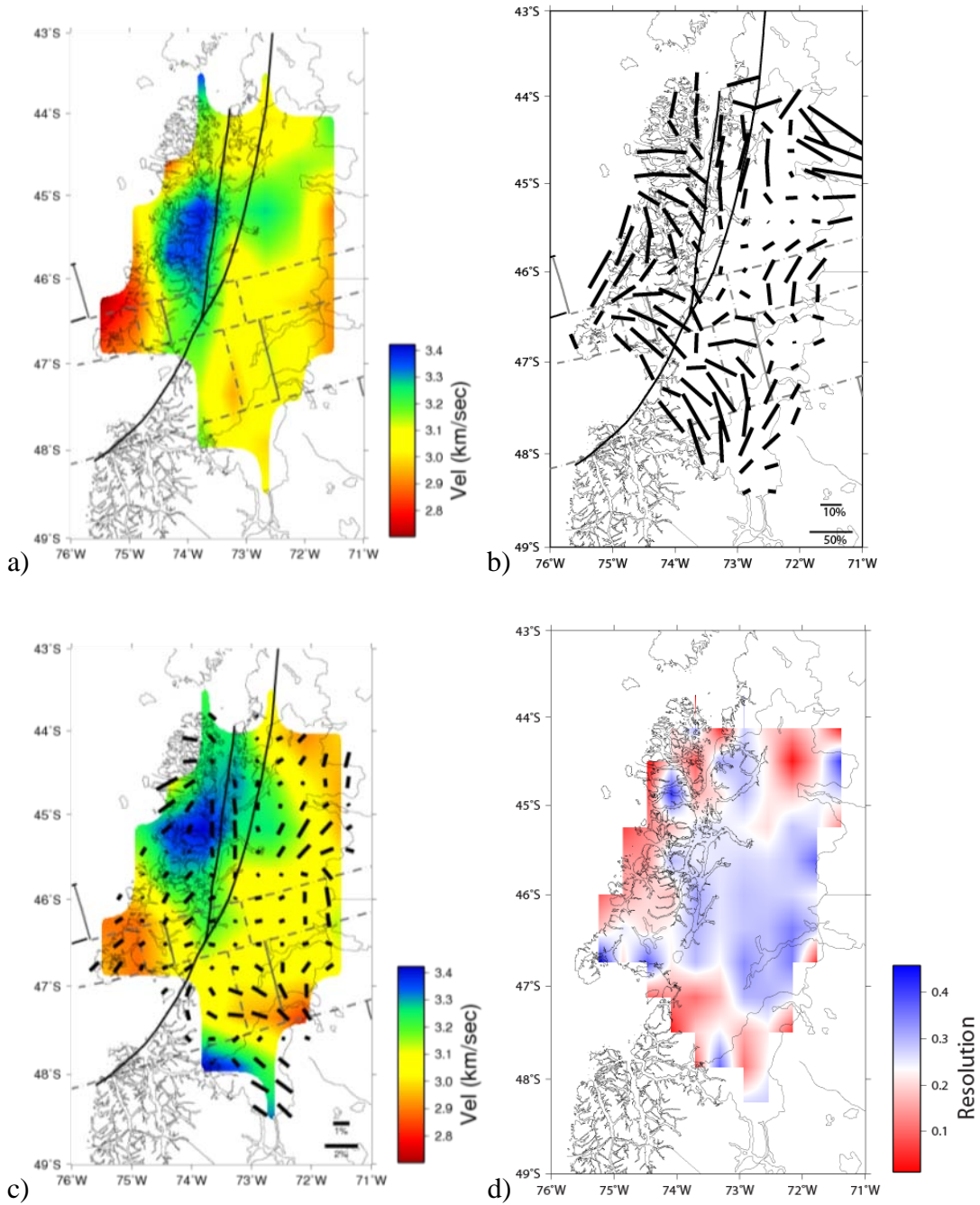


Figure 5-13. Inversion results for 14 sec period. (a) Isotropic inversion. (b) Azimuthal inversion. (c) Azimuthal and isotropic joint inversion. (d) Resolution of joint inversion. Black bars indicate magnitude and orientation of polarized fast ray

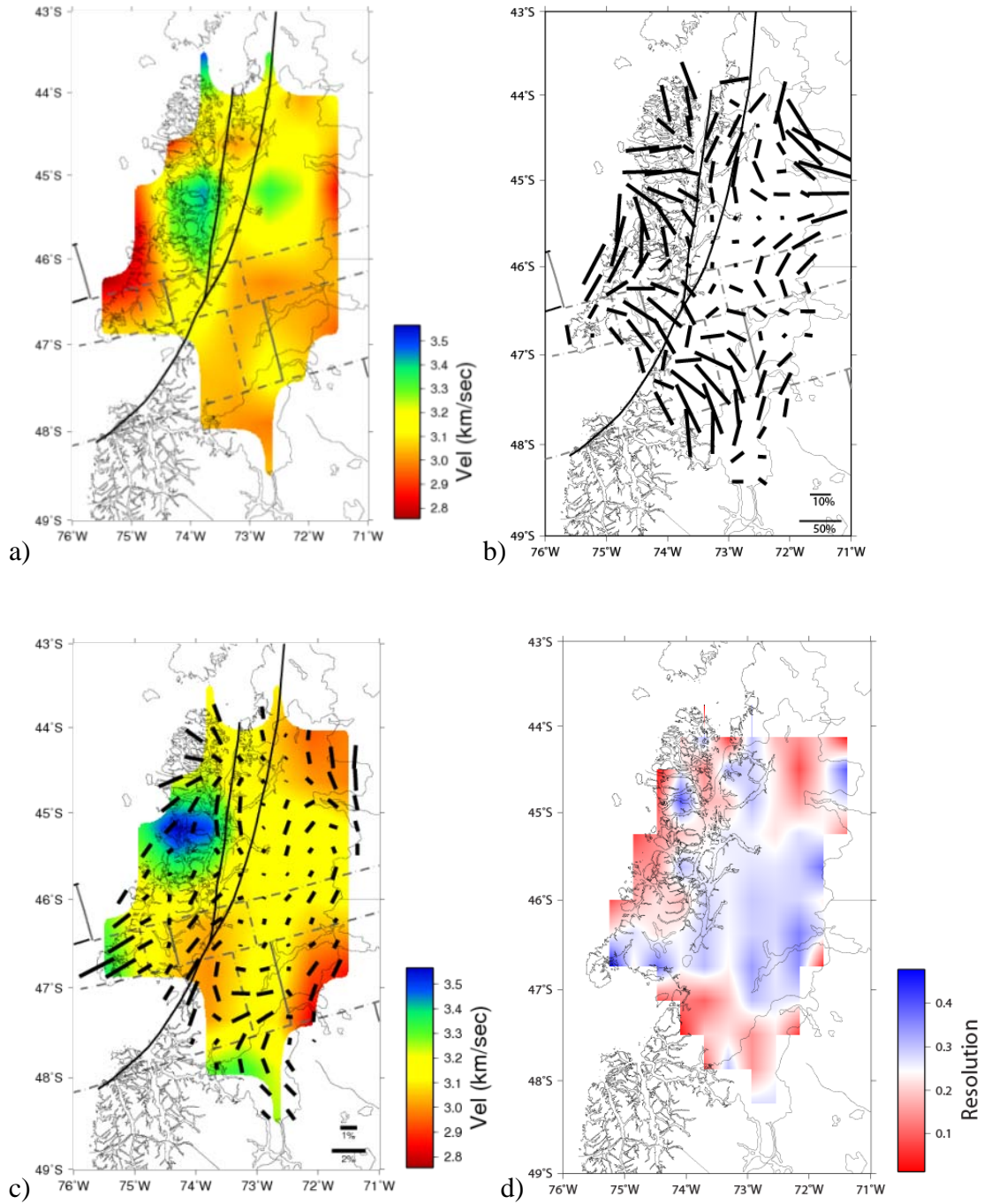


Figure 5-14. Inversion results for 15 sec period. (a) Isotropic inversion. (b) Azimuthal inversion. (c) Azimuthal and isotropic joint inversion. (d) Resolution of joint inversion. Black bars indicate magnitude and orientation of polarized fast ray.

## SUMMARY AND CONCLUSIONS

Nonvolcanic seismic tremors in the CTJ subduction zone region are similar to those observed in the Japan and Cascadia subduction zones: long duration signals lasting from hours to days, depleted in high frequencies relative to earthquakes, and occurring in conjunction with LFEs within the tremor signal.

Chilean NVT and LFE lie in a band parallel to the strike of the Nazca slab, dispersed within a narrow elongated area of 100 km width lying 100 km east of the trench. The NVT do not coincide with either recently active volcanic centers or the Liquine-Ofqui fault zone. The wide depth distribution of NVT (0-80 km), with peak occurrence at 30 km, and the depths of LFE within 40 km of the surface, indicate that both phenomena occur mostly near the plate interface and within the overriding South American plate. Two clusters of NVT activity, one very active in the south and another less active in the north, can be explained by different thermal and pore pressure conditions. The proximity of the active Chile Ridge and slab window to the southern cluster increases the temperature gradient, thereby narrowing the area of the seismogenic zone, thus allowing aseismic fault creeping. Additionally, the oceanic Nazca plate, fractured by normal and strike-slip faults formed prior to subduction, accumulated ocean water within minerals of its altered crust and then released this water later during dehydration of the subducted slab. This process increases the pore pressure and decreases the effective normal stress necessary for faulting. The frequency of occurrence of Chilean NVT is well represented by a power law, revealing a direct relationship between tremor duration and the number and size of faults involved in their production.

A clear correlation between the occurrence of NVT and soli-lunar tides was observed in the CTJ area. Tremor triggering probably occurs when fractures close to failure are activated by the small change in stresses produced by tides. The correlation between tremor occurrence and

tidal displacements is a maximum when the strain caused by semi-diurnal, diurnal, and fortnightly tidal displacements unclamps or enhances shear on existing populations of faults in the Nazca plate crust.

Interstations time-domain Green's function were estimated from cross-correlation of ambient seismic noise recorded in the Chile Triple Junction region, the resulting interstation travel times were inverted to obtain a crustal shear wave velocity model. The results show that observed crustal seismic velocities correlate well with known geologic features. High crustal velocities are where the North Patagonian Batholith outcrops or is likely present at depth, and relatively low velocities correlate with the active volcanic arc of the Southern Volcanic Zone and the Liquiñe-Ofqui intra-arc shear zone, the recent Chile Ridge subduction beneath the Taitao Peninsula, and a sedimentary sequence due to glacial sediment outflow into the NE Golfo de Penas. A pronounced high velocity anomaly in the southeastern portion of the study area correlates with high-elevation outcrops of highly compacted metamorphic rocks of the Paleozoic Eastern Metamorphic Complex.

Furthermore, cross-correlation of ambient seismic noise reveals azimuthal and radial anisotropy of the upper crust in the Chile Triple Junction area. Strong anisotropy with fast shear wave propagation directions trending parallel to the LOFZ is consistent with a wide area of shear deformation that increases at depth. Strong radial anisotropy and high seismic velocities coincide with foliated metamorphic rocks of the western belt of the Western Metamorphic Complex. Intermediate to high velocities and weaker anisotropy appear where the LCPB is present, and high phase velocities and strong anisotropy coincide with the presence of the EMC.

## REFERENCE LIST

- Aki, K. 1989. Ideal Probabilistic Earthquake Prediction. *Tectonophysics* **169**:197-198.
- Anderson, D. L. 1961. Elastic wave Propagation in Layered Anisotropic Media. *Journal of Geophysical Research* **66**:2953-&.
- Arancibia, G., J. Cembrano, and A. Leavenu. 1999. Transpresión dextral y partición de la deformación en la Zona de Falla Liquiñe-Ofqui, Aisén, Chile (44-45°S). *Revista Geologica de Chile* **26**:3-22.
- Bangs, N. L. B., S. cande, S. Lewis, and J. Miller. 1992. Structural framework of the Chile margin at the Chile Ridge collision, in Behrmann, J.H., Lewis, S.D., Musgrave, R.J., et al., eds., *Proceedings of the ODP, Initial Reports*. **141**:11-21.
- Beeler, N. M. and D. A. Lockner. 2003. Why earthquakes correlate weakly with the solid Earth tides: Effects of periodic stress on the rate and probability of earthquake occurrence. *Journal of Geophysical Research* **108**:2391.
- Behn, M. D., M. S. Boettcher, and G. Hirth. 2007. Thermal structure of oceanic transform faults. *Geology* **35**:307-310.
- Bell, C. M. and M. Suarez. 2000. The Rio Lacteo Formation of Southern Chile. Late Paleozoic orogeny in the Andes of southernmost South America. *Journal of South American Earth Sciences* **13**:133-145.
- Bensen, G. D., M. H. Ritzwoller, M. P. Barmin, A. L. Levshin, F. Lin, M. P. Moschetti, N. M. Shapiro, and Y. Yang. 2007. Processing seismic ambient noise data to obtain reliable broad-band surface wave dispersion measurements. *Geophysical Journal International* **169**:1239-1260.
- Breitsprecher, K. and D. J. Thorkelson. 2009. Neogene kinematic history of Nazca-Antarctic-Phoenix slab windows beneath Patagonia and the Antarctic Peninsula. *Tectonophysics* **464**:10-20.
- Brown, K. M., M. Tryon, H. R. DeShon, L. M. Dorman, and S. Y. Schwartz. 2005. Transient fluid pulsing and seismic tremor: Evidence of episodic creep at the updip edge of the seismogenic zone, Costa Rica. *Earth Planetary Science Letters* **238**:189-203.
- Brudzinski, M. R. and R. M. Allen. 2007. Segmentation in episodic tremor and slip all along Cascadia. *Geology* **35**:907-910.
- Campillo, M. and A. Paul. 2003. Long-range correlations in the diffuse seismic coda. *Science* **299**:547-549.
- Cande, S. C. and R. B. Leslie. 1986. Late Cenozoic tectonics of the southern Chile trench. *Journal of Geophysical Research* **91**:471-496.

- Cande, S. C., R. B. Leslie, J. C. Parra, and M. Hobart. 1987. Interaction between the Chile Ridge and Chile Trench - Geophysical and Thermal evidence. *Journal of Geophysical Research-Solid Earth and Planets* **92**:495-520.
- Castello, B., M. Olivieri, and G. Selvaggi. 2007. Local and duration magnitude determination for the Italian earthquake catalog, 1981-2002. *Bulletin of the Seismological Society of America* **97**:128-139.
- Cembrano, J. and F. Herve. 1993. The Liquine-Ofqui Fault Zone: a major Cenozoic strike-slip duplex in the Southern Andes. *Proceedings of Second International Symposium on Andean Geodynamics (ISAG)*, Oxford:175-178.
- Cembrano, J., F. Herve, and A. Lavenu. 1996. The Liquine Ofqui fault zone: A long-lived intra-arc fault system in southern Chile. *Tectonophysics* **259**:55-66.
- Christensen, N. I. and W. D. Mooney. 1995. Seismic velocity structure and composition of the continental-crust - A global view. *Journal of Geophysical Research-Solid Earth* **100**:9761-9788.
- Cochran, E. S., J. E. Vidale, and S. Tanaka. 2004. Earth Tides Can Trigger Shallow Thrust Fault Earthquakes. *Science* **306**:1164-1166.
- Crampin, S. 1984. An Introduction to wave-propagation in anisotropic media. *Geophysical journal of the Royal Astronomical Society*. **76**:17-28.
- Crampin, S. 1994. Crack models for a transversely Isotropic Medium-Comment. *Journal of Geophysical Research-Solid Earth* **99**:11749-11751.
- Dragert, H., K. Wang, and T. S. James. 2001. A Silent Slip Event on the Deeper Cascadia Subduction Interface. *Science* **292**:1525-1528.
- Dziewonski, A. M. and D. L. Anderson. 1981. Preliminary Reference Earth Model. *Physics of the Earth and Planetary Interiors* **25**:297-356.
- Eagles, G. 2004. Tectonic evolution of the Antarctic-Phoenix plate system since 15 Ma. *Earth and Planetary Science Letters* **217**:97-109.
- Ekstrom, G. and A. M. Dziewonski. 1998. The unique anisotropy of the Pacific upper mantle. *Nature* **394**:168-172.
- Escobar, T. 1980. Mapa geológico de Chile, Escala 1:1.000.000. Servicio de Geología y Minería, Santiago.

- Espinoza, F., D. Morata, E. Pelleter, R. C. Maury, M. Suarez, Y. Lagabriele, M. Polve, H. Bellon, J. Cotten, R. De la Cruz, and C. Guivel. 2005. Petrogenesis of the Eocene and Mio-Pliocene alkaline basaltic magmatism in Meseta Chile Chico, southern Patagonia, Chile: Evidence for the participation of two slab windows. *Lithos* **82**:315-343.
- Espinoza, F., D. Morata, M. Polve, Y. Lagabriele, R. C. Maury, C. Guivel, J. Cotten, H. Bellon, and M. Suarez. 2008. Bimodal back-arc alkaline magmatism after ridge subduction: Pliocene felsic rocks from Central Patagonia (47 degrees S). *Lithos* **101**:191-217.
- Faccenda, M., T. V. Gerya, and L. Burlini. 2009. Deep slab hydration induced by bending-related variations in tectonic pressure. *Nature Geoscience* **2**:790-793.
- Fang, Z., A. Boucot, V. Covacevich, and F. Herve. 1998. Discovery of Late Triassic fossils in the Chonos Metamorphic Complex, Southern Chile. *Revista Geologica de Chile* **25**:165-173.
- Forsythe, R. and E. Nelson. 1985. Geological Manifestations of Ridge Collision - Evidence from the Golfo de Penas Taitao basin, Southern Chile. *Tectonics* **4**:477-495.
- Forsythe, R. D., E. P. Nelson, M. J. Carr, M. E. Kaeding, M. Herve, C. Mpodozis, J. M. Soffia, and S. Harambour. 1986. Pliocene near-trench magmatism in southern Chile - A possible manifestation of ridge collision. *Geology* **14**:23-27.
- Gallego, A., R. M. Russo, D. Comte, V. I. Mocanu, and R. E. Murdie. 2006. Non-volcanic seismic tremor in the Chile triple junction region., AGU, Fall Meet. Suppl. *Eos Trans.*
- Gallego, A., R. M. Russo, D. Comte, V. I. Mocanu, R. E. Murdie, and J. C. Vandecar. 2007. Tidal Variation in Non Volcanic Seismic Tremor Activity at the Chile Triple Junction. AGU, Fall Meet. Suppl. *Eos Trans.*
- Gerstoft, P., K. G. Sabra, P. Roux, W. A. Kuperman, and M. C. Fehler. 2006. Green's functions extraction and surface-wave tomography from microseisms in southern California. *Geophysics* **71**:123-131.
- Godfrey, N. J., N. I. Christensen, and D. A. Okaya. 2000. Anisotropy of schists: Contribution of crustal anisotropy to active source seismic experiments and shear wave splitting observations. *Journal of Geophysical Research-Solid Earth* **105**:27991-28007.
- Gorring, M. L., S. M. Kay, P. K. Zeitler, V. A. Ramos, D. Rubiolo, M. I. Fernandez, and J. L. Panza. 1997. Neogene Patagonian plateau lavas: Continental magmas associated with ridge collision at the Chile Triple Junction. *Tectonics* **16**:1-17.

- Guivel, C., D. Morata, E. Pelleter, F. Espinoza, R. C. Maury, Y. Lagabrielle, M. Polve, H. Bellon, J. Cotten, M. Benoit, M. Suarez, and R. de la Cruz. 2006. Miocene to Late Quaternary Patagonian basalts (46-47 degrees S): Geochronometric and geochemical evidence for slab tearing due to active spreading ridge subduction. *Journal of Volcanology and Geothermal Research* **149**:346-370.
- Gutenberg, B. and C. F. Richter. 1945. Frequency of Earthquakes in California. *Nature* **156**:371-371.
- Hearn, T. M. 1996. Anisotropic Pn tomography in the western United States. *Journal of Geophysical Research-Solid Earth* **101**:8403-8414.
- Heaton, T. H. 1975. Tidal Triggering of Earthquakes. *Geophysical Journal of the Royal Astronomical Society* **43**:307-326.
- Herrmann, R. B. and J. B. Ammon. 2002. *Computer Programs in Seismology: Surface Waves, Receiver Functions and Crustal Structure.*
- Herron, E. M., S. C. Cande, and B. R. Hall. 1981. An activespreading center collides with a subduction zone - A geophysical survey of the Chile margin triple junction. *Geological Society of America Memoirs* **154**:683-701.
- Herve, F., M. Calderon, and V. Faundez. 2008. The metamorphic complexes of the Patagonian and Fuegian Andes. *Geologica Acta* **6**:43-53.
- Hess, H. H. 1964. Seismic anisotropy of uppermost mantle under oceans. *Nature* **203**:629-&.
- Husker, A., S. Peyrat, N. Shapiro, and V. Kostoglodov. 2010. Automatic non-volcanic tremor detection in the Mexican subduction zone. *Geofisica Internacional* **49**:17-25.
- Hwang, R. D., G. K. Yu, W. Y. Chang, and J. P. Chang. 2003. Lateral variations of shallow shear-velocity structure in southwestern Taiwan inferred from short-period Rayleigh waves. *Earth Planets and Space* **55**:349-354.
- Ide, S., D. R. Shelly, and G. C. Beroza. 2007. Mechanism of deep low frequency earthquakes: Further evidence that deep non-volcanic tremor is generated by shear slip on the plate interface. *Geophysical Research Letters* **34**.
- Ihmle, P. F., P. Harabaglia, and T. H. Jordan. 1993. Teleseismic detection of a slow precursor to the great 1989 Macquarie ridge earthquake. *Science* **261**:177-183.
- Ito, Y., K. Obara, K. Shiomi, S. Sekine, and H. Hirose. 2007. Slow earthquakes coincident with episodic tremors and slow slip events. *Science* **315**:503-506.

- Jentzsch, G., O. Haase, C. Kroner, and U. Winter. 2001. Mayon volcano, Philippines: some insights into stress balance. *Journal of Volcanology and Geothermal Research* **109**:205-217.
- Kanamori, H. and G. S. Stewart. 1979. A slow earthquake. *Physics of the Earth and Planetary Interiors* **18**:167-175.
- Kao, H. and S. J. Shan. 2004. The Source-Scanning Algorithm: mapping the distribution of seismic sources in time and space. *Geophysical Journal International* **157**:589-594.
- Kao, H., S. J. Shan, H. Dragert, G. Rogers, J. F. Cassidy, and K. Ramachandran. 2005. A wide depth distribution of seismic tremors along the northern Cascadia margin. *Nature* **436**:841-844.
- Katsumata, A. and N. Kamaya. 2003. Low-frequency continuous tremor around the Moho discontinuity away from volcanoes in the southwest Japan. *Geophysical Research Letters* **30**.
- La Rocca, M., K. C. Creager, D. Galluzzo, S. Malone, J. E. Vidale, J. R. Sweet, and A. G. Wech. 2009. Cascadia Tremor Located Near Plate Interface Constrained by S Minus P Wave Times. *Science* **323**:620-623.
- Lagabrielle, Y., J. Lemoigne, R. C. Maury, J. Cotten, and J. Bourgois. 1994. Volcanic record of the subduction of an active spreading ridge, Taitao Peninsula (Southern Chile). *Geology* **22**:515-518.
- Lagabrielle, Y., M. Suarez, J. Malavieille, D. Morata, F. Espinoza, R. C. Maury, B. Scalabrino, L. Barbero, R. de la Cruz, E. Rossello, and H. Bellon. 2007. Pliocene extensional tectonics in the Eastern Central Patagonian Cordillera: geochronological constraints and new field evidence. *Terra Nova* **19**:413-424.
- Lagabrielle, Y., M. Suarez, E. A. Rossello, G. Herail, J. Martinod, M. Regnier, and R. de la Cruz. 2004. Neogene to Quaternary tectonic evolution of the Patagonian Andes at the latitude of the Chile Triple Junction. *Tectonophysics* **385**:211-241.
- Lagabrielle, Y., C. Guivel, R. Maury, J. Bourgois, S. Fourcade, and H. M. 2000. Magmatic-tectonic effects of high thermal regime at the side of active ridge subduction: the Chile Triple Junction model. *Tectonophysics* **326**:255-268.
- Larose, E., A. Derode, M. Campillo, and M. Fink. 2004. Imaging from one-bit correlations of wideband diffuse wave fields. *Journal of Applied Physics* **95**.
- Lay, T. and H. Kanamori. 1981. An asperity model of large earthquake sequences, in *Earthquake Prediction*, edited by D. W. Simpson and P. G. Richards. American Geophysical Union, Washington D. C.:680.

- Lee, W. H., R. E. Bennett, and K. L. Meagher. 1972. A method of estimating magnitude of local earthquakes from signal duration. Page 67. U.S. Geol. Survey Open-File Rept.
- Levshin, A., L. Ratnikova, and J. Berger. 1992. Peculiarities of surface-wave propagation across central Eurasia. *Bulletin of the Seismological Society of America* **82**:2464-2493.
- Li, A. B. and R. S. Detrick. 2003. Azimuthal anisotropy and phase velocity beneath Iceland: implication for plume-ridge interaction. *Earth and Planetary Science Letters* **214**:153-165.
- Lin, F. C., M. H. Ritzwoller, J. Townend, S. Bannister, and M. K. Savage. 2007. Ambient noise Rayleigh wave tomography of new Zealand. *Geophysical Journal International* **170**:649-666.
- Lobkis, O. I. and R. L. Weaver. 2001. On the emergence of the Green's function in the correlations of a diffuse field. *Journal of the Acoustical Society of America* **110**:3011-3017.
- Love, A. E. H. 1944. A treatise on the mathematical theory of elasticity. Dover, reprint.
- Lowry, A. R., K. M. Larson, V. Kostoglodov, and R. Bilham. 2001. Transient fault slip in Guerrero, southern Mexico. *Geophysical Research Letters* **28**:3753-3756.
- Maggi, A., E. Debayle, K. Priestley, and G. Barruol. 2006. Azimuthal anisotropy of the Pacific region. *Earth and Planetary Science Letters*. **250**:53-71.
- Mainprice, D. and P. G. Silver. 1993. Interpretation of SKS-waves using samples from the subcontinental lithosphere. *Physics of the Earth and Planetary Interiors* **78**:257-280.
- McGuire, J. J., P. F. Ihmlé, and T. H. Jordan. 1996. Time-domain observations of a slow precursor to the 1994 Romanche Transform earthquake. *Science* **274**:82-85.
- Milbert, D. 2007. Solid. Page modified from IERS Conventions (2003). Dennis D. McCarthy and Gerard Petit. (IERSTechnical Note No.2032).
- Miyazawa, M. and E. E. Brodsky. 2008. Deep low-frequency tremor that correlates with passing surface waves. *Journal of Geophysical Research-Solid Earth* **113**.
- Montagner, J. P. and H. C. Nataf. 1986. A simple method for inverting the azimuthal anisotropy of surface-waves. *Journal of Geophysical Research-Solid Earth and Planets* **91**:511-520.
- Murdie, R., D. J. Prior, P. Styles, and S. S. Flint. 1993. Seismic responses to ridge-transform subduction: Chile triple junction. *geology* **21**:1095-1098.

- Murdie, R. and R. Russo. 1999. Seismic anisotropy in the region of the Chile margin triple junction. *Journal of South American Earth Sciences* **12**:261-270.
- Murdie, R., P. Styles, D. Prior, and A. Daniel. 2000. A new gravity map of southern Chile and its preliminary interpretation. *Revista Geologica de Chile* **27**.
- Nadeau, R. M. and D. Dolenc. 2005. Nonvolcanic Tremors Deep Beneath the San Andreas Fault. *Science* **307**:389-389.
- Nakajima, J. and A. Hasegawa. 2006. Anomalous low-velocity zone and linear alignment of seismicity along it in the subducted Pacific slab beneath Kanto, Japan: Reactivation of subducted fracture zone? *Geophysical Research Letters* **33**.
- Nakata, R., N. Suda, and H. Tsuruoka. 2008. Non-volcanic tremor resulting from the combined effect of Earth tides and slow slip events. *Nature Geoscience* **1**:676-678.
- Naranjo, J., H. Moreno, and N. Banks. 1993. La erupcion del Volcan Hudson en 1991 (46S), Region XI, Aisen, Chile. *Chile Boletin* **44**:1-50.
- Nelson, E., R. Forsythe, J. Diemer, M. Allen, and O. Urbina. 1993. Taitao Ophiolite - A ridge collision ophiolite in the fore-arc of Southern Chile (46-degrees-S). *Revista Geologica De Chile* **20**:137-&.
- Obara, H. 2002. Nonvolcanic deep tremor associated with subduction in southwest Japan. *Science* **296**:1679-1681.
- Obara, K. and H. Hirose. 2006. Non-volcanic deep low-frequency tremors accompanying slow slips in the southwest Japan subduction zone. *Tectonophysics* **417**:33-51.
- Obara, K., H. Hirose, F. Yamamizu, and K. Kasahara. 2004. Episodic slow slip events accompanied by non-volcanic tremors in southwest Japan subduction zone. *Geophysical Research Letters* **31**:L23602.
- Oleskevich, D. A., R. D. Hyndman, and K. Wang. 1999. The updip and downdip limits to great subduction earthquakes: Thermal and structural models of Cascadia, south Alaska, SW Japan, and Chile. *Journal of Geophysical Research-Solid Earth* **104**:14965-14991.
- Pankhurst, R. J., S. D. Weaver, F. Herve, and P. Larrondo. 1999. Mesozoic-Cenozoic evolution of the North Patagonian Batholith in Aysen, southern Chile. *Journal of the Geological Society* **156**:673-694.
- Payero, J. S., V. Kostoglodov, N. Shapiro, T. Mikumo, A. Iglesias, X. Perez-Campos, and R. W. Clayton. 2008. Nonvolcanic tremor observed in the Mexican subduction zone. *Geophysical Research Letters* **35**.

- Peacock, S. M. 1990. Fluid in subduction zones. *Science* **248**:329-337.
- Peacock, S. M. 2009. Thermal and metamorphic environment of subduction zone episodic tremor and slip. *Journal of Geophysical Research-Solid Earth* **114**.
- Peacock, S. M. and K. Wang. 1999. Seismic consequences of warm versus cool subduction metamorphism: Examples from southwest and northeast Japan. *Science* **286**:937-939.
- Peng, Z. G. and K. V. Chao. 2008. Non-volcanic tremor beneath the Central Range in Taiwan triggered by the 2001 M-w 7.8 Kunlun earthquake. *Geophysical Journal International* **175**:825-829.
- Peterson, C. L. and D. H. Christensen. 2009. Possible relationship between nonvolcanic tremor and the 1998-2001 slow slip event, south central Alaska. *Journal of Geophysical Research-Solid Earth* **114**:13.
- Ramos, V. A. 2005. Seismic ridge subduction and topography: Foreland deformation in the Patagonian Andes. *Tectonophysics* **399**:73-86.
- Ramos, V. A. and S. M. Kay. 1992. Southern Patagonian plateau basalts and deformation: back-arc testimony of ridge collision. *Tectonophysics* **205**:261-282.
- Ranero, C. R. and V. Sallares. 2004. Geophysical evidence for hydration of the crust and mantle of the Nazca plate during bending at the north Chile trench. *Geology* **32**:549-552.
- Ranero, C. R., R. von Huene, W. Weinrebe, and C. Reichert. 2006. Tectonic processes along the Chile convergent margin.
- Robertson, S., D. Wiens, K. Koper, and A. Vera. 2003. Crustal and upper mantle structure of southernmost South America inferred from regional waveform inversion. *Journal of Geophysical Research* **108**:doi:10.1029/2002JB001828.
- Rogers, G. and H. Dragert. 2003. Episodic Tremor and Slip on the Cascadia subduction zone : The Chatter of Silent Slip. *Science* **20**:1492-1493.
- Rosenau, M., D. Melnick, and H. Echtler. 2006. Kinematic constraints on intra-arc shear and strain partitioning in the southern Andes between 38 degrees S and 42 degrees S latitude. *Tectonics* **25**.
- Rubinstein, J. L., J. Gomberg, J. E. Vidale, A. G. Wech, H. Kao, K. C. Creager, and G. Rogers. 2009. Seismic wave triggering of nonvolcanic tremor, episodic tremor and slip, and earthquakes on Vancouver Island. *Journal of Geophysical Research-Solid Earth* **114**.
- Rubinstein, J. L., M. La Rocca, J. E. Vidale, K. C. Creager, and A. G. Wech. 2008. Tidal Modulation of Nonvolcanic Tremor. *Science* **319**:186-189.

- Russo, R. M., A. Gallego, D. Comte, V. I. Mocanu, R. E. Murdie, and J. C. VanDecar. 2010a. Source-side shear wave splitting and upper mantle flow in the Chile Ridge subduction region. *Geology* **38**:707-710.
- Russo, R. M., V. I. Mocanu, A. Gallego, R. M. Russo, D. Comte, R. E. Murdie, J. C. Vandecar, and S. Van der Lee. 2007. Shear Wave Splitting and Seismic Anisotropy in the Chile Ridge Subduction Region. AGU, Fall Meet. Suppl. *Eos Trans*, T34B-06.
- Russo, R. M., J. C. VanDecar, D. Comte, V. I. Mocanu, A. Gallego, and R. E. Murdie. 2010b. Subduction of the Chile Ridge: upper mantle structure and flow. *GSA Today*.
- Shapiro, N. and M. Campillo. 2004. Emergence of broadband Rayleigh waves from correlations of the ambient seismic noise. **31**.
- Shapiro, N., M. Campillo, L. Stehly, and M. Ritzwoller. 2005. High-Resolution Surface-Wave Tomography from Ambient Seismic Noise. *Science* **307**:1615-1618.
- Shelly, D. R., G. C. Beroza, and S. Ide. 2007. Non-volcanic tremor and low-frequency earthquake swarms. *Nature* **446**:305-307.
- Shelly, D. R., G. C. Beroza, S. Ide, and S. Nakamura. 2006. Low-frequency earthquakes in Shikoku, Japan, and their relationship to episodic tremor and slip. *Nature* **442**:188-191.
- Shelly, D. R., W. L. Ellsworth, T. Ryberg, C. Haberland, G. S. Fuis, J. Murphy, R. M. Nadeau, and R. Burgmann. 2009. Precise location of San Andreas Fault tremors near Cholame, California using seismometer clusters: Slip on the deep extension of the fault? *Geophysical Research Letters* **36**.
- Shibuya, T., T. Komiya, R. Anma, T. Ota, S. Omori, Y. Kon, S. Yamamoto, and S. Maruyama. 2007. Progressive metamorphism of the Taitao ophiolite; evidence for axial and off-axis hydrothermal alterations. *Lithos* **98**:233-260.
- Silver, P. G. 1996. Seismic anisotropy beneath the continents: Probing the depths of geology. *Annual Review of Earth and Planetary Sciences* **24**:385-&.
- Smith, M. L. and F. A. Dahlen. 1973. Azimuthal dependence of Love and Rayleigh-wave propagation in a slightly anisotropic. *Journal of Geophysical Research* **78**:3321-3333.
- Snieder, R. 2004. Extracting the Green's function from the correlation of coda waves: a derivation based on stationary phase. *Phys Rev E Stat Nonlin Soft Matter Phys* **69**:046610.
- Su, W., C. Y. Wang, and Z. X. Huang. 2008. Azimuthal anisotropy of Rayleigh waves beneath the Tibetan Plateau and adjacent areas. *Science in China series D-earth science* **51**:1717-1725.

- Suda, N., R. Nakata, and T. Kusumi. 2009. An automatic monitoring system for nonvolcanic tremors in southwest Japan. *Journal of Geophysical Research-Solid Earth* **114**.
- Tarantola, A. 2005. *Inverse Theory Problem and Methods for Model Parameter Estimation*.
- Thomas, A. M., R. M. Nadeau, and R. Burgmann. 2009. Tremor-tide correlations and near-lithostatic pore pressure on the deep San Andreas fault. *Nature* **462**:1048-U1105.
- Thomson, S. N. and F. Herve. 2002. New time constraints for the age of metamorphism at the ancestral Pacific Gondwana margin of southern Chile (42-52 degrees S). *Revista Geologica De Chile* **29**:255-271.
- Tolstoy, M., F. L. Vernon, J. A. Orcutt, and F. K. Wyatt. 2002. Breathing of the seafloor: Tidal correlations of seismicity at Axial volcano. *Geology* **30**:503-506.
- Wahr, J. 1995. Earth Tides, *Global Earth Physics, A handbook of Physical Constants*. Pages 40-46. AGU reference Shelf.
- Wang, K., Y. Hu, M. Bevis, E. Kendrick, R. Smalley, R. B. Vargas, and E. Lauria. 2008. Crustal motion in the zone of the 1960 Chile earthquake: Detangling earthquake-cycle deformation and forearc-sliver translation (vol 9, art no Q04017, 2008). *Geochemistry Geophysics Geosystems* **9**.
- Watanabe, T., Y. Hiramatsu, and K. Obara. 2007. Scaling relationship between the duration and the amplitude of non-volcanic deep low-frequency tremors. *Geophysical Research Letters* **34**:L07305.
- Wech, A. G. and K. C. Creager. 2008. Automated detection and location of Cascadia tremor. *Geophysical Research Letters* **35**.
- Willner, A. P., F. Herve, and H. J. Massonne. 2000. Mineral chemistry and pressure-temperature evolution of two contrasting high-pressure-low-temperature belts in the Chonos Archipelago, Southern Chile. *Journal of Petrology* **41**:309-330.
- Xu, G. C. and P. Knudsen. 2000. Earth tide effects on kinematic/static GPS positioning in Denmark and Greenland. *Physics and Chemistry of the Earth Part a-Solid Earth and Geodesy* **25**:409-414.
- Yao, H. J. and R. D. van der Hilst. 2009. Analysis of ambient noise energy distribution and phase velocity bias in ambient noise tomography, with application to SE Tibet. *Geophysical Journal International*. **179**:1113-1132.

## BIOGRAPHICAL SKETCH

Alejandro Gallego was born in La Coruna Spain in 1975, son of Antonio and Carmen. The middle of 6 siblings, he grew up in Santiago de Chile. He graduated from San Ignacio High School in 1993. He entered the Engineering School at the University of Chile in 1995. With two years of incursion in electrical engineering, he decided change to the geology department after an extraordinary geology field trip. He received his Bachelor in Geology in 2004. He made his thesis in conjunction with the department of Geophysics on Seismic Tomography of Southern Peru, where he became very interested in seismology and he decided to take the opportunity to began his Phd program in seismology at the University of Florida in 2004. In 2008 he got married to April and in 2010 they welcomed a son, Sebastian.